MODELING THE DIRECT AND INDIRECT EFFECTS OF ATMOSPHERIC AEROSOLS ON TROPICAL CYCLONES

A Dissertation

by

KEUN HEE LEE

Submitted to the Office of Graduate Studies of
Texas A&M University
in partial fulfillment of the requirements for the degree of

DOCTOR OF PHILOSOPHY

December 2011

Major Subject: Atmospheric Sciences

Modeling the Direct and Indirect Effects of Atmospheric Aerosols on Tropical Cyclones

MODELING THE DIRECT AND INDIRECT EFFECTS OF ATMOSPHERIC AEROSOLS ON TROPICAL CYCLONES

A Dissertation

by

KEUN HEE LEE

Submitted to the Office of Graduate Studies of
Texas A&M University
in partial fulfillment of the requirements for the degree of

DOCTOR OF PHILOSOPHY

Approved by:

Chair of Committee,	Renyi Zhang
Committee Members,	Sarah D. Brooks
	Courtney Schumacher
	Shari Yvon-Lewis
Head of Department,	Kenneth Bowman

December 2011

Major Subject: Atmospheric Sciences

ABSTRACT

Modeling the Direct and Indirect Effects of Atmospheric Aerosols on Tropical Cyclones.

(December 2011)

Keun Hee Lee, B.S., Ewha Womans University;

M.S., Seoul National University

Chair of Advisory Committee: Dr. Renyi Zhang

The direct and indirect effects of aerosols on the hurricane 'Katrina' have been investigated using the WRF model with a two-moment bulk microphysical scheme and modified Goddard shortwave radiation scheme. Simulations of the hurricane 'Katrina' were conducted under the three aerosol scenarios: 1) the clean case with an aerosol number concentration of 200 cm-1, 2) the polluted case with a number concentration of 1000 cm-1, and 3) the aerosol radiative effects (AR) case with same aerosol concentration as polluted case but with a modified shortwave radiation scheme.

The polluted and AR cases have much larger amounts of cloud water and water vapor in troposphere, and the increased cloud water can freeze to produce ice water paths. A tropical cyclone in dirty and dusty air has active rainbands outside the eyewall due to aerosol indirect effects. The aerosol direct effect can lead to the suppressing of convection and weakening of updraft intensity by warming the troposphere and cooling the surface temperature. However, these thermal changes in atmosphere are concerned with the enhanced amounts of cloud hydrometeors and modification of downdraft and

corresponding the low level winds in rainband regions. Thus, the AR case can produce the enhanced precipitation even in the weakest hurricane. When comparing the model performance between aerosol indirect and direct effect by ensemble experiments, the adjustment time of the circulation due to modification of the aerosol radiative forcing by aerosol layers may take a longer time than the hurricane lifetime, and the results from the simulated hurricane show that it is more sensitive to aerosol indirect effects which are related to the cloud microphysics process changes.

From this aerosol study, we can suggest that aerosols can influence the cloudiness, precipitation, and intensity of hurricanes significantly, and there may be different results in the meso-scale convective clouds cases. The hurricane system is a large and complex convective system with enormous heating energy and moistures. Moreover, relationships between various hydrometeors in hurricane systems are difficult to isolate and thus, it needs further study with more realistic cloud microphysical processes, aerosol distributions, and parameterizations.

ACKNOWLEDGEMENTS

I would like to thank my committee chair, Dr. Renyi Zhang, and my committee members, Dr. Sarah D. Brooks, Dr. Courtney Schumacher, and Dr. Shari Yvon-Lewis, for their guidance and support throughout the course of this research.

Thanks also go to my friends and colleagues and the department of Atmospheric Sciences faculty and staff for making my time at Texas A&M University a great experience.

Finally, thanks to my mother and father for their encouragement and to my husband, Hyun Myoung and my son Nathan, for their loves, and to my LORD for his great love and faithfulness.

TABLE OF CONTENTS

LIST OF FIGURES

FIGURE Page

FIGURE Page

FIGURE Page

LIST OF TABLES

1. INTRODUCTION

The importance of aerosol effects on cloud has received substantial attention from recent climate researches due to the aerosol influence on the Earth's radiation budget and climate. The aerosol direct effects refer to the scattering or absorbing of solar and thermal radiation. Also, aerosol absorption and backscattering change the atmospheric temperature profile, decrease the solar radiation at the surface, and lowers surface moisture fluxes. As the result, the aerosol radiative effect suppresses the convective activity and reduces a hydrological cycle [*Ackerman et al*., 2000; *Ramanathan et al*., 2001]. This effect also has been recognized as the semi-direct effect [*Hansen et al*., 1997; *Johnson et al*., 2004]. Moreover aerosols can influence a cloud indirectly acting as cloud condensation nuclei (CCN) or ice nuclei (IN) and alter the microphysical and optical properties of a cloud. The changes of aerosol number concentration can also affect the cloud droplet effective radius leading to the modification of cloud albedo, lifetime, water, and onset of precipitation, which is known as the aerosol indirect effect. The Fourth Assessment Report (AR4) of the Intergovernmental Panel on Climate Change (IPCC) [*IPCC*, 2007] estimated that the direct effect due to anthropogenic aerosols and cloud albedo effect (the first indirect effect of the Twomey effect) on the global mean radiative forcing are - 0.5 Wm^{-2} and - 0.7 Wm^{-2} respectively. This radiative forcing of climate change by anthropogenic

---

This dissertation follows the style of *Journal of Geophysical Research.*

aerosols is short-lived and negative with a high climate efficacy but still low scientific understanding with the estimate error of +/- 1.2 Wm^{-2}. Current understanding of the aerosol indirect effect still remains highly uncertain because of the complexity of cloud processes governed by intricate thermodynamic, dynamic, and microphysic processes and their interactions. Moreover, the assessment of the radiative forcing by the aerosol properties such as the number/size distribution and the chemical composition is difficult to quantify due to a complex mixture of chemical components of anthropogenic particles [*Hegg et al*., 1997; *Putaud et al*., 2000; *Ramanathan et al*., 2001].

Recently, atmospheric aerosols have been hot topics for the tropical cyclones study. *Willoughby et al*. [1985] showed the results of the microphysical structure of the hurricane clouds and found that seeding was not likely to affect cloud dynamics because of too much natural ice and too little supercooled water where seeding was applied using the STORMFURY conceptual model. Moreover, the results of seeding are often hard to separate from naturally occurring intensity changes. These problems are considered as two main flaws in the STORMFURY project [*Willoughby et al*., 1985]. Later on, *Rosenfeld and Woodley* [2003] and *Andreae et al*. [2004] claimed that by loading of large amount of small aerosols, warm rain process can be prevented from tropical clouds and more cloud water can be ascended to the freezing level to produce sufficient supercooled water and made up for the STORMFURY problem [*Willoughby et al*., 1985]. *Mann and Emanuel* [2006] made a model simulation for the warming effects by accumulating greenhouse gases in the atmosphere along with the reduced aerosols trends recently and showed the linkage of the long-term trends in tropical Atlantic warmth to

the trend of increasingly stronger hurricanes in recent decades. *Lau and Kim* [2007] claims that during the 2006 hurricane season, the cooling over the tropical North Atlantic by increasing aerosols in this area suppressed tropical hurricane activities in the western Atlantic and the Caribbean using satellite data. Recent studies have suggested that the relationship between dust aerosols and the formation and intensity of Atlantic tropical cyclones [*Dunion and Velden*, 2004; *Wu*, 2007; *Zhang et al. 2007*]. During the spring and summer months, a deep, well-mixed layer of hot, dry, and dusty air forms over the Sahara Desert due to intense heating. As this air layer often moves westward over the Atlantic basin, it is undercut by cool and moist marine air. This elevated layer of dry continental air is referred to as the Saharan Air Layer (SAL) and well-known to its negative influence tropical cyclogenesis [*Dunion and Velden*, 2004]. *Dunion and Velden* [2004] found mechanisms of the Saharan Air Layer (SAL) to weaken or prevent to intensify the hurricane activities. *Wu* [2007] also showed the possible linkage between the SAL and the summer African monsoon and Atlantic hurricane activity. *Zhang et al*. [2007] indicated that dust in SAL influenced the tropical cyclone development by leading hydrometeors changes, the storm diabatic heating distribution and thermodynamic structure using the Regional Atmospheric Modeling System (RAMS).

Several numerical studies have been made to simulate the role of aerosols on tropical cyclones and hurricane. *Khain et al*. [2005] and *Lynn et al*. [2005] simulated a deep convective cloud and showed a large number of small droplets by an increase in the concentration of small aerosols results in a delay of the raindrop formation and rainout at the lower part of the clouds. However, this partial suppression of the raindrop formation

can lead additional latent heat release at high levels due to cloud water freezing and water vapor/ice condensation. Consequently, it is founded that in a polluted atmosphere, convective cloud can develop invigoratively [*Khain et al*., 2005; *Lynn et al., 2005*; *Van den Heever et al*., 2006; *Rosenfeld et al*., 2007]. In the study of possible aerosol effects on lightning activity of hurricanes, *Khain et al*. [2008] showed the dramatic increases of supercooled water, ice contents, and vertical velocities by adding aerosols at the maritime cloud base. These numerical results also indicated that the invigorate convection at the periphery of the hurricane system could decrease the influx of air mass into the hurricane center and lead to the relative weakening of convection and intensity in the tropical cyclone center. *Rosenfeld et al*. [2007] have been studied the possible impacts of submicron CCN seeding to suppress the warm rain in the hurricanes system and showed the weakening of the tropical cyclone by the low level evaporative cooling of the unprecipitated cloud drops and the added cooling due to melting of precipitation using the WRF model. On the other hand, *Zhang et al*. [2007] linked the changes in storm track over the North Pacific to Asian pollution and showed the effects on radiative forcing by atmospheric aerosols might intensify storms and trigger more precipitation over the Pacific Ocean during winter season using long-term satellite cloud data and WRF model simulations.

For the study of aerosol direct effects, observations and numerical studies using GCM and regional models are also used. *Menon et al*. [2002] and *Huang et al*. [2007] studied the possible aerosol contributions to the climate change over the eastern Asia and India using a GCM and a regional coupled climate-chemistry-aerosol model,

respectively. They also showed some changes in the regional atmospheric stability, vertical motions by absorbing aerosols, and, consequently, decreasing trend of hydrological cycle over this area in terms of long-term scale. *Jiang and Feingold* [2006] explained several reasons for these similar responses of the dynamics and the precipitation pattern with a new-coupled large eddy model. When aerosol radiative effects are included, modifications in the atmospheric heating profiles can be occurred because of the decrease in downwelling solar radiation by absorbing aerosols. Therefore the absorbing aerosols may lead the reduction in surface latent, sensible heat fluxes, and significant effects on cloud parameters. *Takemura et al*. [2005] showed some changes in the cloud water and precipitation by a variation of the hydrological cycle with a temperature change by the aerosol direct effects and suggested a reduction of the increase in the surface air temperature by greenhouse gases with global aerosol transport-radiation model. *Bäumer et al*. [2007] parameterized the optical properties of Black Carbon (BC) and Organic Carbon (OC) for the shortwave and longwave portions of the atmospheric radiation spectra and used in the AGCM. In this study, he suggested that aerosols including BC and OC could lead to a decrease in the net solar flux. *Fan et al*. [2008] investigated the aerosol radiative effects on the deep convective clouds using a spectral-bin cloud resolving model and showed decreases of convective intensity and precipitation because of the increase of aerosols absorptions.

In this study, the direct and indirect effects of aerosols on the hurricane system are investigated. Although many previous studies have shown the direct and indirect aerosol contributions to the development of the mesoscale convective system, both

experimental and numerical investigations of the aerosol effects on the tropical cyclone systems are quite limited. Recently, several studies investigated the cloud microphysical processes of tropical cyclones adding more Cloud Condensation Nuclei (CCN)s with their conceptual models. However, the study of the aerosol direct effects on the hurricane system has not been performed. We estimate the aerosol indirect effects using the two-moment bulk microphysical scheme to parameterize microphysical processes in the WRF model. In this scheme, the number concentrations of cloud droplets are included as a new prognostic variable. The associated aerosol direct and semi-direct radiative forcing values for hurricane system are also evaluated by using an aerosol radiative module. This module calculates the wavelength-dependent aerosol radiative properties such as aerosol optical depth (AOD), single scattering albedo (SSA), and asymmetry factor (AF) based on the aerosol characteristics and ambient relative humidity. These aerosol radiative properties are important factors to determine the aerosol radiative effects on clouds and associated forcing [*Fan et al*., 2008]. For the model simulation, this module is incorporated into the Goddard shortwave radiation scheme [*Chou and Suarez*, 1999] of the WRF model to interact with a cloud.

2. METHODOLOGY

2.1 WRF MODEL

The WRF model is a next-generation meso-scale numerical weather prediction (NWP) system designed to serve both operational forecasting and atmospheric research needs and suitable for a broad spectrum of feedback processes over a wide range of spatial scales since it is a fully compressible and nonhydrostatic model that applies nested domain. Its vertical coordinate is a terrain-following hydrostatic pressure coordinate and 35 vertical levels are used. The Arakawa C-grid staggering and the Runge-Kutta 2nd and 3rd order time integration schemes are used and for the advection schemes, the model uses the 2nd to 6th order schemes in both horizontal and vertical directions. For the calculation of the acoustic and gravity-wave modes, a time-split small step is used. In this study, several physics schemes are considered. The Monin-Obukhov and thermal diffusion schemes were used for the surface-layer and land-surface physics. Both domains also used the YSU scheme for the planetary boundary layer [*Noh et al*., 2001]. For the atmospheric longwave and shortwave radiation physics scheme, the RRTM [*Mlawer et al*., 1997] and Goddard radiation schemes [*Chou and Suarez*, 1999] are implemented, respectively. More detailed description of the WRF model is provided in the WRF web site http://www.wrf-model.org/index.php [*Li et al*., 2008].

Most of microphysical schemes in the present WRF model use single-moment bulk schemes that only consider the mass concentrations of hydrometeors and prevent

the evaluation of the aerosol-cloud interaction for the aerosol indirect effect. Moreover, the Goddard shortwave radiation scheme used for the interaction with cloud in the default WRF model has zero value of aerosol optical properties at 11 wavelengths. Therefore, the WRF model cannot account for the scattering and absorption of the aerosol to consider the aerosol direct and semi-direct effect. Because of these limited applications of the microphysical and radiative schemes for the aerosol-cloud interaction, a two-moment microphysics scheme [*Li et al.*, 2008] and a modified Goddard shortwave radiation scheme [*Fan et al*., 2008] incorporated with an aerosol radiative module has been developed and implemented into the WRF model.

2.2 TWO-MOMENT BULK MICROPHYSICAL SCHEME WITH AEROSOL EFFECTS

A two-moment bulk microphysical scheme used in this study has been modified and implemented into the WRF model by *Li et al*. [2008] to account for the aerosols effects on a cloud with calculation of the time-dependent bulk mass mixing ratios and the number concentration of five types of hydrometeors including cloud water, rain water, ice crystals, snow flakes, and graupels, as well as the aerosol mass mixing ratio, surface area and number concentration.

The size distributions of the five types of hydrometeors are represented by the gamma function and thirty-two microphysical processes for the five types of hydrometeors are considered in the two-moment microphysical scheme. . In the present

work most of the microphysical processes in the two-moment bulk microphysics scheme by *Lou* [2003] are similar to those described in details by *Wang and Chang* [1993]. For the warm rain process, the analytic solutions to the stochastic collection equation (SCE) by a polynomial approximation for the collection kernel [*Long*, 1974] are used according to *Cohard and Pinty* [2000]. The auto-conversion parameterization developed by *Liu and Daum* [2004] is also applied in this simulation. For the ice nucleation, the deposition nucleation, immersion-freezing, and contact-freezing processes are considered. The number of ice crystals by deposition nucleation is the function of temperature and ice supersaturation [*Pruppacher and Klett,* 1997; *Wang and Chang*, 1993].

$$N_i = N_{i0}\exp\left[-a\left(T - T_0\right)\right]\left(\frac{Q_v - Q_{si}}{Q_{si}}\right)^b\left(\frac{1}{\rho}\right), \tag{1}$$

where N_i is the number of ice crystals, $N_{i0} = 10^{-2}/\mathrm{m}^3$, T is temperature, Q_v is saturation of water vapor, Q_{si} is the supersaturation of water vapor with respect to ice, $a = 0.6\ \mathrm{K}^{-1}$, $b = 5.0$, and ρ is air density. The number production rate of newly nucleated ice crystals at a time step and a certain grid point, R_{nuc} is calculated from the relationship with a temperature fields.

$$R_{nuc} = \frac{dN_i}{dt} = -aN_i\frac{dT}{dt} \tag{2}$$

The rate of drop freezing is from the immersion-freezing parameterization based on the stochastic hypothesis formulated by *Bigg* [1953] and homogeneous freezing by *DeMott et al*. [1994]. Contact-freezing of drops follows *Meyers et al*. [1997] and is negligible for temperatures warmer than -10℃. The secondary ice production of *Hallet and Mossop* [1974] is considered for the rime-splintering mechanism. At T = -5℃, 250 collisions of droplets having radius exceeding 24 μm with graupel particles lead to the formation of one ice splinter [*Li et al*., 2008]. We consider the several processes for ice particles growth such as deposition growth, aggregation among ice crystals, and riming of supercooled droplets in the cold phase of the cloud development [*Wang and Chang*, 1993; *Lou et al*., 2003]. A heavily rimed ice crystal is transferred to a graupel and melting occurs by instantaneous conversion into liquid drops of equal mass if all ice particles fall below the freezing level.

In this simulation, we do not include the aerosol sources and sinks except for the activation process in clouds. The number concentrations of both aerosol types decayed exponentially with altitudes and they have a log-normal size distribution:

$$n(lnD) = \frac{N}{\sqrt{2\pi}\ln\sigma_g}\exp\left[\frac{-1}{2}\left(\frac{lnD - lnD_g}{\ln\sigma_g}\right)^2\right], \tag{3}$$

where D is the aerosol diameter, N is the number concentration of aerosols, D_g is the geometric mean diameter, and σ_g is the geometric standard deviation [*Seinfeld and Pandis*, 2005].

For the CCN nucleation, the aerosol spectrum is divided into 92 sections from 0.002 μm to 2.5 μm. A critical aerosol/CCN radius is calculated according to the Köhler theory using the calculated water supersaturation from the WRF model. Once aerosols and CCNs with radius exceeding the critical value is activated, but the radius of aerosols, $r_a < 0.03$ μm, the mass of nucleated droplets is calculated under the equilibrium assumption. In the case of $r_a > 0.03$ μm, the mass of nucleated droplets on these CCN at zero supersaturation is calculated as $m_w = K4/3r_a^3\rho_w$, where $3 < K < 8$ [*Khain et al*., 2000].

2.3 AEROSOL RADIATIVE MODULE FOR AEROSOL OPTICAL PROPERTIES CALCULATION IN GODDARD SHORTWAVE RADIATION SCHEME

The aerosol radiative module calculates the wavelength (λ)-dependent aerosol radiative properties such as AOD (τ), SSA (σ), and AF (g) based on the aerosol composition, size distribution, mixing state, and ambient relative humidity [*Fan et al*., 2008]. Aerosol optical depth, AOD (τ) is defined integrating the spectral extinction coefficient over an incremental distance and quantifies scattering and absorbing by aerosols that occurs between the top of the atmosphere and a given altitude for radiative transfer calculations. This value increases from zero at the top of the atmosphere to a maximum at the ground. The ratio of Q_s to Q_e is called the single-scattering albedo, SSA (σ), where Q_s and Q_e are the dimensionless scattering efficiency and extinction efficiency of a particle. If there is no absorption, σ equals 1 and in the case of very high

absorption, σ goes to zero. Asymmetry factor, AF (g) is a parameter derived from the phase function that gives the relative direction of scattering by particles or gases. AF approaches +1 for the forward (Mie) direction scattering and -1 for the backward direction scattering. If g = 0, scattering of particles is isotropical or Rayleigh scattering (the same in all directions) [*Seinfeld and Pandis*, 2005]. To obtain the aerosol optical properties, the Mie calculations have to be carried out to calculate the extinction efficiency (Q_e), scattering efficiency (Q_s), and asymmetry factor (g). The aerosol size distribution and the complex refractive index of aerosol components for these Mie calculations are needed. In this study, aerosols are assumed to have internal Black Carbon (BC)-cores surrounded by ammonium sulfate and to be in states of external and core-coated internal mixed aerosol. For the internally mixed aerosol states, the complex refractive index of aerosol components is computed based on the volume-weighted average of the individual refractive index [*Hänel*, 1976]. For the aerosol size parameter, $x = 2\pi r/\lambda$, the hygroscopic growth of a water-soluble component at a certain ambient humidity is calculated by this relationship [*Mallet et al*., 2004],

$$r_{g,a(0)} = r_{g,a(b)}(1-h)^{e}, \tag{4}$$

where *r* and *h* are the wet particle radius and the relative humidity, respectively. The coefficient *e* which depends on the aerosol type, is 0.25 for the internal mixture of ammonium sulfate and BC [*Chazette and Liousse*, 2001; *Hänel*, 1976]. To avoid repeated Mie calculations at the later time steps, the well-proven numerical code for the

Mie calculations by *Bohren and Huffman* [1983] is used. First we get a look-up table for all the relevant optical properties over all size ranges and a set of typical refractive indexes of atmospheric aerosols by performing full Mie calculations. We provide the calculated complex refractive index and size parameter in terms of look-up tables and obtain Q_e, σ, and g by interpolating linearly from this table. These aerosol optical properties also cover the whole spectrum region from 0.175 to 10μm to match the same spectrum region in the solar fluxes calculation by the Goddard shortwave radiation scheme.

The aerosol optical depth, τ (λ , j) at a certain wavelength (λ) and atmospheric layer (j) is calculated by integration for all aerosol log-normal size spectrum with 92 sections.

$$\tau(\lambda, j) = \sum_{i=1}^{92} Q_e(\lambda, r_i)\pi r_{i^2} n(r_i, j) dz_j, \tag{5}$$

where $n(r_i , j)$ and dz_j indicate the aerosol number concentrations and the height of atmospheric layer. The r_i in this formula is the wet particle radius which is calculated from equation (2). The weighted-mean SSA (σ) and AF (g) for the mixed aerosol at a certain wavelength and layer are computed by below equations.

$$\sigma(\lambda, j) = \sum_{i=1}^{92} \tau(\lambda, r_i, j)\sigma(\lambda, r_i, j) / \sum_{i=1}^{92} \tau(\lambda, r_i, j) \tag{6}$$

$$g(\lambda, j) = \sum_{i=1}^{92} \tau(\lambda, r_i, j)\sigma(\lambda, r_i, j)g(\lambda, r_i, j) / \sum_{i=1}^{92} \tau(\lambda, r_i, j)\sigma(\lambda, r_i, j) \quad (7)$$

For the externally mixed aerosol components, the aerosol radiative properties are computed for each component, and summed for the total aerosol population to get the ensemble aerosol radiative properties [*Wolf*, 2002]. More detailed explanation for the aerosol radiative scheme are suggested by *Fan et al*. [2008].

For the model simulation, this aerosol module is incorporated into the Goddard shortwave radiation scheme to online calculate the aerosol optical properties as a function of wavelength (λ). This shortwave radiation scheme by *Chou and Suarez* [1999] can compute the solar fluxes due to absorption and scattering by clouds, aerosols and gases including water vapor. Fluxes integration can cover the whole spectrum region from 0.175 to 10 μm such as seven bands for ultraviolet region (0.175 ~ 0.4 μm), one band for photosynthetically active radiation region (0.4 ~ 0.7 μm), and three bands in the near infrared region (0.7 ~ 10.0 μm). Once the aerosol radiative parameters are determined, they affect the solar fluxes in the shortwave radiation scheme and then interact with the other model components such as dynamical and microphysical processes. Although the longwave portions of the radiation spectra by aerosol optical properties is also required, the effects of aerosols on shortwave radiation is known to be more important than the longwave radiation. Therefore we only consider the aerosol optical properties for the shortwave radiation scheme and effect of aerosols on the longwave radiation is not treated in this study.

2.4 DESIGN OF NUMERICAL EXPERIMENTS

To evaluate the aerosol impacts on the hurricane, we performed simulations of the hurricane Katrina from 27 August 0 z to 30 August 0 z by using a two-way nested grid of the WRF model. A 9 km outer domain with a nest on a 3 km mesh is integrated. Each domain has 217 x 227 and 460 x 448 points in the north-south and east-west directions respectively with a center at 29.5 N, 90 W on 35 vertical levels with top at 10 hPa, which is used to provide about 2000 km x 2000 km and 1380 km x 1340 km area coverage for outer and inner domain, respectively. This domain area can cover the Gulf of Mexico and southern part of US influenced by the hurricane Katrina including highly industrial region such as Houston area (Figure 2.1). Both domains use a two-moment

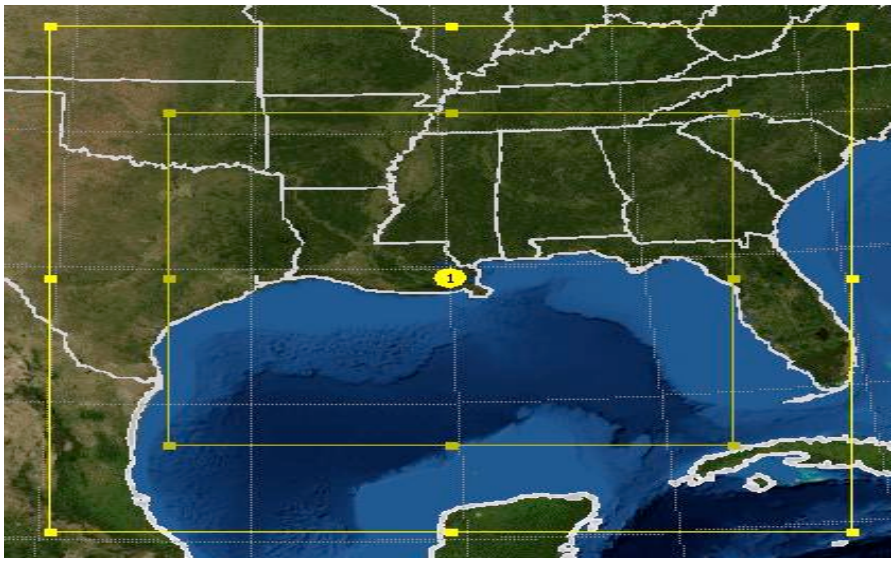

Figure 2.1. Nested grid domains. The inner domain, 1 is defined as the study domain.

microphysical scheme to consider aerosol effects on a cloud and they also employed the Goddard shortwave radiation scheme coupled with aerosol radiative module to calculate the aerosol radiative properties. Both domains were initialized from 6 hourly NCEP FNL Final analysis data (1^{o}x1^{o}) and used NCEP global SST data for 00:00 UT 27 August.
microphysical scheme to consider aerosol effects on a cloud and they also employed the Goddard shortwave radiation scheme coupled with aerosol radiative module to calculate the aerosol radiative properties. Both domains were initialized from 6 hourly NCEP FNL Final analysis data (1^{o}x1^{o}) and used NCEP global SST data for 00:00 UT 27 August.

Aerosol composition is an important factor of cloud physics mechanisms by affecting the activation processes. In the southeast of Texas, oxidation of volatile organic compounds (VOCs) from industrial and transportation sources contributes significantly to formation and growth of aerosols [*Zhang et al*., 2004; *Fan et al*., 2006; *Yuan et al*., 2008]. Especially, the organics are the major aerosol components in Houston area as shown in the observational and modeling studies of *Russell et al*. [2004] and *Fan et al*. [2005]. Figure 2.2 is the average value of aerosol optical thickness in mid-visible range from the MODIS-AQUA data during 27^{th} ~30^{th} Aug. in 2005 over the Gulf of Mexico. Even the ocean, the amount of aerosol in this area was moderate due to the transported continental aerosol from the industrial regions over the land, such as the Southern part of Texas, Louisiana, and Florida. Therefore, the aerosol information in this area is very useful to evaluate the influence of aerosols on tropical cyclones.

In this study, the maritime and polluted continental aerosols will be assumed to contain sea salt (NaCl) and ammonium sulfate ($(NH_4)_2SO_4$) aerosols for the aerosol

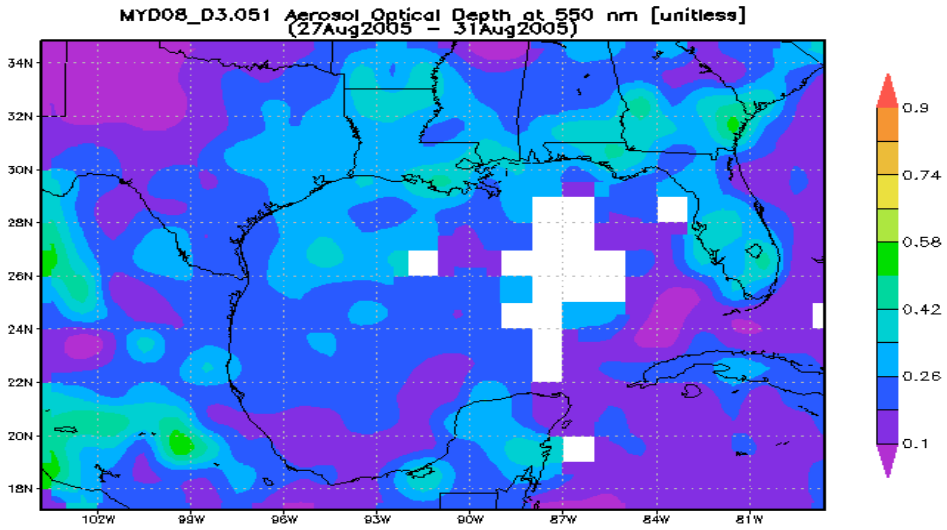

Figure 2.2. Aerosol optical depth in mid-visible range during 27th Aug. ~ 31th Aug. in 2005 over the Gulf of Mexico from the MODIS-AQUA.

compositions [*Fan et al*., 2006]. For the aerosol effect on hurricane, simulations assumed the ammonium sulfate ($(NH_4)_2SO_4$) aerosols as polluted continental aerosols but different number concentrations with cloud microphysical scheme and radiation scheme conducted to evaluate aerosol effects on hurricane system. Then, a series of sensitivity simulations have been performed. The clean case assumed to contain $(NH_4)_2SO_4$ with a number concentration of 200 cm^{-3} at the surface level over a whole domain and is performed as a control run and the polluted case with an elevated concentration of over 1000 cm^{-3} as the initial and boundary aerosol distributions considering aerosol indirect effects [*Li et al*., 2008]. Aerosol concentration of both cases is vertically interpolated with a log-normal distribution and they also use the two-

moment bulk microphysics scheme for cloud microphysics processes (Figure 2.3). In the case of aerosol radiative effects (referred to as the AR), aerosols are assumed to have internal BC-cores surrounded by ammonium sulfate to calculate aerosol radiative properties with the modified Goddard shortwave radiation scheme to account for the aerosol direct effects. The aerosol number concentration and vertical distribution are same as the polluted case and the mass mixing ratios are assumed to be about 5 % for BC and 95 % for ammonium sulfate. BC produced from incomplete fossil fuel and biomass burning is a very important absorptance, which reduces substantially the

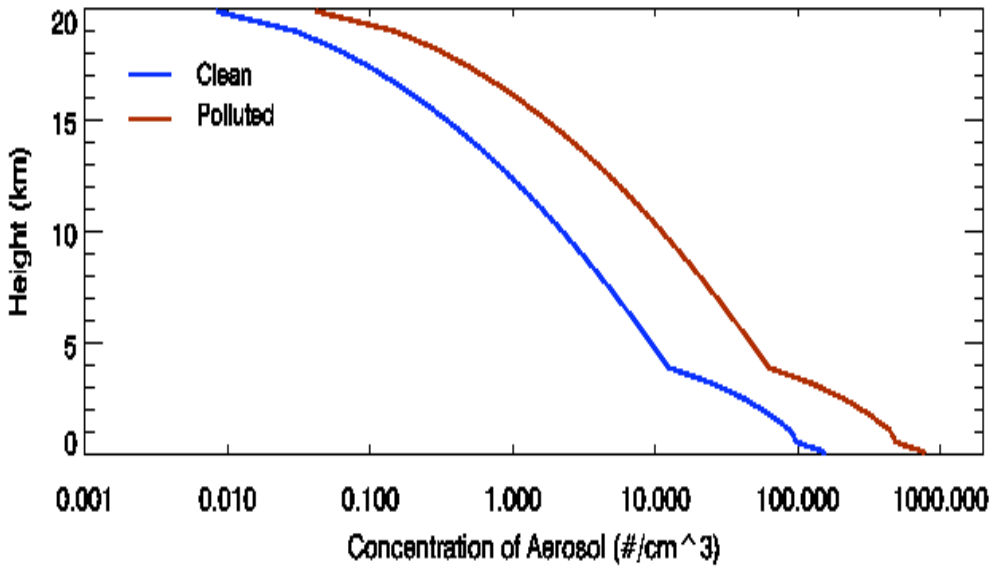

Figure 2.3. Domain-averaged vertical aerosol profiles for the clean and polluted scenarios.

incoming solar radiation reaching the surface while ammonium sulfate only has a scattering effect. Therefore the SSA value for pure ammonium sulfate aerosols is 1.0 at the wavelength of 0.55 μm. The impact of BC on clouds and radiative forcing depends on its mixing state. Therefore it is common to treat BC as a core coated by the other aerosol components for the aerosol radiative properties study [*Ackerman and Toon*, 1981] and coating on BC aerosols may increase the absorption of solar radiation significantly. Therefore, the SSA of internally mixed BC-ammonium sulfate aerosol in this study is 0.89 at the mid-visible range and this value is in the 0.85 to 0.95 ranges of the SSAs for the most Northern Hemisphere aerosols [*Ramanathan et al*., 2001]. This simulation also uses the two-moment bulk microphysical scheme for cloud-aerosol interactions same as the clean and polluted cases. The simple descriptions of three idealized cases are shown in Table 1.

Even the hurricane generates over the ocean off the industrialized areas, the polluted case can be supposed because of outflows of anthropogenic aerosols from polluted regions, for instance Houston. Both scenarios are also assumed to have same background maritime aerosols, NaCl with a number concentration of 100 cm^{-3} at the surface and it is vertically interpolated with a log-normal distribution same as in ammonium sulfate aerosols. In reality, sea salt is one of the giant CCN in Houston regions because sea salt particles can be transported inland in the summer season along the coast of the Gulf [*Verma et al*., 2006]. Also they can influence on the warm rain formation of the hurricane system because wind driven sea salt particles serve as giant

CCN (>1 μm diameter) that initiate early rain even when large concentrations of small CCN exist [*Woodcock,* 1953; *Segal et al*., 2004].

Table 1. The description of three idealized scenarios.

Model Scenarios	**Clean**	**Polluted**	**AR**
Initial/Boundary aerosol # concentrations (Ammonium Sulfate / Sea salt)	$200cm^{-3}$ /$100cm^{-3}$	$1000cm^{-3}$ /$100cm^{-3}$	$1000cm^{-3}$ /$100cm^{-3}$
Two-Moment Bulk microphysics scheme (*Li et al.,* 2008)	√	√	√
Goddard shortwave radiation scheme with aerosol radiative properties (*Fan et al*., 2008)			√

3. THE NUMERICAL RESULTS OF AEROSOL SENSITIVITY TESTS

3.1 THE EVOLUTION OF STORM SYSTEM

For the overall evolution of the simulated tropical cyclone (TC) intensity, Figure 3.1 shows the time evolution of the minimum surface pressure (a) and maximum surface wind speeds (b) for the clean, polluted, and radiation (AR) cases from 00:00 UTC 27th to 00:00 UTC 30th August. The results are also compared with the six hourly observational data from the National Hurricane Center (NHC) during the same time period. According to the observational data, the minimum surface pressure of the real hurricane Katrina (black dashed line) fell to 902 hPa and reached its maximum wind speed of 75 ms^{-1} around 18:00 UTC 28th August and made a landfall near Louisiana on 29th August 2005. Even three simulated hurricanes cannot capture the exact values of the observational wind speeds and minimum surface pressure, they can describe the main features of the hurricane evolution: an initial stage from 0 to about 24 h; a rapid intensification stage from 24 h to about 60 h; and a weakening stage from 60 h to 72 h. Within the first 24 h, the hurricane Katrina in the clean case (blue solid line) intensifies much earlier than the other two cases and passes ahead the observed minimum surface pressure and maximum surface wind speeds. It reaches the minimum surface pressure of 885 hPa and the maximum surface wind speed of 79.5 ms^{-1} around 00:00 UTC 29th with the formation of the stronger hurricane than the real hurricane Katrina. The polluted case (dark red dotted line) with high aerosol number concentration and mass mixing ratio is

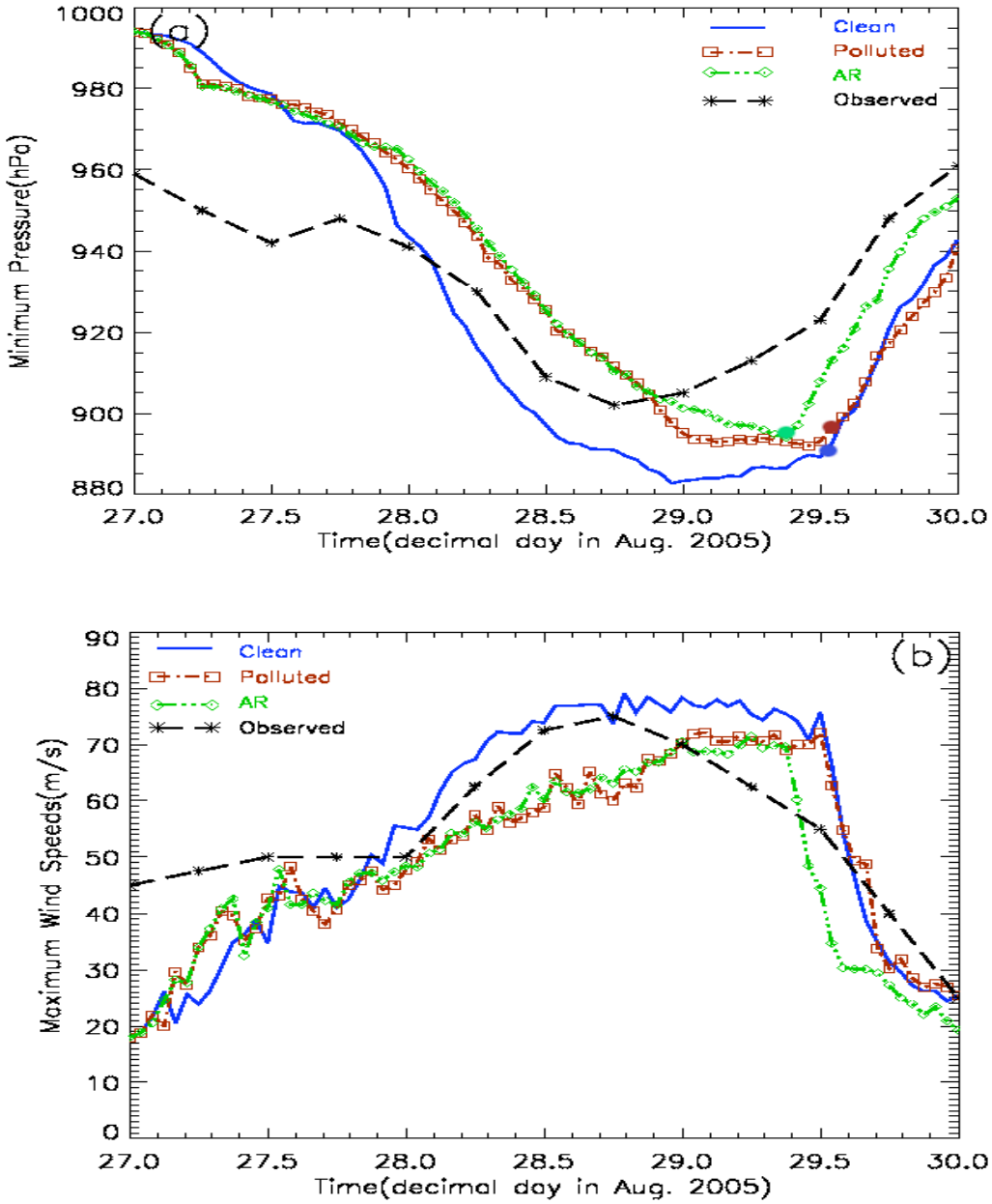

Figure 3.1. Time evolution of (a) minimum surface pressure and (b) maximum wind speed at the lowest model level in three simulations: the clean in blue, polluted in dark red, and AR in green. The black line is the observed values of the hurricane Katrina. Three spots of the surface pressure indicate the landfalls of the simulated hurricanes.

designed to evaluate the aerosol indirect effect on hurricane system and suggests a delayed intensification and weak intensity with higher minimum surface pressure and less maximum surface wind speeds than those in the clean case. Figure 3.2 shows the vertical wind shear of three simulated hurricane systems. For this study, the vertical wind shear is defined as the magnitude of the difference between the average 200 hPa wind and the 850 hPa wind within an annulus starting at 100 km and extending to 300 km from the center of the hurricane [*Knaff et al*., 2004]. It has been recognized that the vertical wind shear tends to give a negative influence on tropical cyclone development [*Emmanuel and Nolan*, 2004; *Camargo et al*., 2007] and has a deleterious effect on the intensity of developed tropical cyclones [*DeMaria*, 1996; *Frank and Ritchie*, 2001].

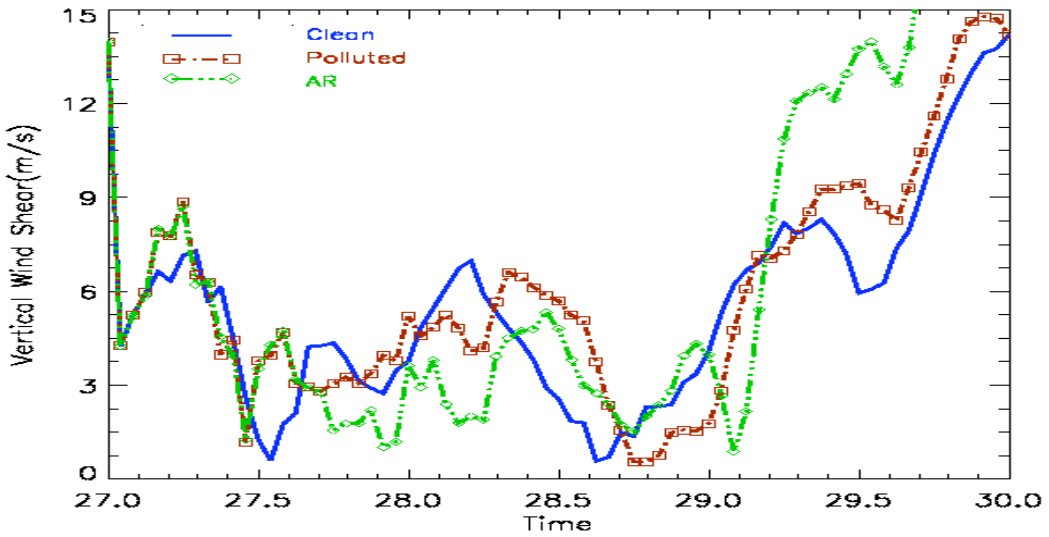

Figure 3.2. Same as in Figure 3.1 except for the magnitude of vertical wind shear.

During the hurricane development, the magnitudes of vertical wind shear decreased and start to increase after the weakening of the hurricane intensity. The abrupt increase of vertical wind shear over 5 ms^{-1} is noticeable in the AR case on 29th August. When it is compared with the hurricane intensity in Figure 3.1, the wind shear affects its weakness on 29th. Therefore, the hurricane of the AR case shows more active interaction with the environmental wind shear and its early dissipation and landfall than the other cases. These results indicate that the simulated tropical cyclone evaluation and intensity are quite sensitive to the modification of other hydrometeors due to the change in the representation of aerosol size distributions, i.e. the aerosol indirect effect. The AR case (green dotted line) has the same aerosol number concentration and mixing ration of those in the polluted case but suggests the modified shortwave radiation scheme for the calculation of aerosol radiative properties to see the aerosol direct effect. The AR case shows the weakest hurricane intensity and early dissipation but a similar intensity to that in the polluted case. It means that aerosol direct effect also can influence the weakening of intensity and early landing of hurricane but the simulated hurricane is less sensitive to the aerosol direct effects than the aerosol indirect effects.

3.2 OVERALL CLOUD MICROPHYSICAL AND THERMODYNAMIC FIELDS

The change of aerosol distribution is directly reflected in the modification of cloud microphysical fields. Figure 3.3 show the time series of cloud microphysical fields averaged over the inner domain during a whole simulation time period. Initial cloud

(a) Simulated cloud number concentration

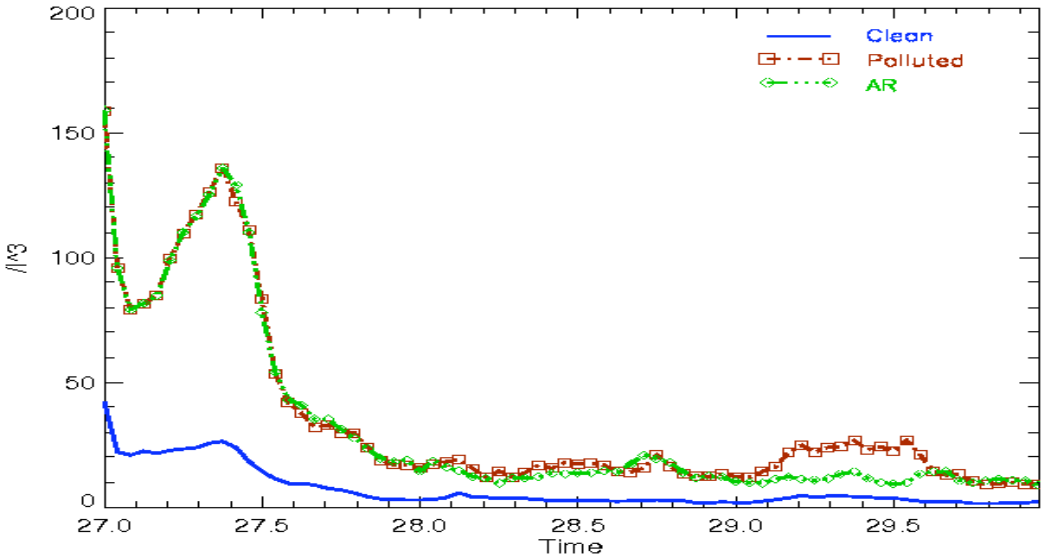

(b) Simulated ice number concentration

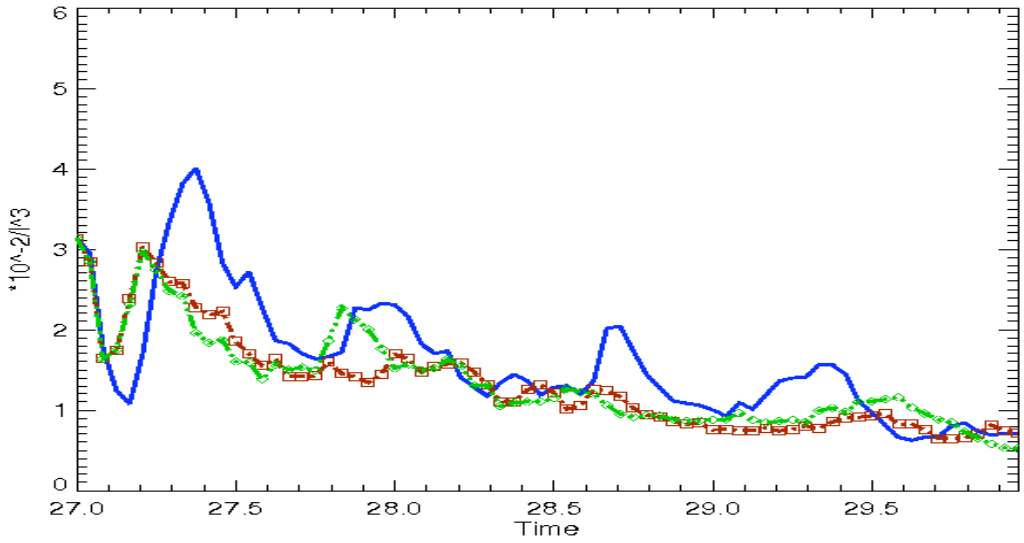

Figure 3.3. Same as in Figure 3.1 but for (a) cloud number concentration, (b) ice number concentration, (c) liquid water path, and (d) ice water path.

(c) Simulated liquid water path

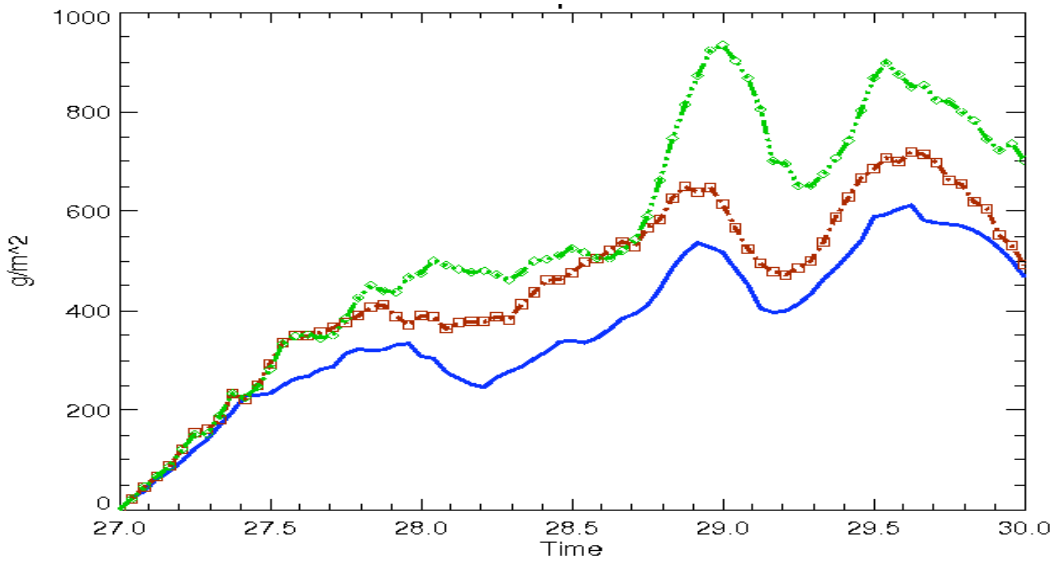

(d) Simulated ice water path

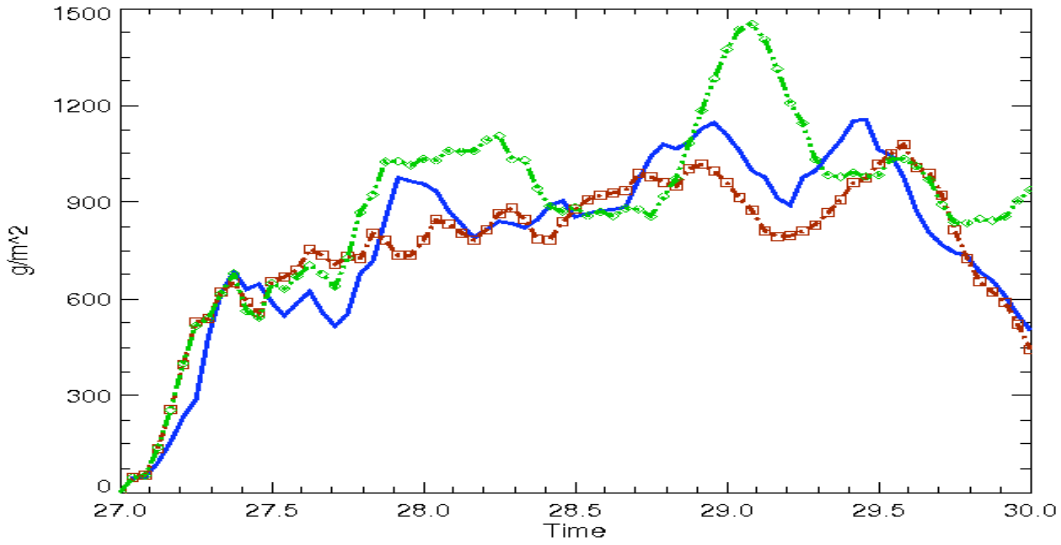

Figure 3.3. continued.

droplets number concentration (CDNC) (Figure 3.3a) is decreased gradually due to the consumption by precipitation process. Two polluted air cases show higher CDNC than clean case because high aerosol concentrations correspond to a large amount of nucleated cloud droplet. The CDNC of the AR case does not differ appreciably from that of the polluted case, since the aerosol composition and size distribution are identical in both cases. However, the clean case with a low aerosol concentration has higher ice number concentration than those of two polluted air cases (Figure 3.3b) and it may be related with the reduction of vertical updraft velocity in the polluted and AR cases due to the aerosol indirect effect.

The liquid water path (LWP) and ice water path (IWP) for the simulated hurricane system are presented in Figure 3.3c and Figure 3.3d, respectively. The LWP is defined as the sum of the mass-integrated mixing ratios of cloud water and rainwater that determine the water clouds, while IWP is defined as the sum of the mass-integrated mixing ratios of ice, snow, and graupel that determine the ice clouds [*Fan et al*., 2008]. Higher values of the polluted and AR cases in LWP mean more active warm rain process than that in the clean case and the increase of liquid water contents in cloud is due to a high aerosol concentration. Moreover, liquid and ice water paths in the AR case become to increase after sunset and suggest the highest LWP and a peak value of IWP during the night time (28:00 UTC and 29:00 UTC), while the polluted and clean cases show similar trends of liquid and ice water contents. During the daytime, the heating in troposphere and cooling at surface occur due to shortwave radiation absorbing by aerosols, while there are no more heating in troposphere and a quick cooling at surface after sunset. The

dramatic changes in vertical temperature profiles can lead the formation of cloud water and ice water contents. The diurnal trends in two water paths represent the aerosol shortwave radiation effects in the AR case. Also the both of LWP and IWP are closely related because ice contents are from nucleation and freezing/deposition of cloud water. Thus, the value of IWP is concerned with the mixed phase rain process. The large IWP in AR represents the activity of convective system and that there are large amounts of cloud ice, snow, and graupel formation. It suggests that updraft activity, the amount of cloud ice, and liquid water contents are influenced by high aerosol concentrations and the aerosol radiative effects.

The aerosol direct effect can reduce the incoming solar radiation fluxes at the surface and eventually, surface air temperature. Figure 3.4 presents the spatially averaged (a) surface air temperature, (b) latent heat flux, and (c) surface wind speeds over the inner domain during a simulation time period. The surface temperature shows a diurnal variation and the one in the AR case with the aerosol radiation effects indicates a distinct decrease after 36 h (Figure 3.4a). The simulated latent heat fluxes at the surface also show similar trends as those of the surface temperature, but the AR case shows almost equal and larger values than the other two cases from a night to early morning, about 28:00 ~ 28:12 UTC and 29:00 ~ 29:12 UTC (Figure 3.4b). This is concerned with the peaks of LWP and IWP and the decrease surface air temperature during the almost same time periods of high latent heat fluxes in the AR case. It means there are large amount of evaporation of water at the surface (sea surface) associated with the change of the vertical temperature profile and more condensations of water vapor in the

(a) Simulated surface air temperature

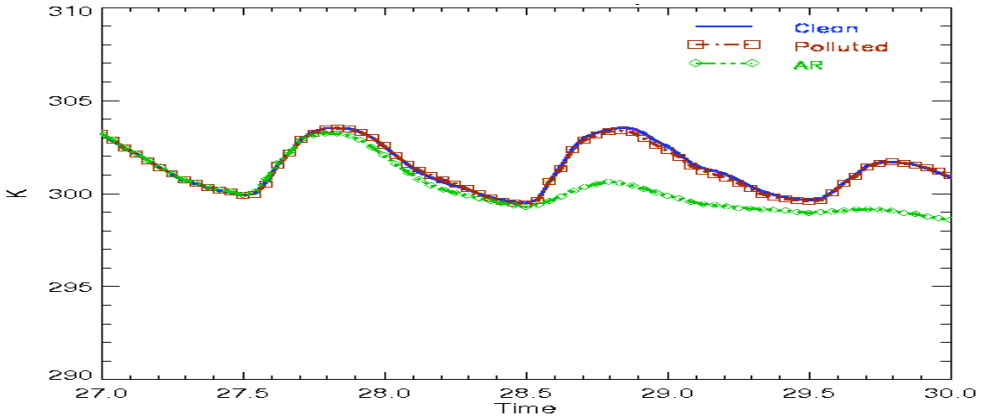

(b) Simulated latent heat flux at surface

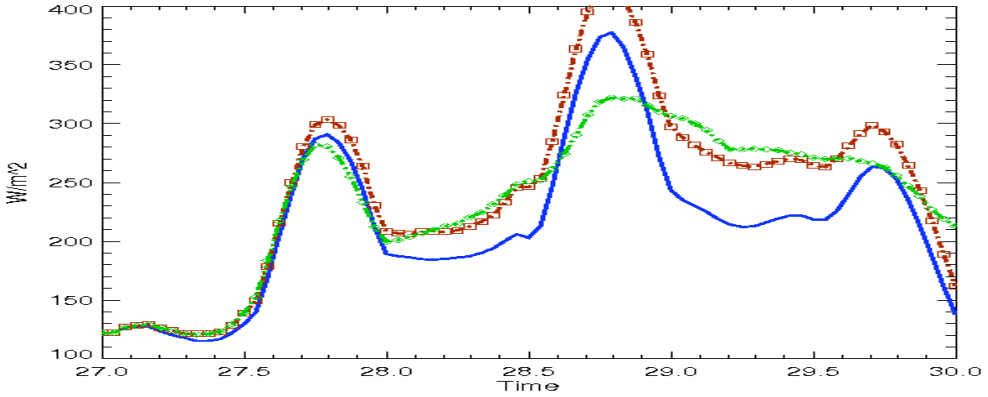

(c) Simulated surface wind speeds

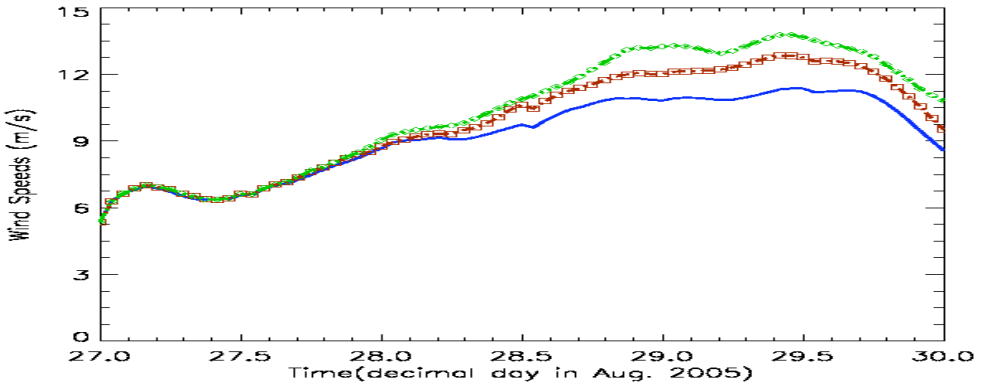

Figure 3.4. Same as in Figure 3.1 but for (a) surface air temperature, (b) latent heat flux, and (c) surface wind speeds.

troposphere subsequently. Figure 3.4c shows the temporal evolution of surface wind speeds averaged over the inner domain grids. The difference of surface latent heat flux in Figure 3.4b can be explained the surface wind speeds. The lowest value of latent heat flux in the AR case is mainly due to the decrease of surface temperature in Figure 3.4a even it shows the highest surface wind speeds. However, the difference between the clean and polluted cases can be related with the variation of surface wind speeds. Therefore, higher latent heat flux in the polluted case is correlated with the increase of surface wind speeds and it may also correspond to the modification of hurricane wind fields due to the aerosol indirect effects.

The convective motions in the hurricane are very complex and mixtures of various convective systems in the eyewall and rainband areas. Therefore, it is also needed to analyze the cloud microphysical, dynamic, and thermodynamic fields in the matter of the hurricane structures.

3.3 CLOUD STRUCTURES OF THE SIMULATED HURRICANE SYSTEM

Based on the temporal evolution of three simulated hurricane systems in Figure 3.1, three simulation times are selected after 24 h (00 UTC 28th), 48 h (00 UTC 29th), and landfall of 60 h (12 UTC 29th). These time periods represent the starting stage of the hurricane development, the strongest hurricane intensity, and the weakening stage of the hurricane due to a landing, respectively. In the clean case with low aerosol concentrations (Figure 3.5a), the vertical-radial cross sections of the azimuthally

(a) Clean

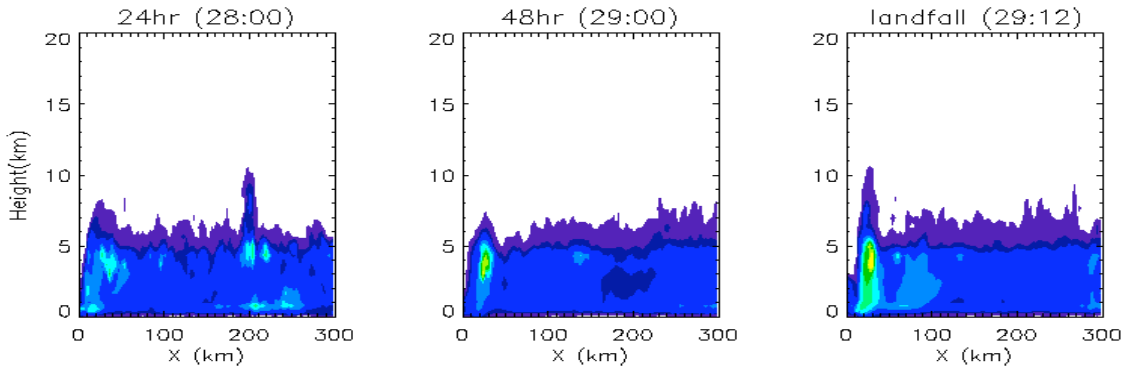

(b) Polluted

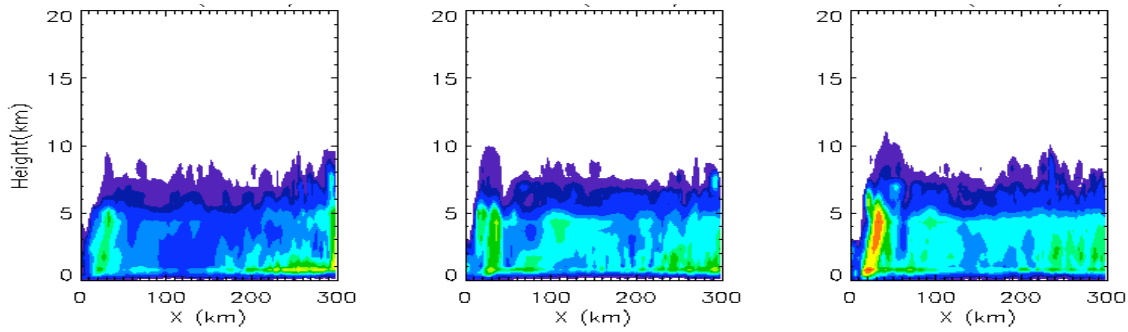

(c) AR

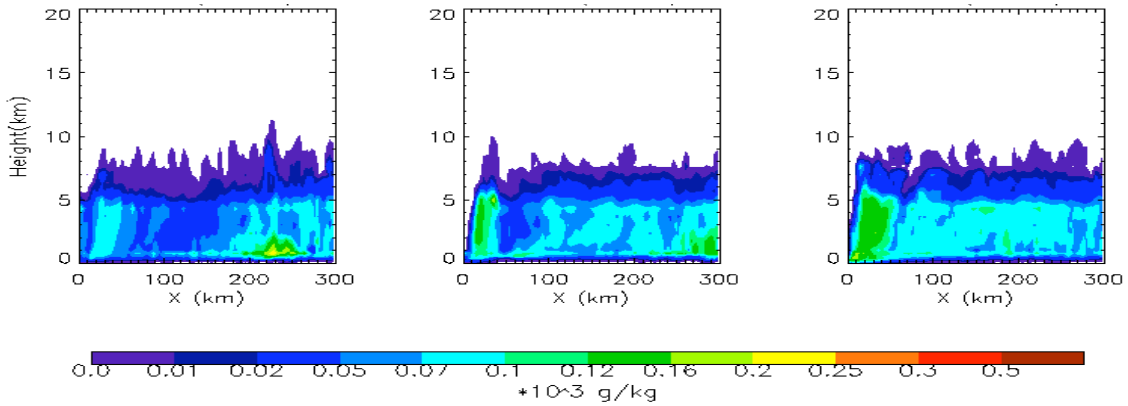

Figure 3.5. Vertical-radial cross sections of the azimuthally averaged cloud water content (CWC) in three simulations of (a) the clean, (b) polluted, and (c) AR at different times: t=28:00, 29:00, and 29:12 (day in August 2005: hour UTC).

averaged cloud water content (CWC) is concentrated in the eyewall and begins to show the outward-tilted structure at the stage of a hurricane development (48 h and landfall). Most of cloud water is located below 5 km and its high concentration is related with the vertical motion since the cloud water is initiated by the condensation of supersaturated water vapor. The sharp tower structure of the cloud water around the eyewall and another high values at 200 km outside the eyewall at the initial stage of 24 h are closely associated with the outward-tilted updrafts in the eyewall and the activity of convective rainbands, respectively. The polluted and AR cases show much large amounts of concentration from the eyewall to rainbands regions due to their high aerosol concentrations (Figure 3.5b and Figure 3.5c). Also the vertical margins of concentrated cloud water content are higher than that in the clean case from 5 km to 6 ~ 7 km at outside the eyewall and it means more active convections in this region. However, the slopes and areas of high concentrated cloud water content in the eyewall are less steep and wider than the clean case after 60 h. It suggests the weakening of the hurricane due to high aerosol concentrations and the aerosol radiative effects.

Ice contents from nucleation and freezing of supercooled cloud water and growths by deposition of water vapor in the eyewall can be transported outward by the outflow and produce a stratiform cloud in the upper troposphere [*Wang*, 2002]. For this reason, the simulated ice contents in the hurricane system are mainly located in the eyewall and upper troposphere above 5 km outside the eyewall (Figure 3.6). Even the clean case (Figure 3.6a) shows the largest ice content in the eyewall because of its strong updrafts, significant amounts of ice contents in the polluted and AR cases are increased

(a) Clean

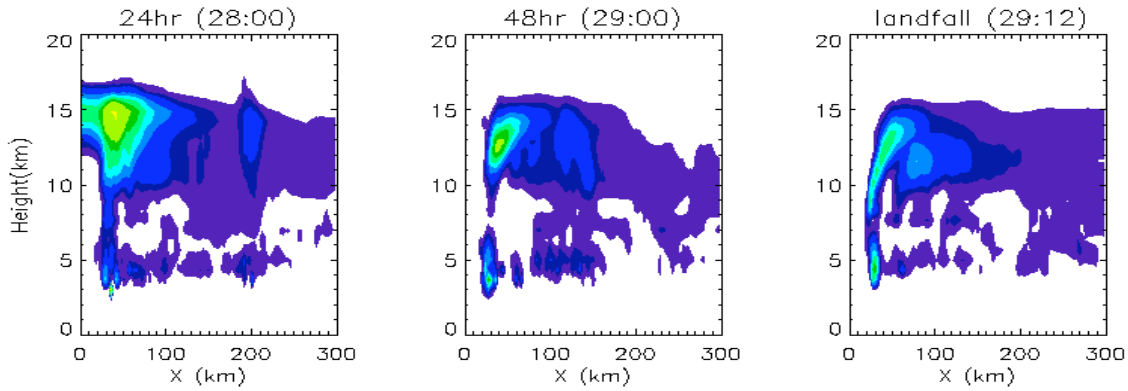

(b) Polluted

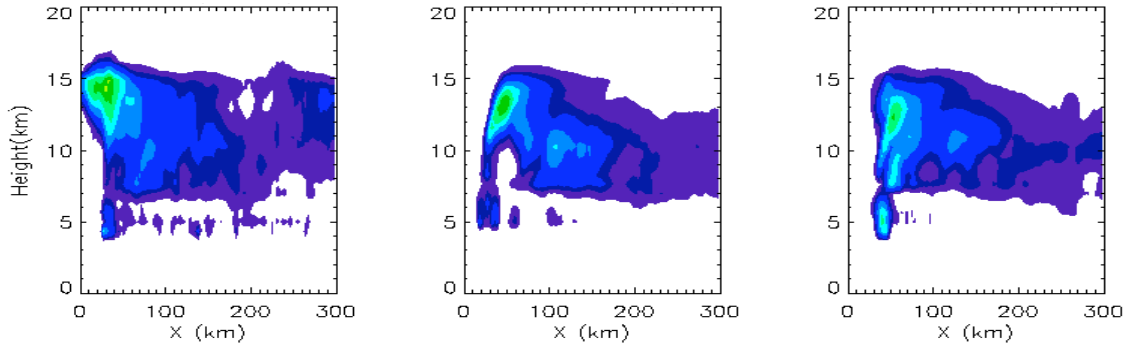

(c) AR

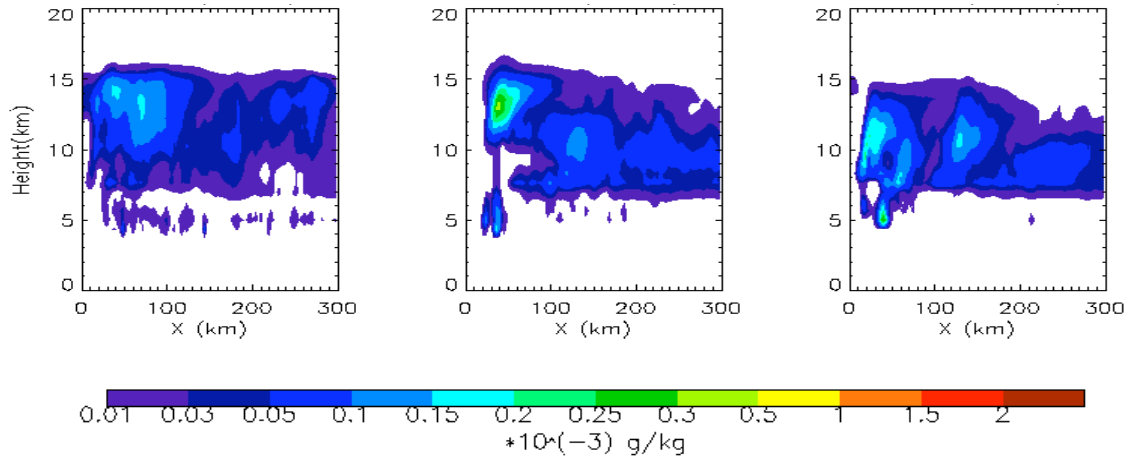

Figure 3.6. Same as in Figure 3.5 but for ice content.

in the upper troposphere of the hurricane rainbands throughout the whole simulation time periods (Figure 3.6b and Figure 3.6c). The increases in two polluted air cases are associated with more cloud water or water vapor contents due to their high aerosol concentrations in the lower troposphere and active updrafts at the rainbands region. In particular, the growth in the AR case is noticeable at the periphery of the hurricane, which means more ice formations from the increased cloud water and water vapor than those in the polluted case and updrafts in rainbands (Figure 3.6c).

Snow from cloud ice and supercooled cloud water is located in the upper troposphere with its maximum concentration in the 10 ~ 15 km layer (Figure 3.7). The distinct increases and thick layers in the polluted and AR cases (Figure 3.7b and Figure 3.7c) are dominant and its distribution is similar to that in ice contents (Figure 3.6b and Figure 3.6c). Graupel can be produced by the conversion of snow or collecting liquid and solid particles after freezing of rainwater when it falls through the melting level [*Wang*, 2002]. Therefore, the layer of the concentrated graupel contents show more extended distributions than those of ice and occurs just above the melting level of 4 km (Figure 3.8). The differences of graupel between the clean (Figure 3.8a) and two polluted cases or the polluted and AR cases (Figure 3.8b and Figure 3.8c) are not significant, but we can see the small amount of increase in the polluted and AR cases outside the eyewall because of the existence of updrafts. This insignificant change in graupel may be explained by a quick conversion into rain in warm and the humid state of the hurricane system.

(a) Clean

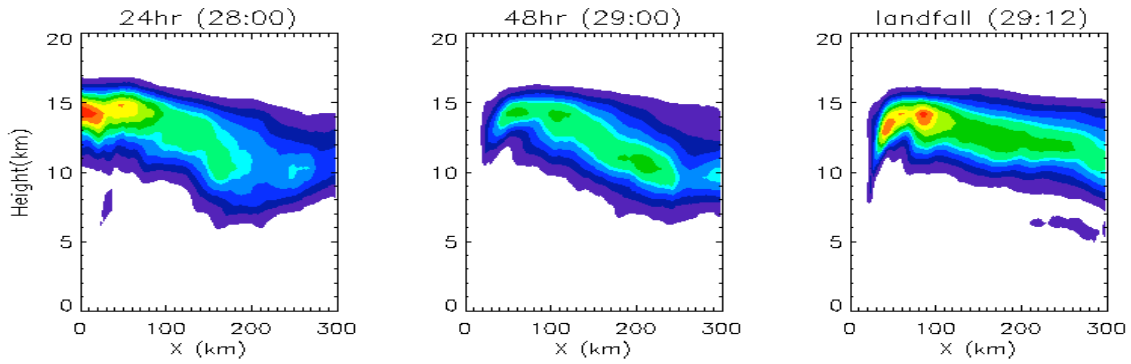

(b) Polluted

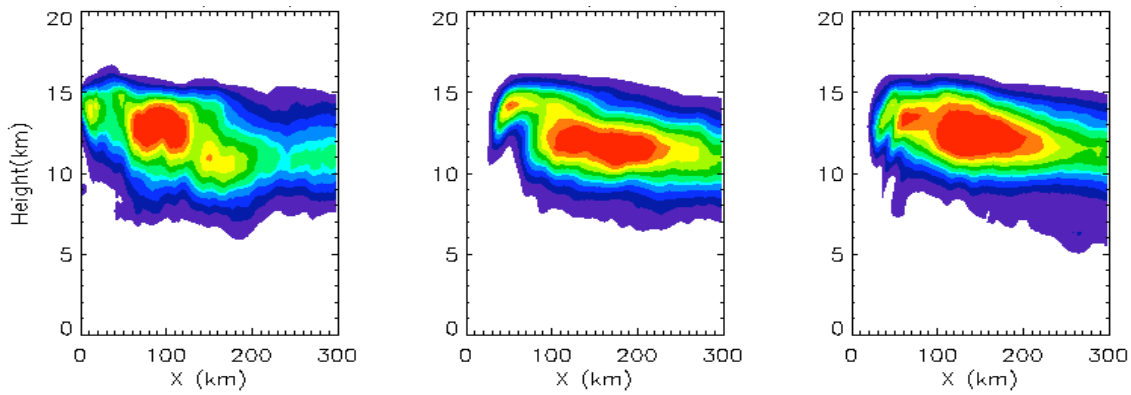

(c) AR

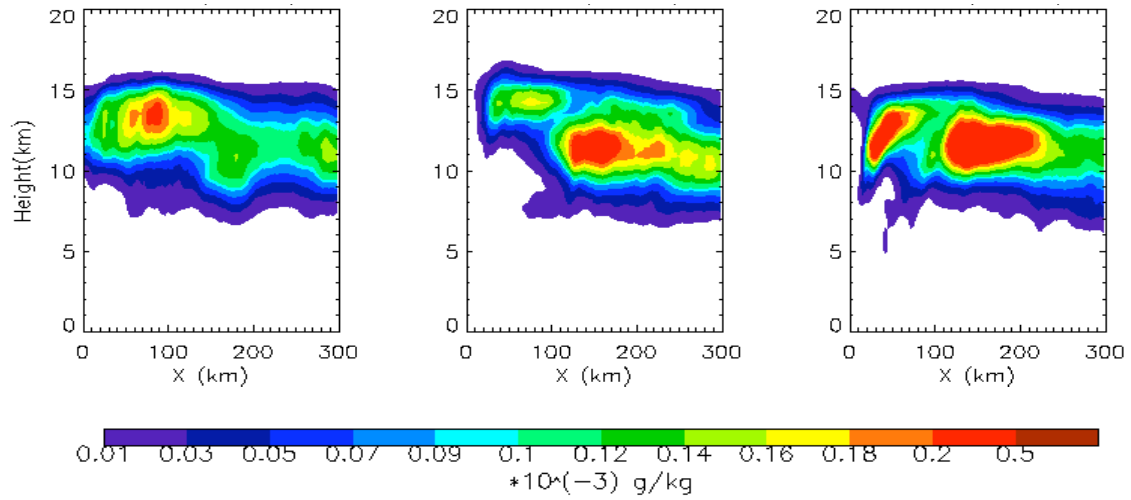

Figure 3.7. Same as in Figure 3.5 but for snow flake.

(a) Clean

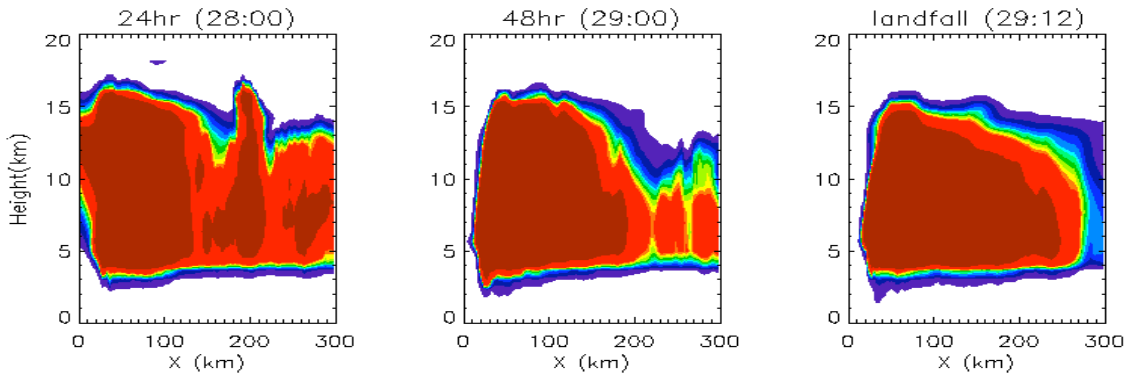

(b) Polluted

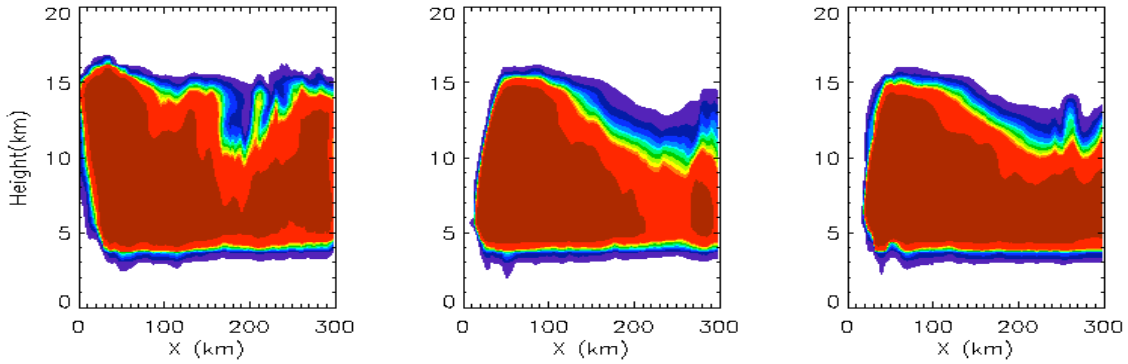

(c) AR

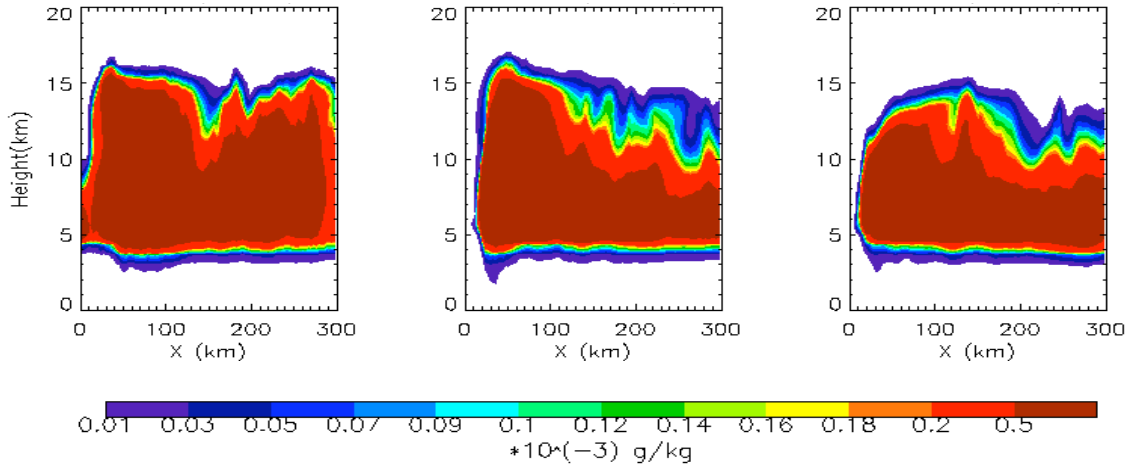

Figure 3.8. Same as in Figure 3.5 but for graupel.

Rainwater content by warm and cold rain processes is concentrated below the melting level of 5 km and represents a comparable pattern with that of cloud water contents, such as a slantwise pattern in the eyewall and rainbands at the periphery of the hurricane (Figure 3.9). All simulated rainwater contents show the peak values in the eyewall and the clean case has the highest contents within the narrow eyewall region due to its strongest intensity of updrafts (Figure 3.9a). According to the structure of precipitation in the hurricane system, the rain water in the eyewall is mainly formed by the warm rain process with cloud water contents and its strong convective motion, while that in outside the eyewall is produced by more complex processes including the mixed phase rain process. As mentioned before, the ice, snow, and graupel transported by strong updrafts from the eyewall and lower troposphere can attribute the formation of stratiform precipitations at rainbands regions. For this reason, the polluted and AR cases (Figure 3.9b and Figure 3.9c) suggest more expanded and stratiform rainbands outside the eyewall than those in the clean case.

The changes in cloud hydrometeors structures also can be seen from the vertical radial cross sections of radar reflectivity calculated with the simulated hydrometeors shown in Figure 3.5 ~ Figure 3.9 (Figure 3.10). In the clean case, sharp vertical gradients of a high reflectivity greater than 30 dBZ occur and penetrate into near the freezing level in the eyewall and some high reflectivity areas at 100 ~ 200 km are associated with the rainbands outside the eyewall with relatively weaker stratiform clouds (Figure 3.10a). In the polluted case, even its weak intensity of radar reflectivity in the eyewall, the region grater than 20 dBZ which means weak stratiform cloud extends outside the eyewall

(a) Clean

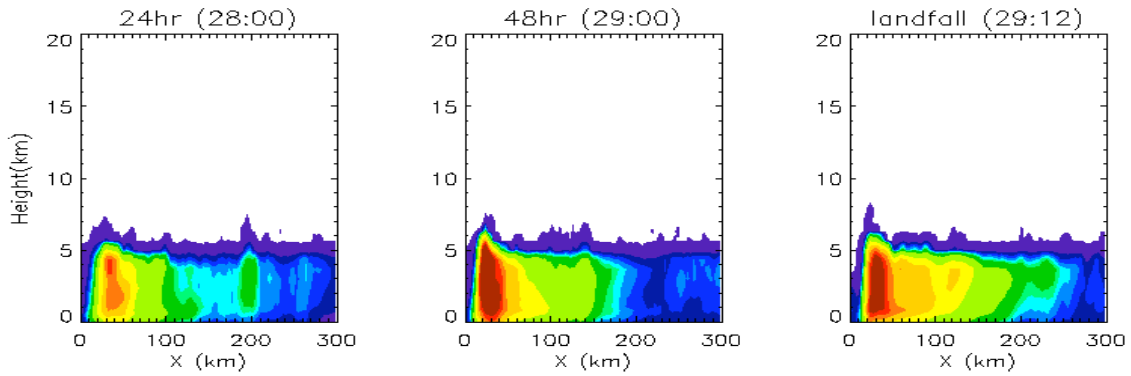

(b) Polluted

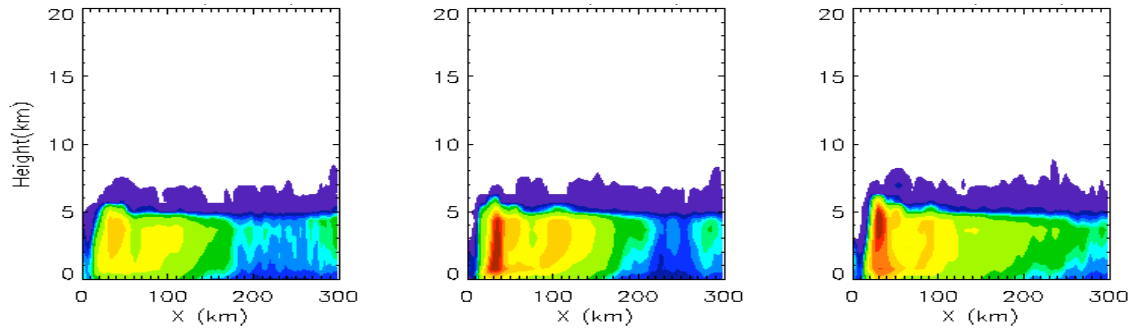

(c) AR

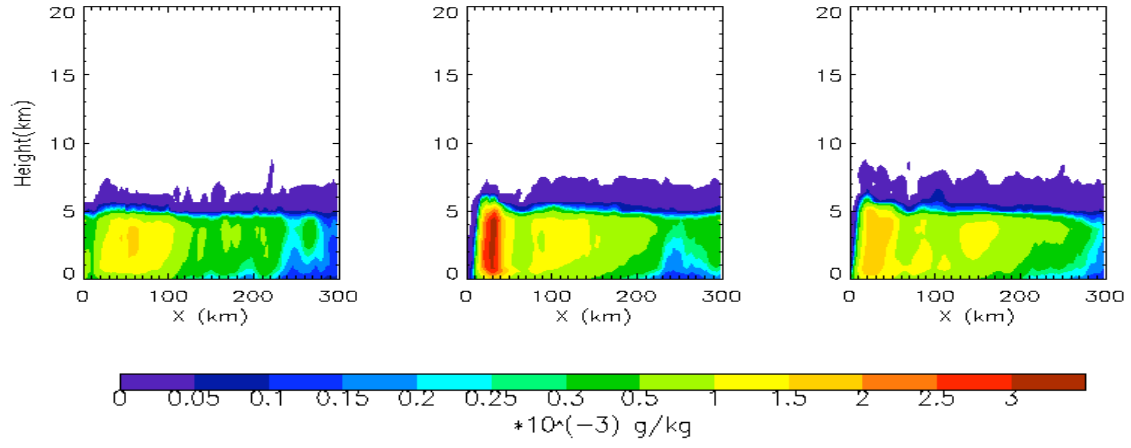

Figure 3.9. Same as in Figure 3.5 but for rain water content.

(a) Clean

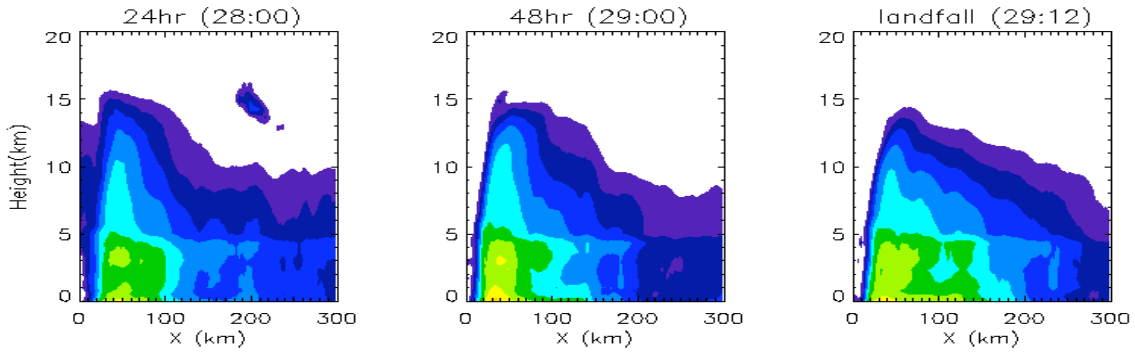

(b) Polluted

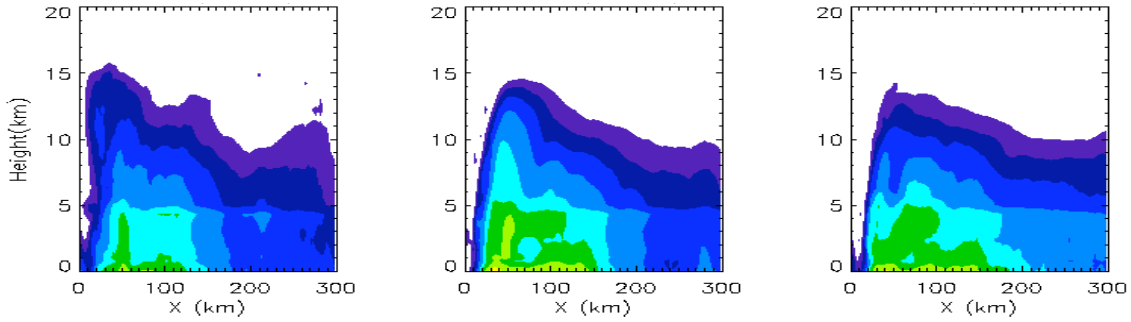

(c) AR

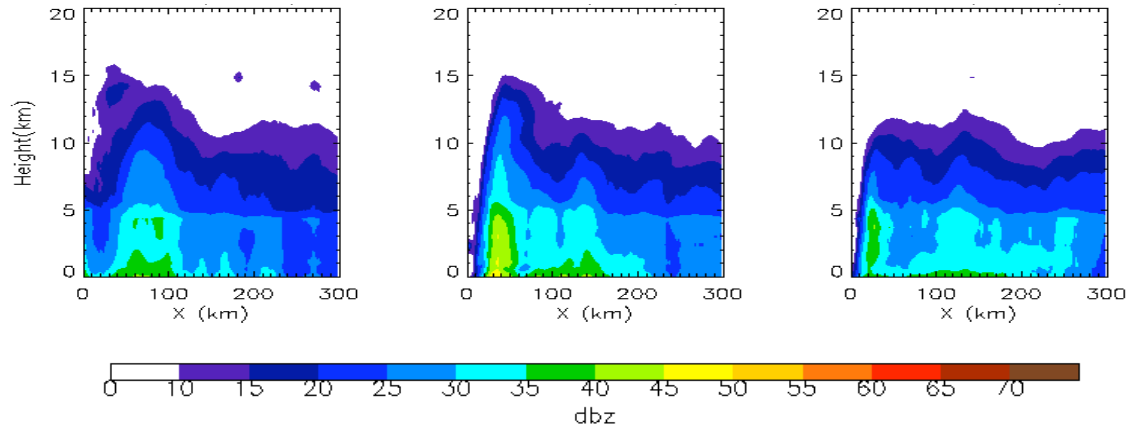

Figure 3.10. Same as in Figure 3.5 but for radar reflectivity.

(Figure 3.10b). Therefore, the polluted case presents more pronounced stratiform clouds in the mid-upper troposphere due to the higher concentration of the rain water, snow, and graupel than that in the clean case. The AR case with the aerosol radiative effects shows the weakest intensity of reflectivity in the eyewall, but more expanded areas of high reflectivity over 30 dBZ than those in the polluted case at the periphery of the hurricane in the troposphere (Figure 3.10c). It means the increase of rainwater outside the eyewall in the AR case. Also the moderate intensity of a radar reflectivity in two polluted air cases at the rainbands regions suggests the active vertical updrafts rather than the clean case. The different distributions between the hydrometeors contents can lead the modifications in the thermodynamic and dynamic fields in three simulated hurricane systems.

Figure 3.11 and Figure 3.12 present the horizontal distribution of aerosol number concentration of ammonium sulfate and sea salt aerosols at the lowest level of the simulation results. The aerosol number concentration is given by initial and boundary conditions during model run. Therefore, they can be transported and supplied from the boundary for each time step. For this reason, the distribution of aerosol number concentration is increased as time step. Two polluted air cases show more enhanced concentrations throughout the simulation time (Figure 3.11b and Figure 3.11c). The low concentrations are also shown around the eyewall regions because they are activated quickly and removed by convective motions and precipitation processes. After landing, we can see the increase of concentrations with their weakening of convective intensity at the eyewall regions. The distribution of sea salt aerosols shows a different pattern of

(a) Clean

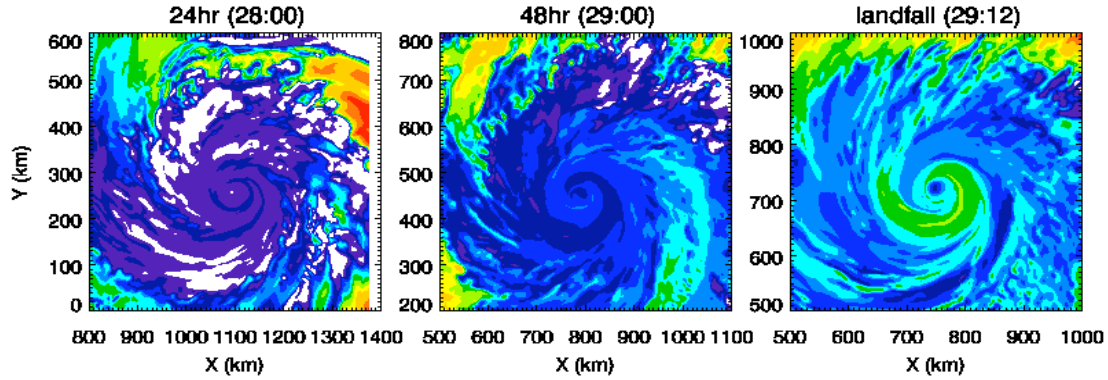

(b) Polluted

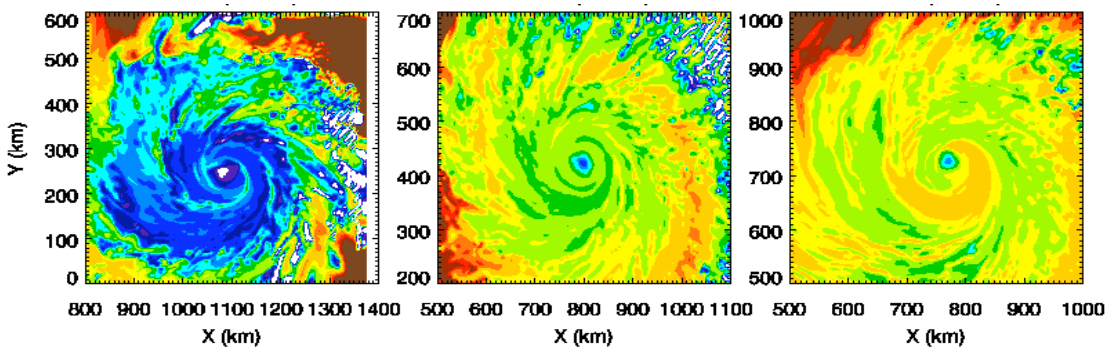

(c) AR

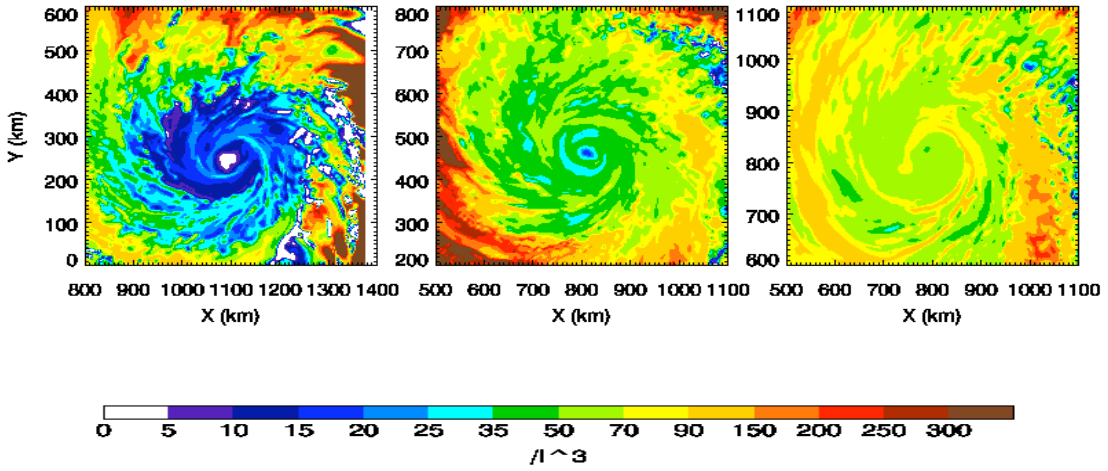

Figure 3.11. Horizontal distribution of ammonium sulfate aerosol number concentration at the lowest model level.

(a) Clean

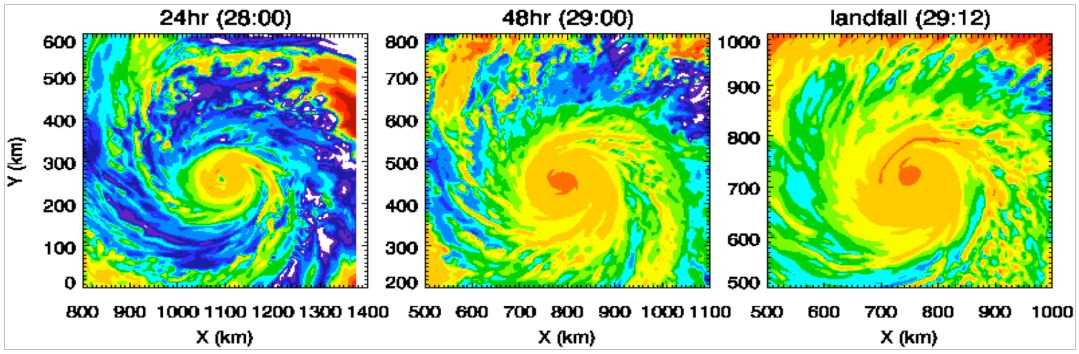

(b) Polluted

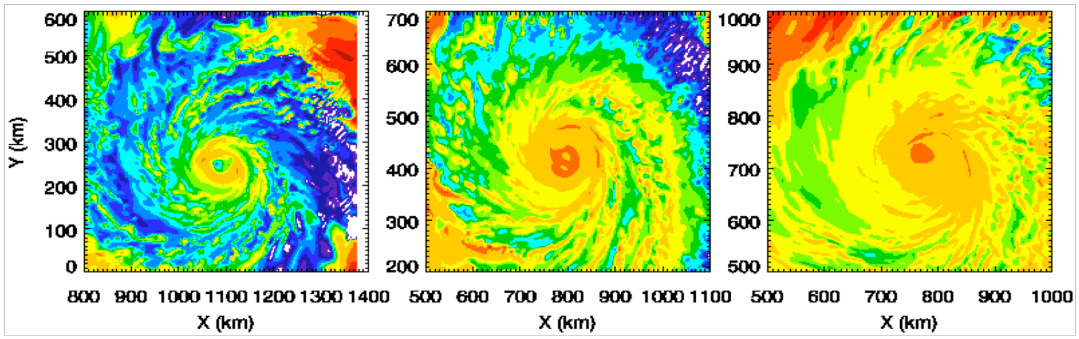

(c) AR

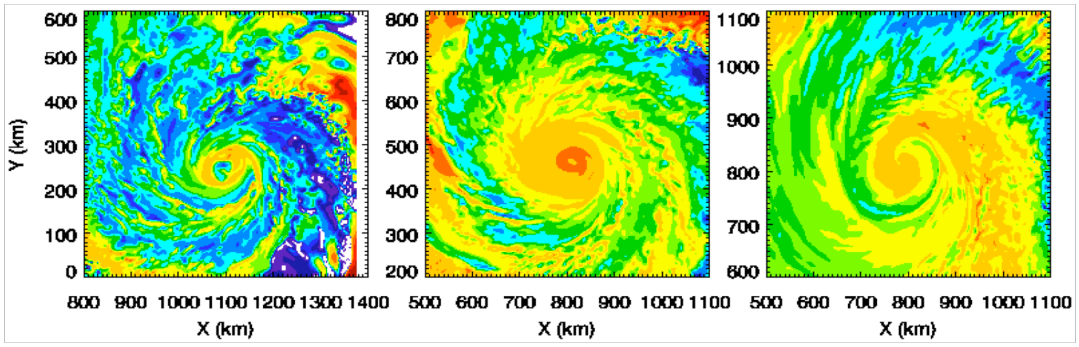

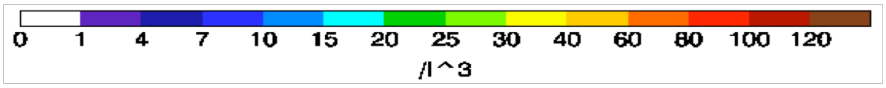

Figure 3.12. Horizontal distribution of sea salt aerosol number concentration at the lowest model level.

ammonium sulfate aerosols. Unlike the ammonium sulfate aerosols, we can sea a relevant increase of number concentration around the eyewall. After 48 h, they are concentrated as the center of hurricane. In the convective region of the eyewall, they can be transported into the eyewall but cannot be removed effectively by convective motions or precipitation processes. *O'Dowd et al*., [1999] show that giant CCNs can reduce the number of cloud droplets under polluted conditions by suppressing the supersaturation reached in a cloud based on their in situ observations and parcel model simulations. The decrease cloud droplet number concentration with presence of giant CCNS cloud lead to increased droplet effective radius [*Lu and Seinfeld*, 2005; *Yuan et al*., 2008].

3.4 THERMODYNAMIC AND DYNAMIC STRUCTURES OF THE SIMULATED HURRICANE SYSTEM

Figure 3.13 shows vertical cross sections of azimuthally averaged vertical velocity in three simulated hurricanes. In the clean case, it presents a typical hurricane vertical structure with a slant-wise vertical updrafts in the eyewall and its related downdrafts in the center of the eyewall (Figure 3.13a). After a period of the hurricane development (48 h), the updrafts outside the eyewall start to develop and be extended horizontally and vertically. This trend is quite similar as those in two polluted air cases even they show less intensity of updrafts. It is not distinct strength but vertical updrafts more than 0.1 m/s in the polluted and AR cases indicate more activity of convections at the periphery of the hurricane from the lower level even their less intensities (Figure

(a) Clean

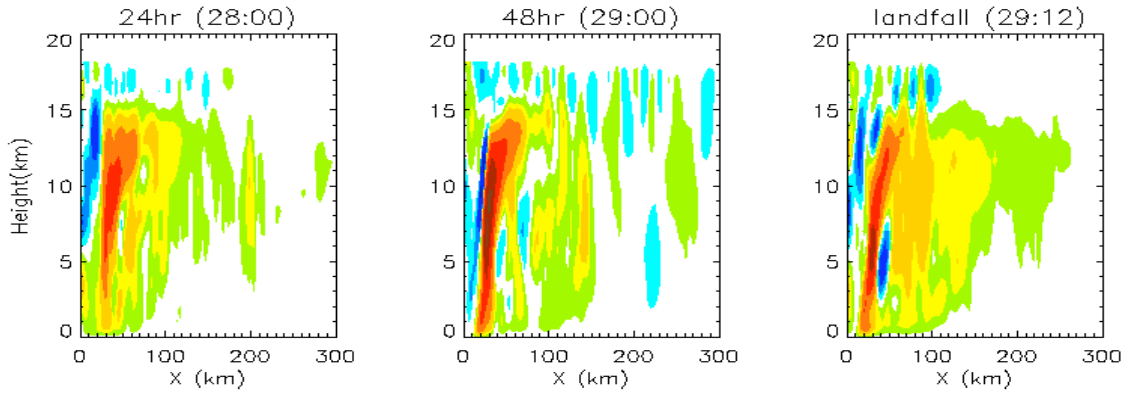

(b) Polluted

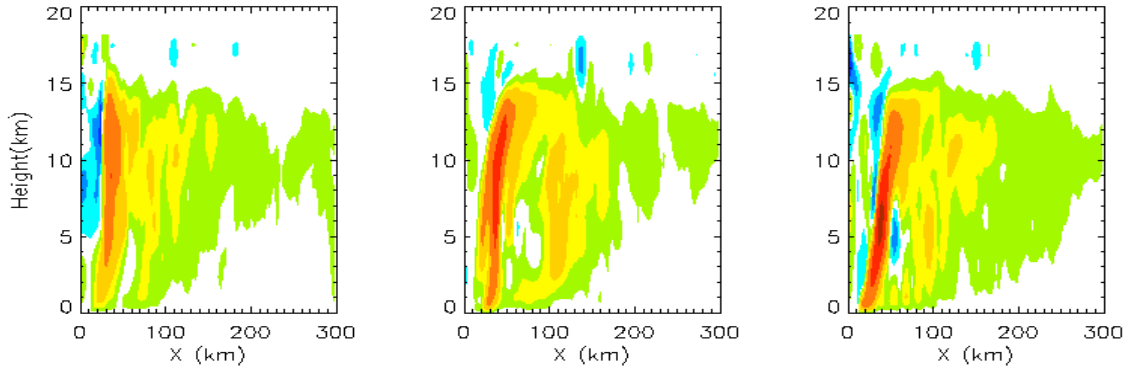

(c) AR

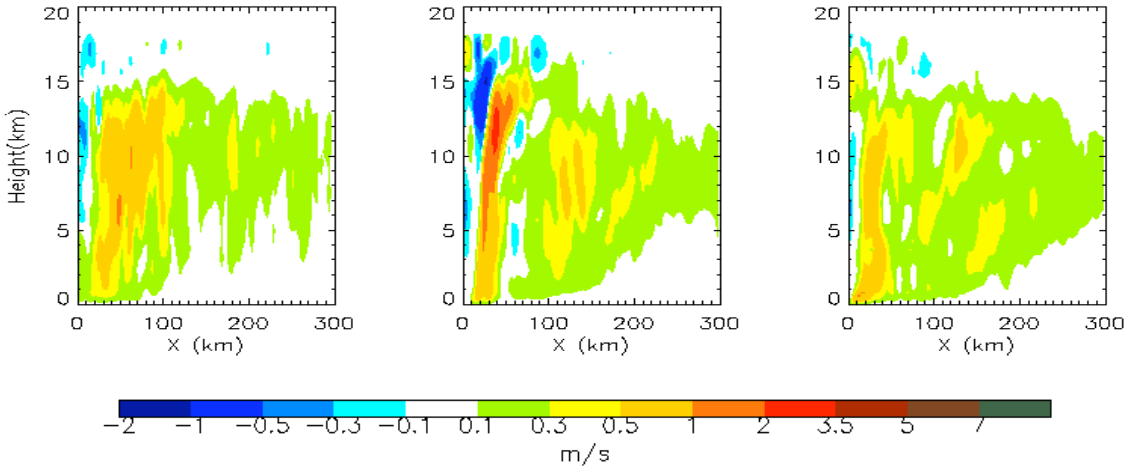

Figure 3.13. Same as in Figure 3.5 but for the vertical velocity.

3.13b and Figure 3.13c). The cores with maximum or high vertical updrafts correspond to the locations of high radar reflectivity areas in Figure 3.10. The strong updraft in the clean case at the radius of 20 ~ 30 km in the eyewall matches with the highest reflectivity at the same location. Also the relative active updrafts in the polluted and AR cases between 100 ~ 200 km outside the eyewall are equivalent to rainbands at the periphery of the hurricane. However, the peak of updrafts velocity in the AR case indicates the weakest intensity and it corresponds to the reducing of overall convective strength due to the aerosol radiative effects. The updrafts outside the eyewall can play very important roles in limiting the intensity of the hurricanes because the mass and moisture air rising in rainbands region due to updrafts can lead the reducing of the low level warm and moist air inflow before reaching the tropical cyclone center. Therefore, it leads to the weakening of the convection intensity at the center of hurricane.

The equivalent potential temperatures (θ_e) concerned with the hurricane vertical-radial cross section are shown in Figure 3.14. Inside the rainband at 50 km radial distance, θ_e related to the stability of atmosphere is well mixed in the vertical due to strong updraft motion. Also there is a warming due to subsidence in the hurricane center. This mixing extends from near the surface to 15 km height. In clean case, there is minimum of 336 K at 5 km height outside of 250 ~ 300 km radius during a strong hurricane stage (48 h) and this minimum of θ_e corresponds to the field that dew point depressions are typically 5 ~ 6 ℃ (Figure 3.14a). When we compare with the low θ_e area less than 352 K, it retreats to outside the eyewall after 48 h and the vertically well-mixed area in the eyewall is also expended horizontally at radius of 100 km after landing. In the

(a) Clean

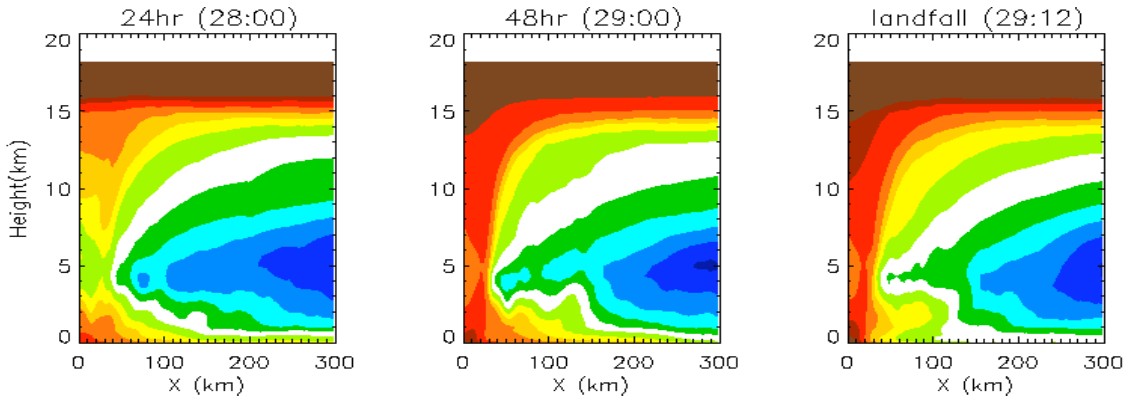

(b) Polluted

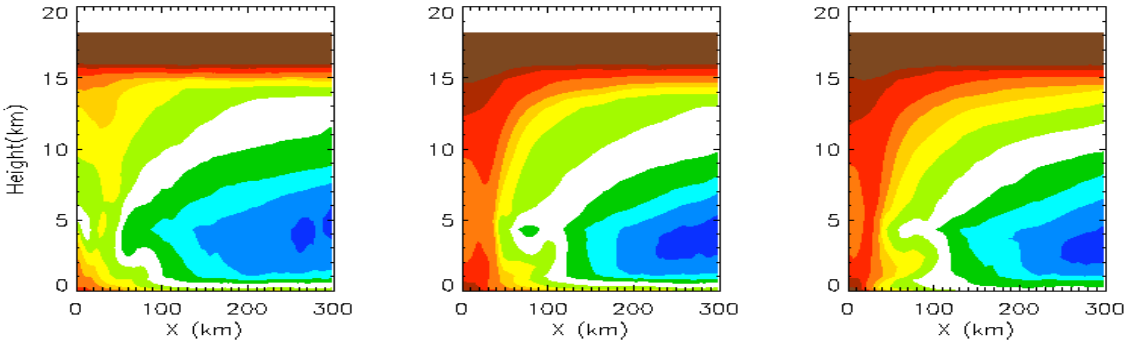

(c) AR

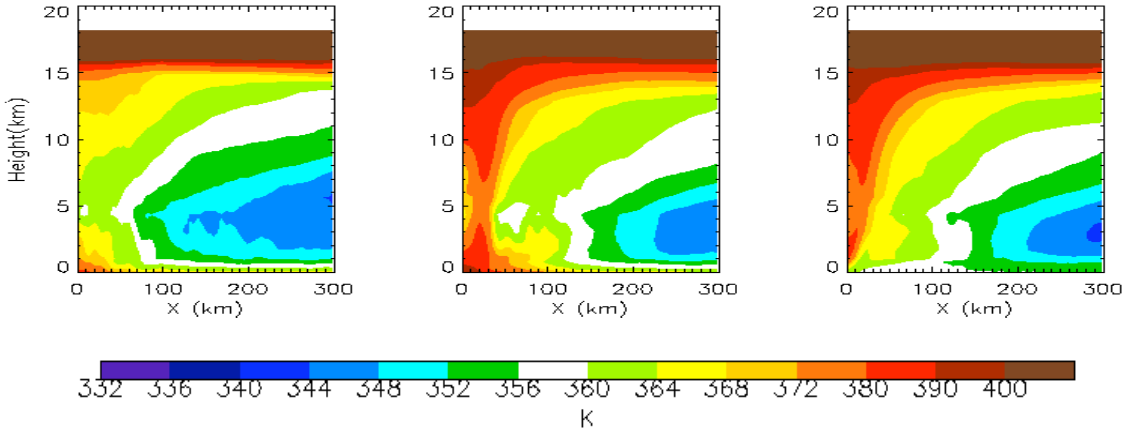

Figure 3.14. Same as in Figure 3.5 but for equivalent potential temperature.

polluted case, horizontally expanded well-mixed θ_e layer related with the strong updraft in the eyewall is located 50 km and relatively small mixed layer at 100 km is shown after 48 h (Figure 3.14b). These locations are equivalent to those of vertical velocity fields in Figure 3.13b. The AR case can not show the prominent eyewall ascents compared with those in the other two cases during the hurricane development (after 48 h), but represents higher θ_e in the troposphere with the weak mixed layers of θ_e at the radius of 100 ~ 150 km (Figure 3.14c). These areas are matched with the location of slight updrafts in Figure 3.10c. Two polluted air cases represent higher θ_e at 5 ~ 15 km in the troposphere, while the clean case shows higher θ_e than those in two polluted air cases in the lower level of 5 km and above the freezing level of 15 km. This increase of θ_e suggests that the polluted air with high aerosol concentrations is able to produce the enhanced latent heat release by more water vapor condensation and extra cloud water droplet freezing with producing ice, snow, and graupel at the lower troposphere and above the freezing level, respectively. More θ_e values in rainband regions also suggest the activity of ascents in outside the eyewall for two polluted air cases even the updraft in the AR case shows less intensity. Moreover, higher θ_e in the AR case than those in the polluted case means the enhanced latent heat release by additional condensation and freezing of more hydrometeors contents. It can be explained that more heating and sequent warming of the atmosphere due to absorbing aerosols in the AR cases can lead the enhanced hydrometeors contents and play a role in increasing of latent heat release. For the detailed comparison of vertical structures of θ_e at periphery of the hurricane, Figure 3.15 contains vertical profiles of derived from Figure 3.14. Each line indicates the θ_e at 150

(a) Clean

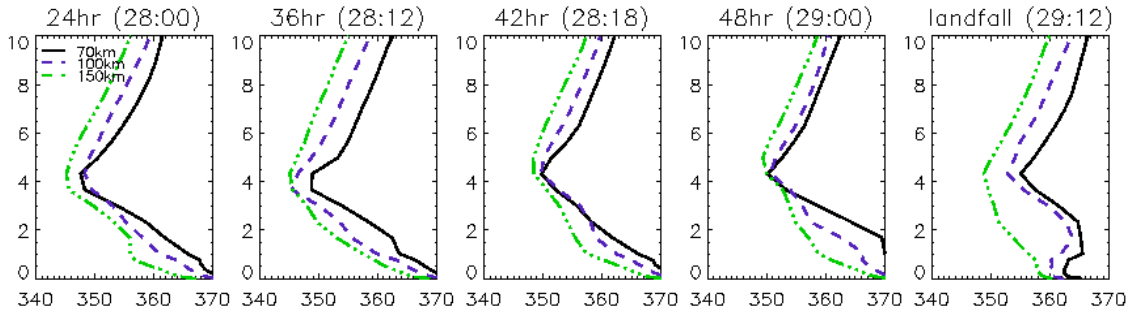

(b) Polluted

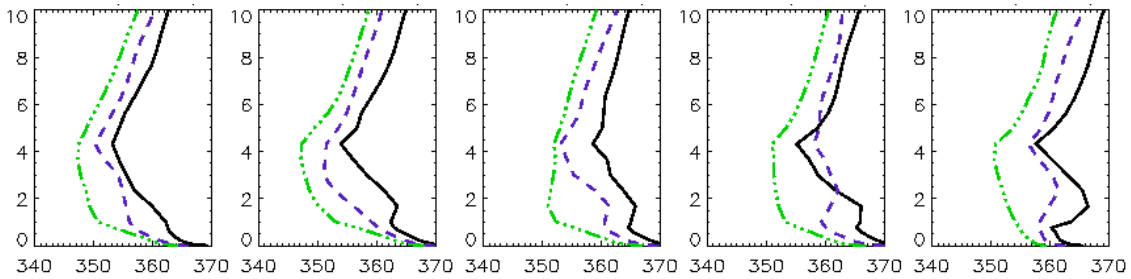

(c) AR

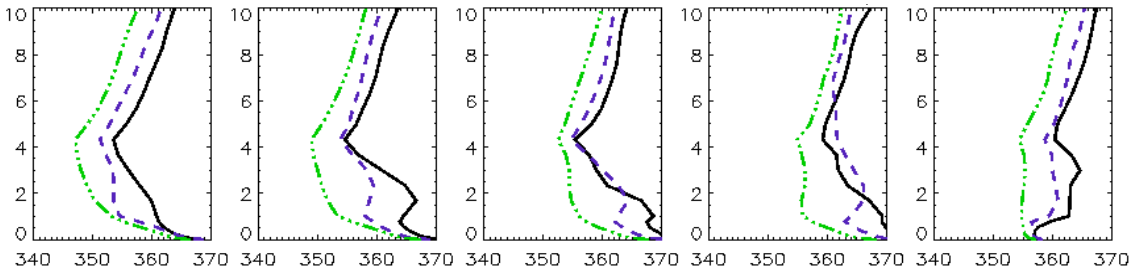

Figure 3.15. Azimuthally averaged outside the band of 70, 100, and 150 km equivalent potential temperature in three simulations of (a) clean, (b) polluted, and (c) AR at different times: t=28:00, 28:12, 28:28, 29:00, and 29:12 (day in August 2005:hour UTC).

km radial distance of outside edge the rainband, 100 km radial distance of middle of the rainband and 70 km radial distance of the inside edge of the bands, respectively. Unlike the θ_e profile in the clean case (Figure 3.15a), increases of θ_e in the polluted and AR cases (Figure 3.15b and Figure 3.15c) are observed in the layer 1 ~ 2 km above the ocean surface as radial distance decreases (70 and 100 km), which means more latent heat release by the enhanced cloud water due to high aerosol concentrations with the unstable and convective air in rainband regions. The AR case presents higher value of θ_e throughout the layer at 100 km and 150 km radial distances and, in particular, the θ_e profile at 150 km radius shows the vertically neutral layer at 1 ~ 4 km height and its slope becomes slightly positive with height as the one at 100 km radial distance. It presents the AR case has more latent heat release and additional hydrometeors contents in rainband regions due to its warming in the troposphere by the aerosol radiative effects.

The warming of the atmosphere due to absorbing aerosols in two polluted cases can be seen in the vertical-radial cross section of heating rate (K) by longwave and shortwave radiations in Figure 3.16 and only shortwave radiation in Figure 3.17, respectively. The polluted case presents a prominent warming layer between 5 ~ 12 km above the freezing level and it is also related with the increase of latent heat release around this layer (Figure 3.14b), which means enhanced freezing by cloud droplets into ice, snow, and graupel by adding more aerosol concentrations (Figure 3.16a). In the AR case, main heating is located at 10 km height as the polluted case, but indicates more enhanced warming than the polluted case between 2 ~ 10 km heights (Figure 3.16b). In comparing with the heating rate in Figure 3.17, the increase of warming in the AR case

(a) Polluted

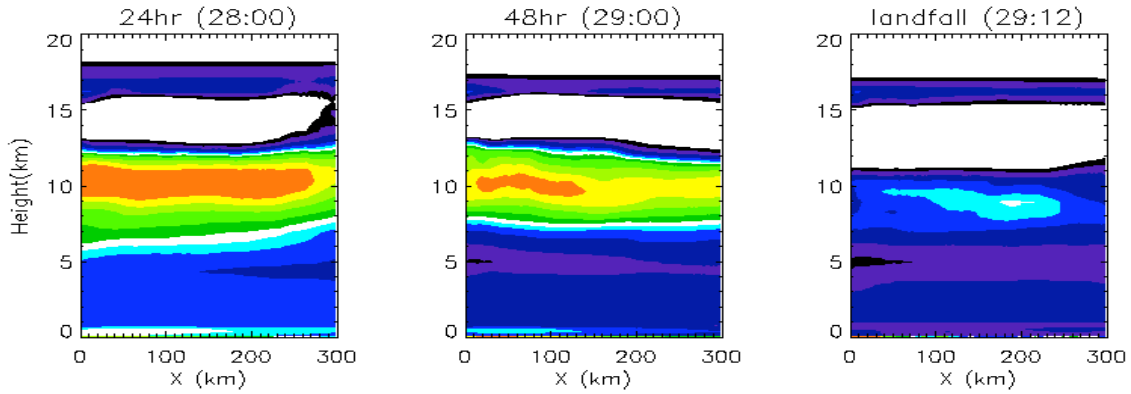

(b) AR

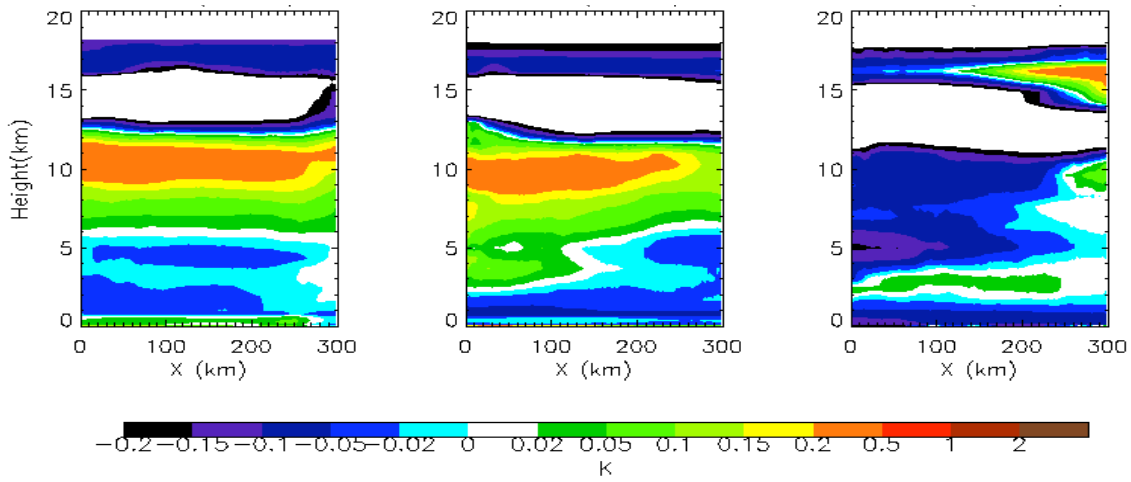

Figure 3.16. Same as in Figure 3.5 but for heating rate by longwave and shortwave radiation of (a) the polluted and (b) the AR cases.

(a) Polluted

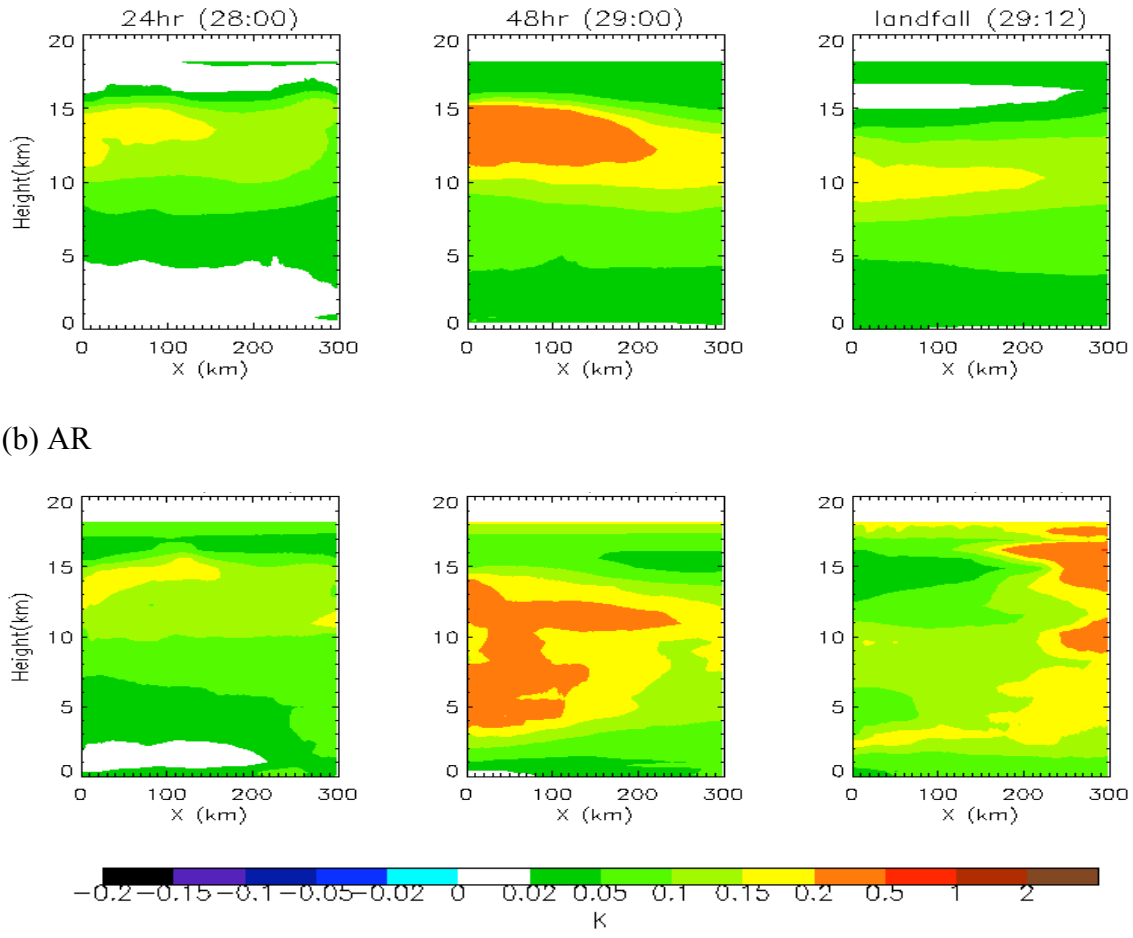

Figure 3.17. Same as in Figure 3.5 but for heating rate by only shortwave radiation of (a) the polluted and (b) the AR cases.

is mainly due to the absorption of shortwave radiation by aerosols. The vertical height-time diagram of the horizontally averaged heating rate by shortwave plus longwave (Figure 3.18) and only shorwave radiations (Figure 3.19) over inner domain are illustrated from 00 UTC 28th to 12 UTC 29th time periods. As in Figure 3.16 and Figure 3.17, there are dominant positive heating rate at 10 km heights in both cases, but this heating layer around the freezing level is extended to 6 km heights and the weakening of cooling which means warming in the lower atmosphere also appears in the AR case (Figure 3.18b). In heating rate by only shortwave radiation, the locations of warming in the AR case (Figure 3.19b) are getting lower and expanded into the surface layer than those in the polluted case (Figure 3.19a). The heating rate distribution by absorbing aerosols can lead the difference of heating rate between the polluted and AR cases and the warming in the lower atmosphere can contribute to a more stable air with its lower surface temperature in the AR case. The warming in the atmosphere also affects the relative humidity. Figure 3.20 represents the vertical-radial cross section of relative humidity of three simulated hurricane systems. There are high relative humidity areas; around hurricane centers with condensation processes, above the freezing levels from 5 km to 10 km heights associated with the freezing of cloud droplets outside the eyewall, over the surface, and below 5 km at rainband regions related with the condensation, precipitation and evaporation of water vapor. The relative humidity of the polluted case represents higher humidity at the periphery of the hurricane than that in the clean case due to its aerosol high concentrations (Figure 3.20b). The AR case also shows higher relative humidity than one in the clean case at rainbands region, but there are weak

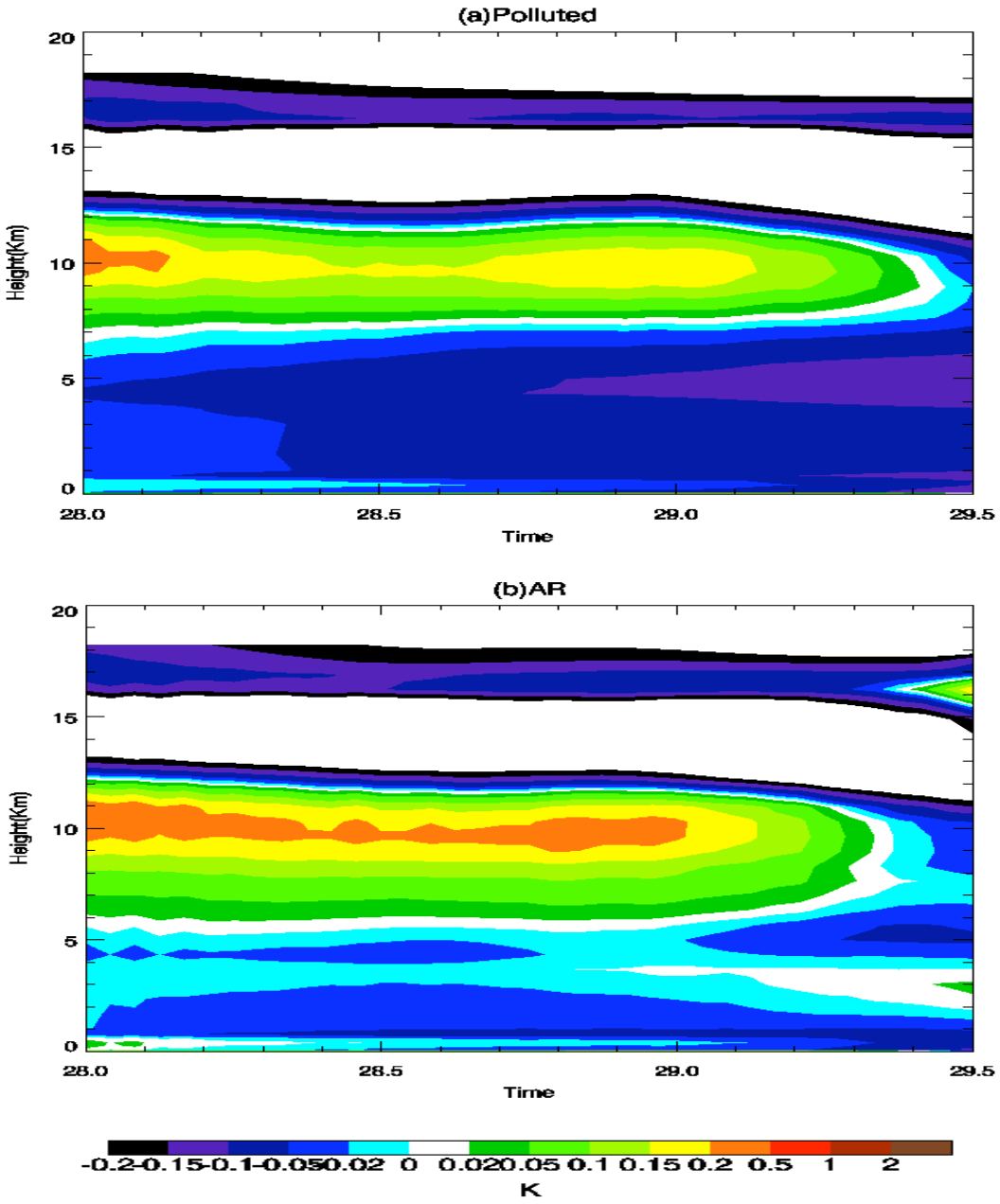

Figure 3.18. Time-altitude diagram for horizontally averaged over inner domain heating rate by longwave and shortwave radiation of (a) the polluted and (b) the AR cases from 00 UTC 28th to 12 UTC 29th.

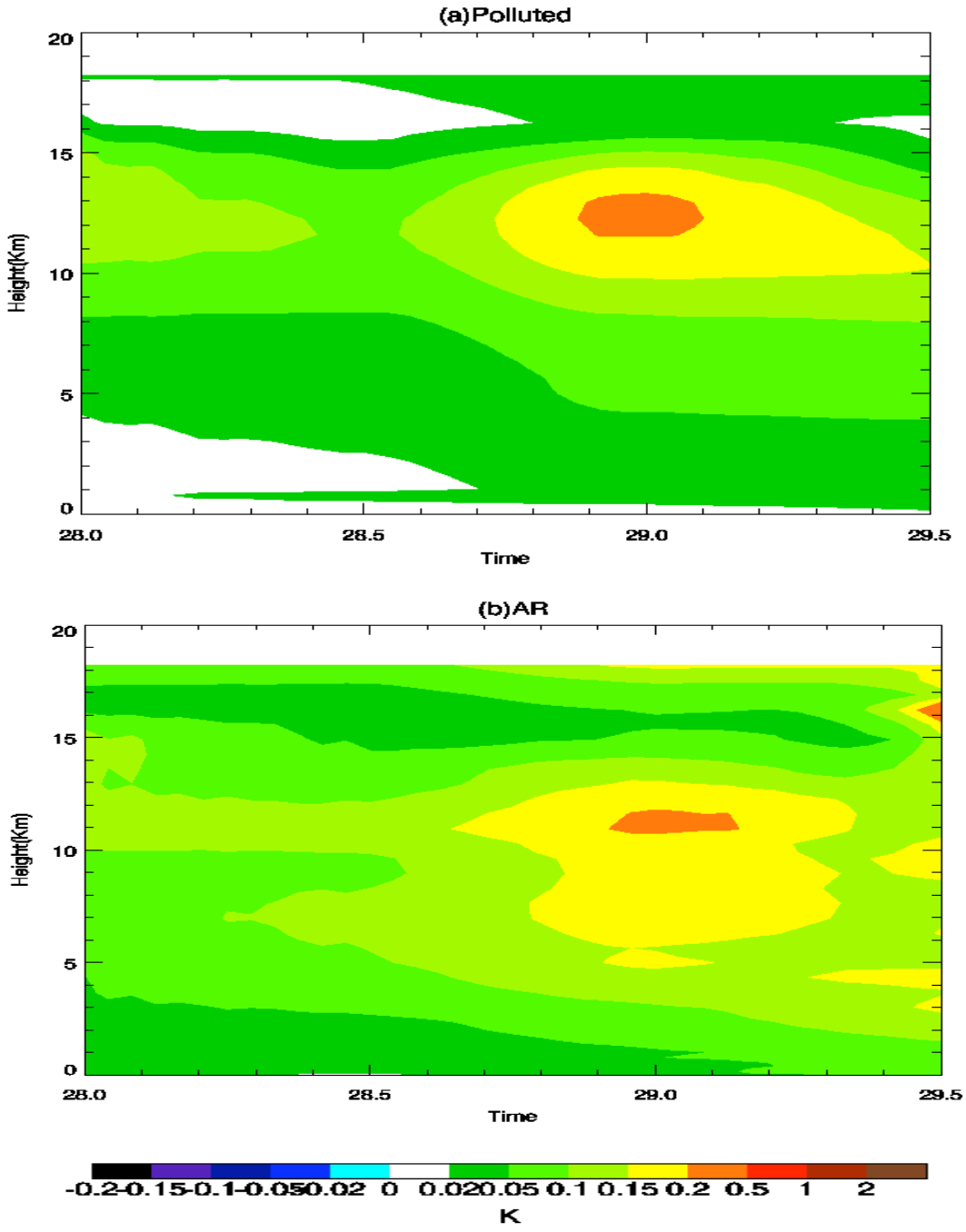

Figure 3.19. Same as in Figure 3.18 but for heating rate by only shortwave radiation.

humidity areas above the freezing level compared with those in the polluted case due to a warming of this layer in Figure 3.16 and Figure 3.17 (Figure 3.20c).

In summary, from the difference of vertical structures in the hurricane system, the thermodynamic and dynamic structures are quite sensitive to the aerosol indirect effects by high aerosol concentrations and the aerosol radiative effects by absorbing shortwave radiation aerosols. By adding more aerosol concentrations, active vertical motions can be proposed to outside the eyewall with a weakening of hurricane intensity in center. On the other hand, more heating in the lower atmosphere by absorbing aerosols can attribute to suppress the convective motion at the rainband regions with a more stable vertical structure. At the same time, it can hold more hydrometeors contents in the troposphere with releasing a latent heat. The influence of aerosol effects in thermodynamic and dynamic fields is also investigated in the rainbands of the hurricane system because the rainbands play main roles in changing the intensity of the hurricane.

3.5 RAINBANDS AND CONVECTIVE ACTIVITY

The discussion of the hurricane rainbands by previous studies suggests that it consists of convective scale cells embedded in a stratiform precipitation and large rainband spirals connected with the storm center. *Barnes et al*. (1983) showed a stratiform and convective structure of the band using reflectivity observations and suggested that the updrafts end of the band was categorized as convective, and the bands

(a) Clean

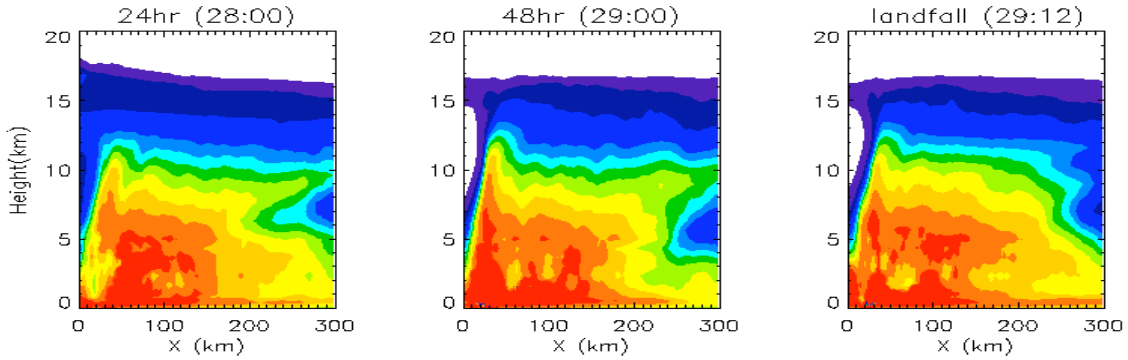

(b) Polluted

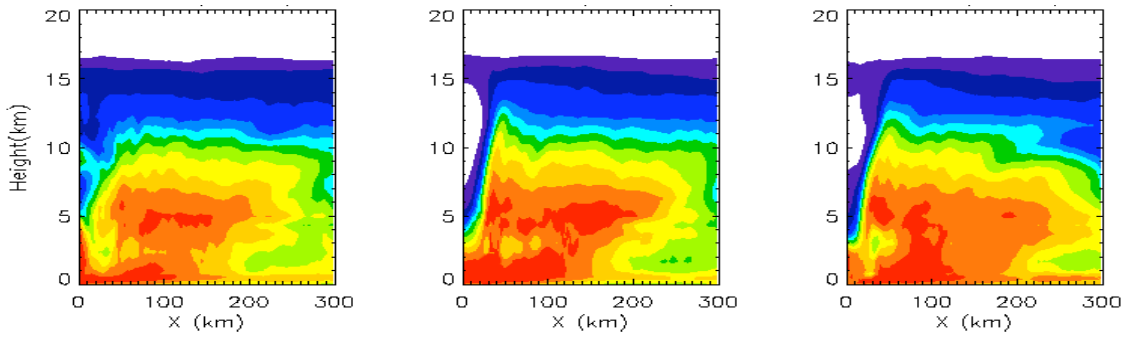

(c) AR

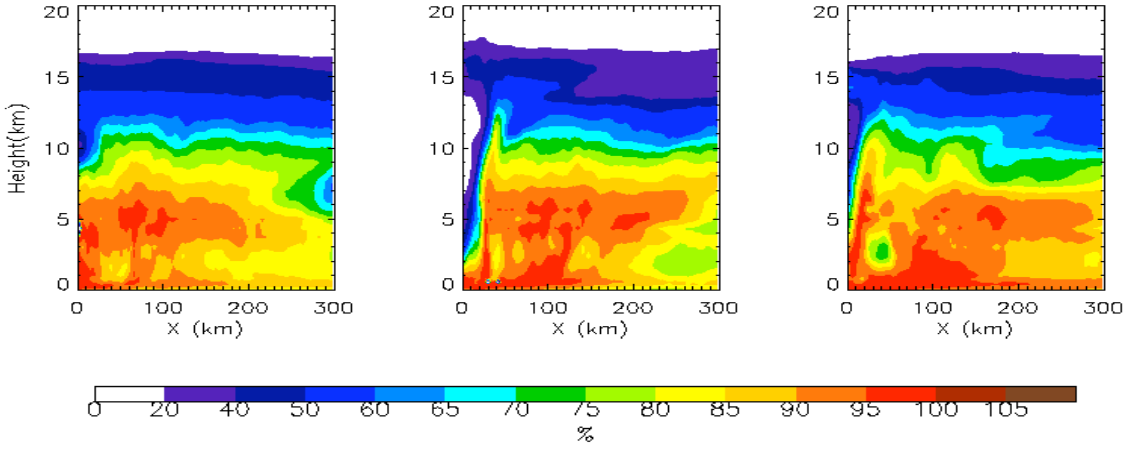

Figure 3.20. Same as in Figure 3.5 but for relative humidity.

gradually became less convective and stratiform precipitation was dominant toward its downdrafts end of the band. The rainband and its related convective activities can influence in limiting the intensity of tropical cyclones [*Barnes et al*., 1983; *Powell*, 1990a, b; *Wang*, 2002]. Generally, downdrafts form just inside the rainbands and are originated by the melting of ice, snow, and graupel and evaporation of rain. During these downdrafts occur, dry and cold air with low θ_e from the middle troposphere is brought into the inflow boundary layer and the air with θ_e is advected into the eyewall by the boundary layer inflow, thus contributes to suppress the convection in the eyewall and reduce the intensity of the hurricane. Moreover, the mass and moisture air rising in rainbands due to updrafts can play a barrier role in reducing the low level warm and moist air inflow before reaching the center of tropical cyclone, diminishing the mass and moisture convergence into the eyewall, and thus weakening the hurricane intensity. The correlations between vertical motions and build-up of rainbands are also documented by *Hence and Houze* (2008) and *Didlake and Houze* (2009) using high resolution Doppler radar data. *Hence and Houze* (2008) found that the principal rainbands in the hurricane Katrina (2005) and Rita (2005) had well defined jet along their rainbands axes and the overturning updrafts could act to strengthen the jet and suggested the manifestation of principal rainbands by mesoscale convective cells. The downward motions associated with the convective cells of principal rainbands were also studied by *Didlate and Houze* (2009) using Doppler radar data for the hurricane Katrina (2005). They showed that there are two distinct convective scale downdrafts in the principal rainband. One is an inner-edge downdrafts (IEDs) which is initiated at 6 ~ 8 km heights and induced as a

result of three different downward forcing effects in response to the updrafts cell. At upper levels, the downward pressure gradient force is formed in response to the adjacent buoyant updrafts of the cell. Once descending, the dynamically induced pressure gradient force due to the shear of the wind maximum along the rainband axis and the updraft core accelerates the air and finally, the air obtains negative buoyancy via evaporation of rain into the downdraft air. This downward motion due to pressure forces and evaporative cooling creates a sharp reflectivity gradient along the inner boundary of the rainbands. The inner-edge downdraft also builds a convective-scale tangential wind maximum just inward of the principal rainband via a low-level divergence of vorticity. This wind maximum is advected inward and contributes to the growing and sustaining of the principal rainband in the hurricane system. The other one is low-level downdrafts (LLDs) which are driven by evaporation and precipitation drag originated at 2 ~ 4 km altitude in the rain cores of each convective element [*Barnes et al*., 1983]. Two downdrafts are spatially distinguished and linked with the updrafts within the rainband and influences the hurricane dynamics by maintaining or weakening the rainband [*Didlake and Houze*, 2009].

In both polluted and AR, there are active spiral rainbands outside the eyewall in the simulated hurricane while the clean case has a distinct concentric clouds in the eyewall (Figure 3.21). However after weakening of the hurricane intensity at landing time, the clean case also shows a lot of spiral rainbands (Figure 3.21a). Downdrafts associated with these spiral rainbands and stratiform regions account for a low θ_e in the boundary layer (Figure 3.22). The dry and cold air with a low θ_e is transported into the

(a) Clean

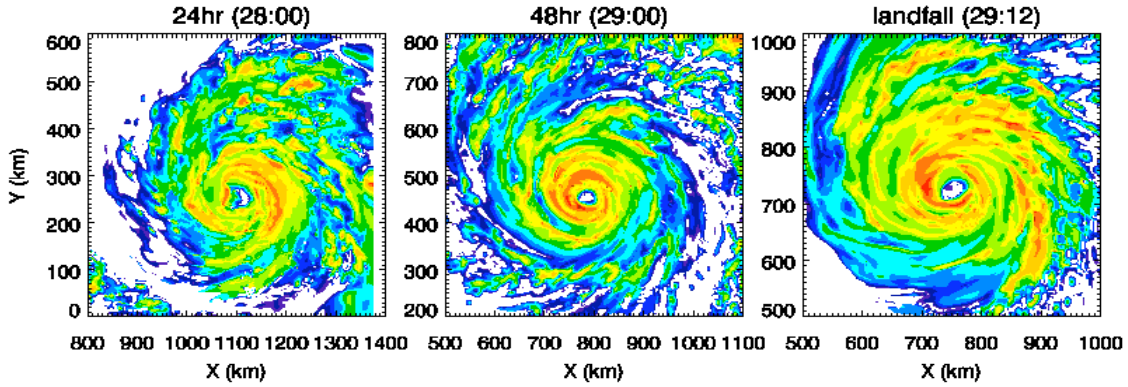

(b) Polluted

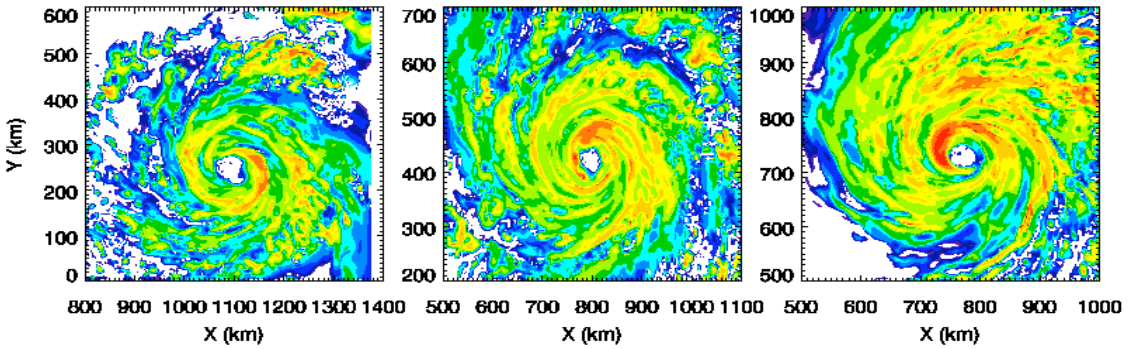

(c) AR

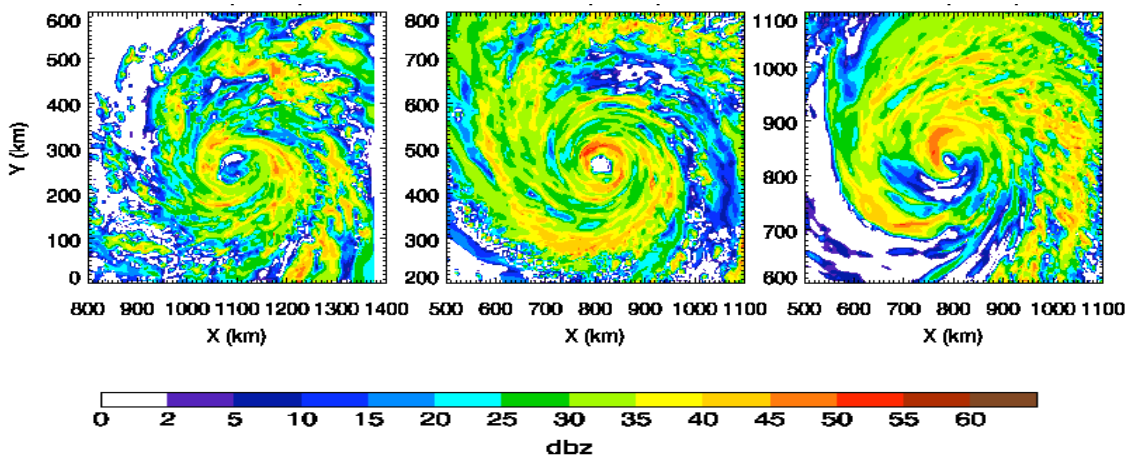

Figure 3.21. Horizontal distribution of radar reflectivity at 2 km altitude in three simulations of (a) the clean, (b) polluted, and (c) AR.

(a) Clean

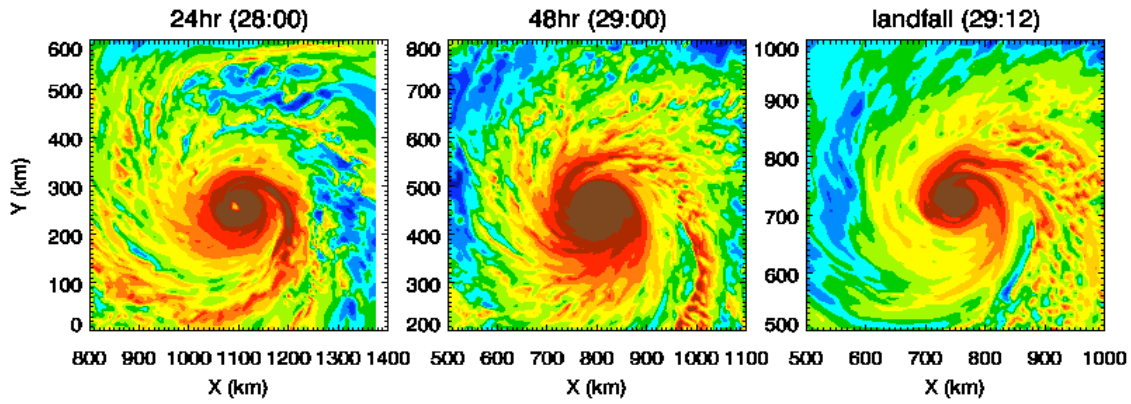

(b) Polluted

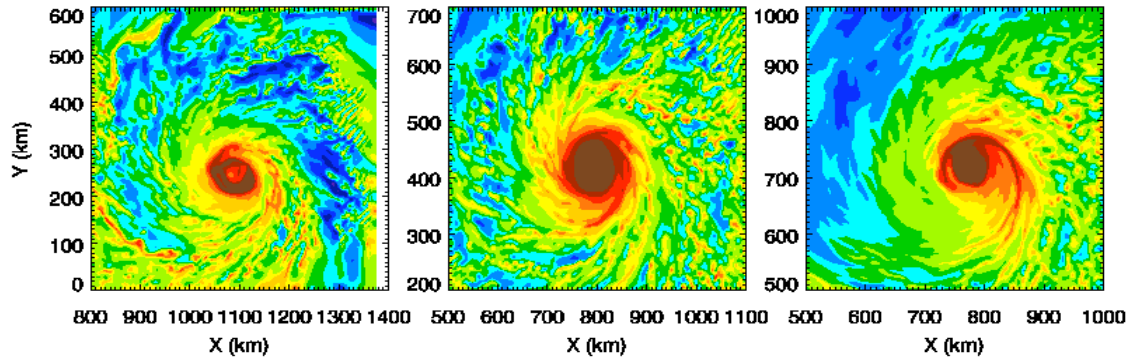

(c) AR

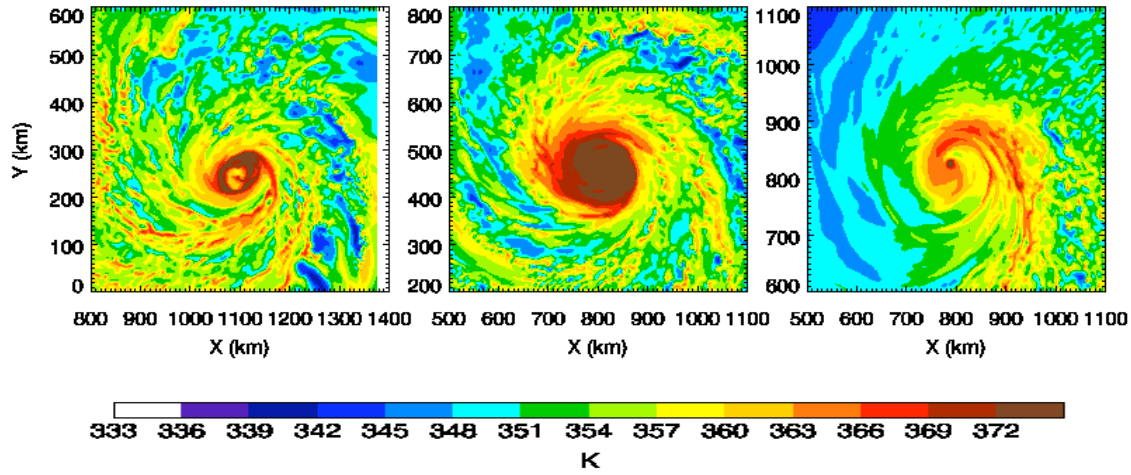

Figure 3.22. Same as in Figure 3.21 but for equivalent potential temperature at the lowest model level.

boundary layer in the rainband regions by downdrafts and advected toward the eyewall region by the low level inflow and leads the suppressing the eyewall convection, and thus weakening of the hurricane intensity in the polluted and AR cases (Figure 3.22b and Figure 3.22c). After 48 h of the strong hurricane stage, however, higher θ_e in the AR case than one in polluted case is shown in the eyewall, which means relatively less cold and moist air with high θ_e is advected into the eyewall region. This higher θ_e in the center of the hurricane is explained by the increase of θ_e in the middle troposphere in the AR case (Figure 3.14c and Figure 3.15c). The tropical cyclone in the clean case has comparatively less activity of rainbands (Figure 3.21a) and thus shows a stronger cyclone than those in two polluted air cases.

To demonstrate the role of rainband and its related convective activity in weakening the simulated hurricane intensity, Figures 3.23, 3.24, and 3.25 illustrate the percentages of area coverage of (a) radar reflectivity grater than 30 dBZ and (b) θ_e less than 365 K of three simulated tropical cyclones as a function of time and radius at the lowest model level. In the tropical cyclone of the clean case, rainfall starts at the beginning of simulation and the convective clouds in eyewall are located within 100 km radius before landing on 12 UTC 29th. After about 6 h, 16 h, and 38 h of simulation, the outward extensions of precipitation appear in the rainband regions of 100 ~ 200 km radius (Figure 3.23a) and their correspondent low θ_e are also propagated outward from 100 up to a radius of about 200 km (Figure 3.23b). The outward extensions of rainbands and large area with low θ_e also present the accompanying of strong downdrafts concerned with the rainbands. The polluted case shows larger area coverage of rainfall

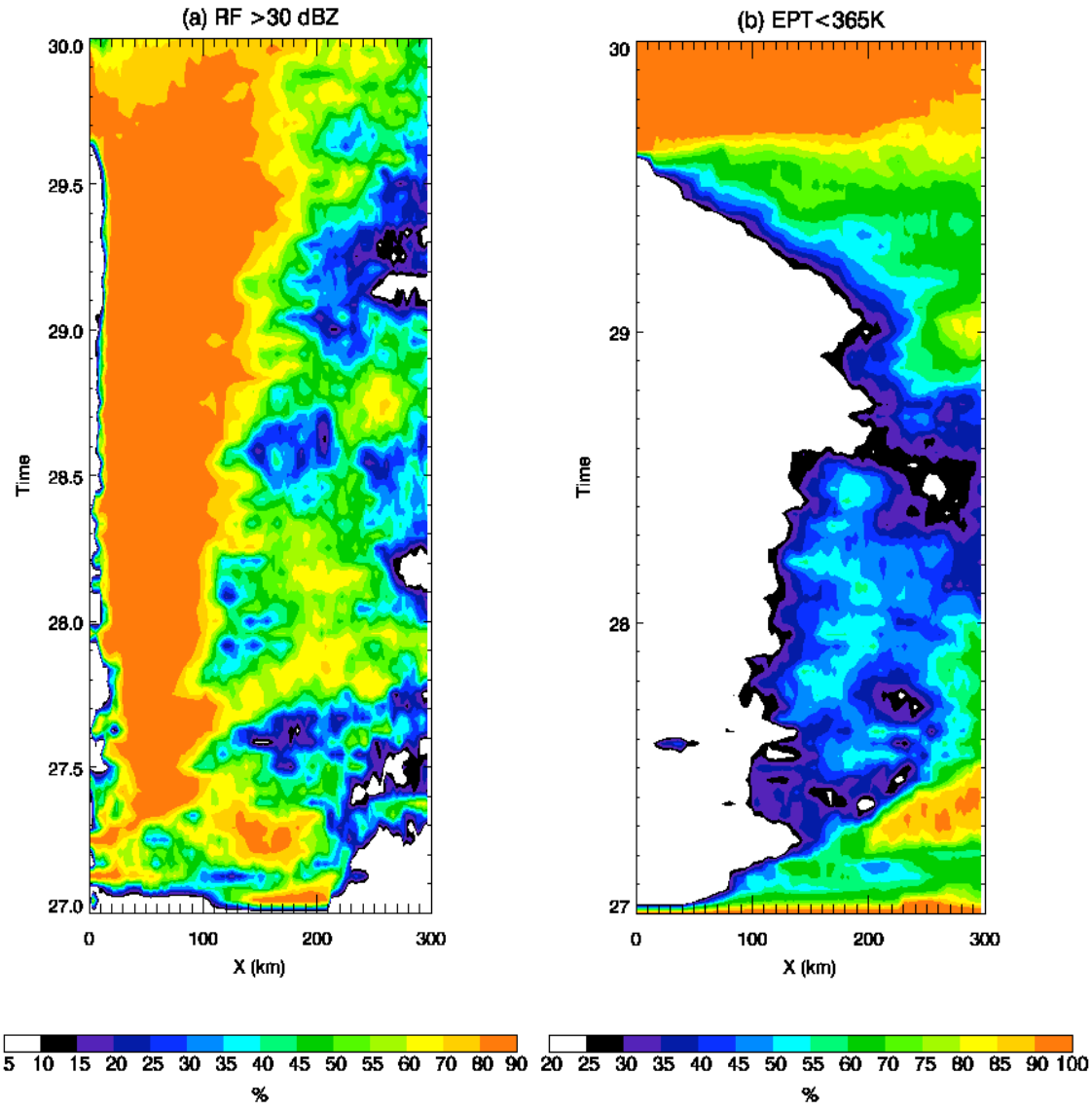

Figure 3.23. (a) Time-radial cross section of the percentage areal coverage of radar reflectivity greater than 30 dBZ and (b) time-radial cross section of the percentage areal coverage of equivalent potential temperature less than 365 K in the clean case.

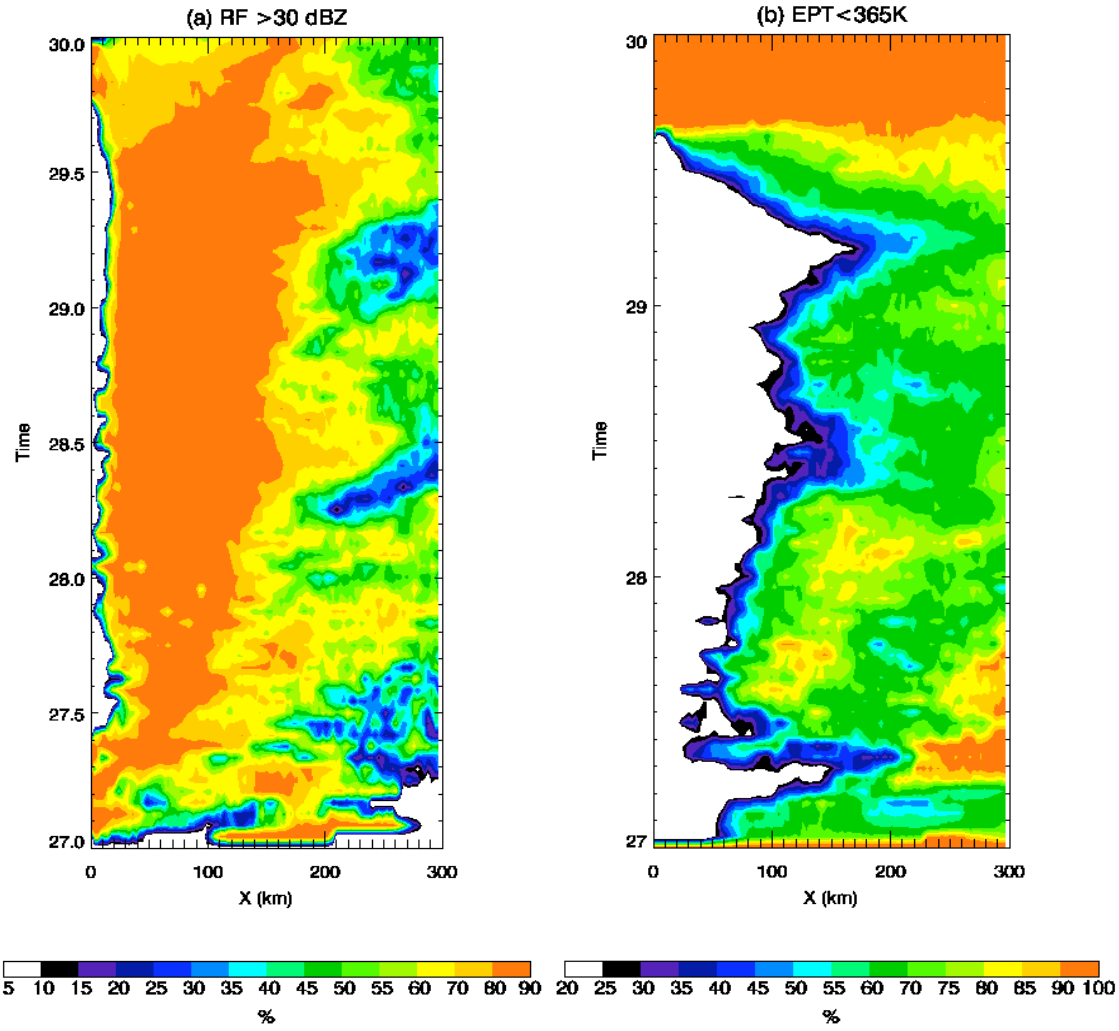

Figure 3.24. Same as in Figure 3.23 but for the polluted case.

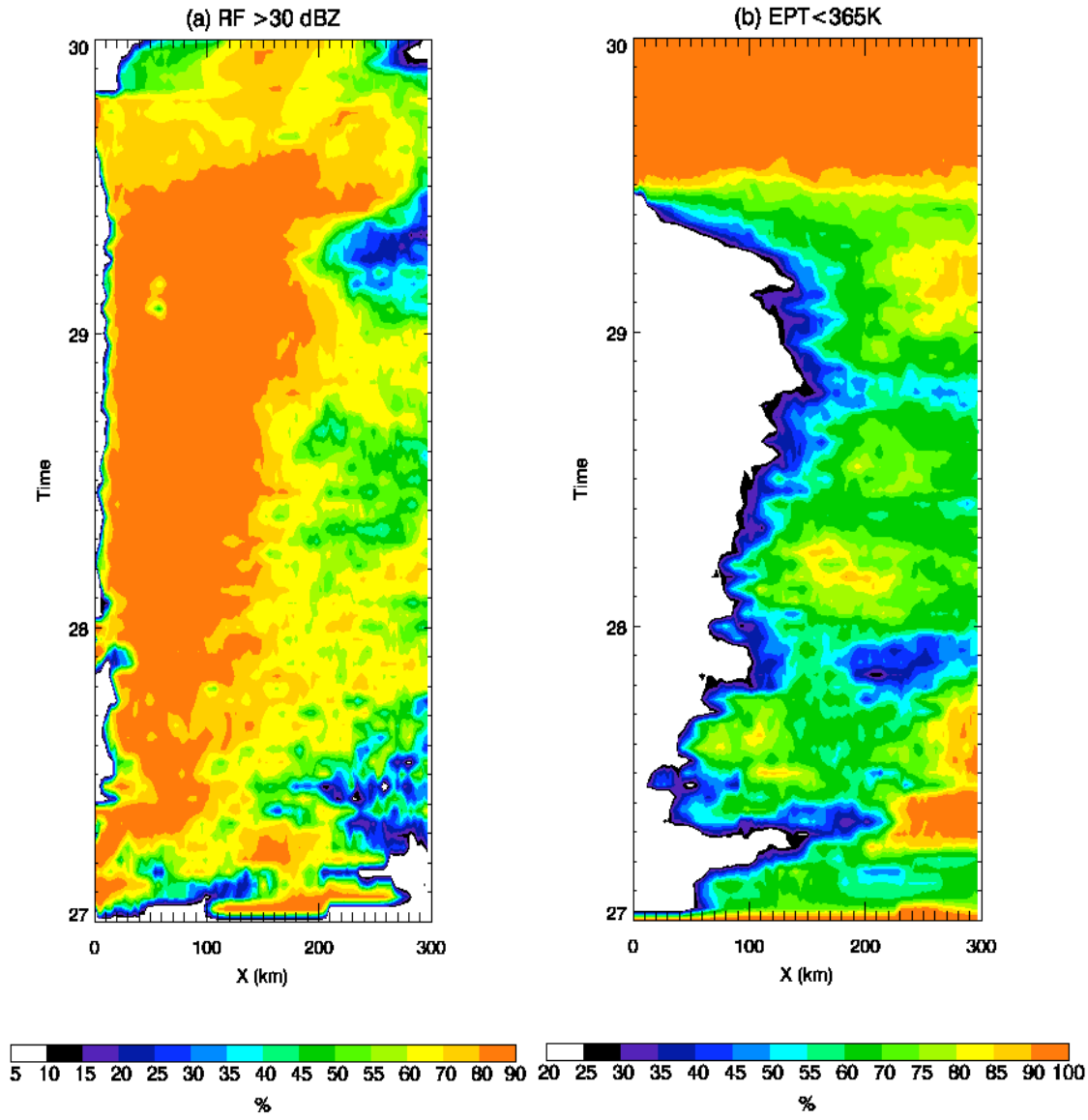

Figure 3.25. Same as in Figure 3.23 but for the AR case.

than that in the clean case with wider radius of convective clouds in the eyewall up to 150 km before landing (Figure 3.24a). The high area coverage with low θ_e also propagates outward from 60 km to 300 km and indicates more active rainbands and its related downdrafts in the polluted case (Figure 3.24b). Before tropical cyclone landing, there are three dominant extensions after about 4 h, 14 h, and 32 h of simulation into a radius of 250 km and the areas with low θ_e show the extended patterns toward outside of the eyewall at similar time periods. The percentage areal coverage of high radar reflectivity and low θ_e in the AR case are shown in Figure 3.25a and Figure 3.25b, respectively. They are comparable to those in the polluted case, but the area of radar reflectivity in the AR case appears larger spatial coverage than the polluted case even its less intensity in rainband regions (Figure 3.25a). This more larger areal percentage of rainfall regions with a slightly less coverage of low θ_e in the AR case suggest that there are more precipitation, but the air with relatively higher θ_e in the middle troposphere is advected into the boundary layer by downdrafts in rainband regions.

To illustrate variations of dynamic fields during an evolution of tropical cyclone, time-radial Hövmoller diagrams of the azimuthally averaged vertical velocity in 500 hPa (shading) and tangential velocity in 700 hPa (contour) are shown in Figure 3.26 for three simulated hurricane systems. The simulated life cycles of the activity of vertical velocity correspond well to the hurricane intensity evolution in Figure 3.1 and the maximum velocity area of tangential wind is propagated toward the rainband regions. Three simulated tropical cyclones exhibit the strong convective updraft at the eyewall and relatively less convective updraft at the periphery with their accompanying tangential

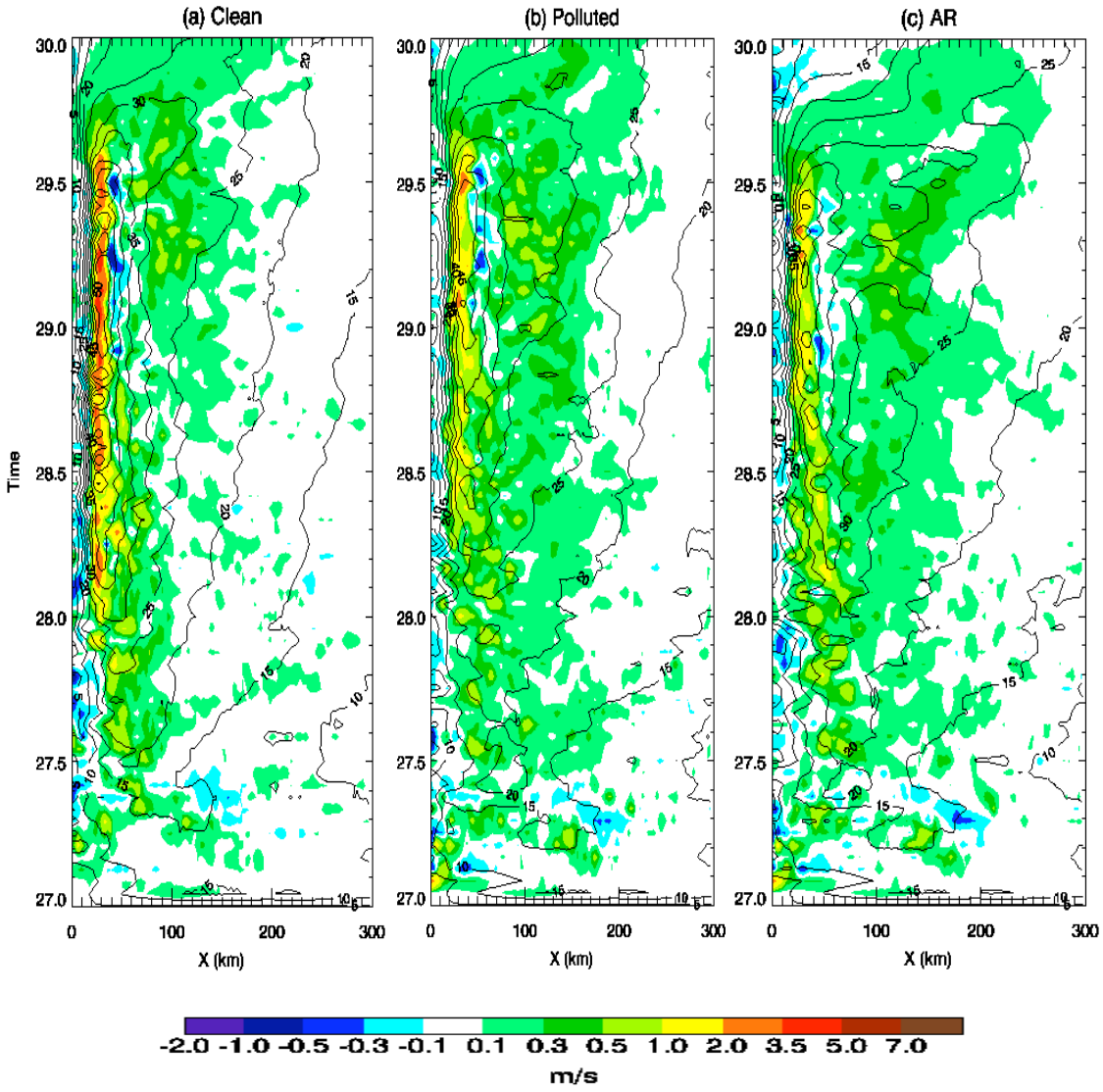

Figure 3.26. Time-radial Hovmoller diagrams of the azimuthally averaged vertical velocity in 500 hPa (shading, m/s) and tangential velocity in 700 hPa (contour, m/s). (a) , (b), and (c) indicate the clean, polluted, and AR case, respectively.

winds. With time, the eyewall updraft becomes weaker, while the updraft at the outer periphery becomes broader and to be developed. At the same time, the low level tangential wind exceeding 25 ms^{-1} expands from 90 km to 200 km. The clean case shows the concentric eyewall structure with the strongest updrafts in the eyewall and downdrafts in center of tropical cyclone after 24 h simulation (Figure 3.26a). New convections outside the eyewall begin to be developed around 06 UTC 28th in the vicinity of 100 km radius when the convective updraft of the hurricane center starts to be weakened. Another updraft exists at the radius of 90 km on 14 UTC 28th and the low level tangential wind is also getting stronger with corresponding maximum updrafts before landing. The increases of the middle level vertical velocity and a low level tangential wind velocity in outside the eyewall are closely related with each other [*Hence and Houze*, 2008; *Didlake and Houze*, 2009]. The polluted case shows a delayed intensification with less intensity of updrafts and downdrafts in the eyewall and center comparing with the clean case (Figure 3.26b). In rainband regions, on the other hand, it shows slightly earlier and stronger development of convective updrafts after 6 h simulation than those in the clean case. The regions of updrafts extends outward up to 200 km radius and strong updrafts (> 0.3 ms^{-1}) which starts at 12 UTC 28th are maintained for about 24 h at the radial distance of 100 ~ 150 km. Its corresponding tangential wind is also following the trend of vertical velocity and represents high wind velocity with strong updrafts in rainband regions. The AR case shows the weakest updraft and downdraft intensity in the eyewall and center of the hurricane with its fast dissipation due to early landing (Figure 3.26c). In outside the eyewall of the AR case,

the updrafts velocity is less strong than that in the polluted case but the area with weak updrafts (> 0.1 ms^{-1}) is distributed up to 200 km radius. The low level tangential wind also shows similar pattern and much wider region with moderate intensity of 20 ms^{-1}. The reduced intensity of vertical motion in the AR case also indicates the suppressing of convection by the aerosol radiation effects.

The general characteristics and impacts of the rainband in a tropical cyclone are important in decaying or maintaining of the hurricane system [*Barnes et al*., 1983; *Powell*, 1990a, b; *Wang*, 2002; *Hence and Houze*, 2008; *Didlake and Houze*, 2009]. The rainband of tropical cyclone is a mixture of convective and stratiform precipitation regions and characterized by their intensity of vertical motion and rainfall amounts. Usually convective precipitation regions have active updrafts and a large amount of rainfall and can be distinguished by locally and vertically oriented cells of high reflectivity in radar reflectivity data. The stratiform cloud area is formed by ice particles transported into outside of the eyewall by strong updrafts in the eyewall and consists of weak vertical motions and less amounts of rainfall than those in convective regions. In radar reflectivity, it appears a stratiform structure in the horizontal dimension and is often signaled by a bright band due to a melting of precipitating ice particles [*Houze*, 1993, chapter 6].

To separate the convective and stratiform precipitation in three simulated hurricane rainbands, the convective/stratiform separation algorithm is applied [*Didlake and Houze*, 2009]. Figure 3.27 presents the results of the convective and stratiform precipitation separation applied to the radar reflectivity data at 2 km altitude in Figure

(a) Clean

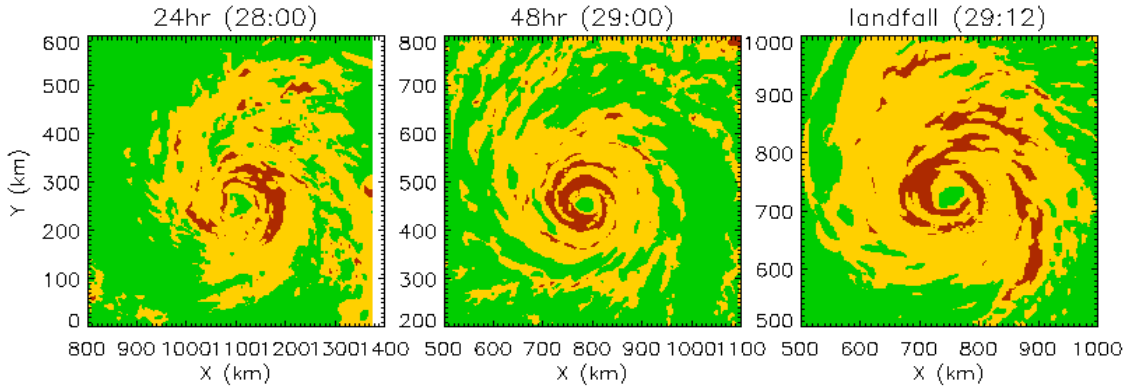

(b) Polluted

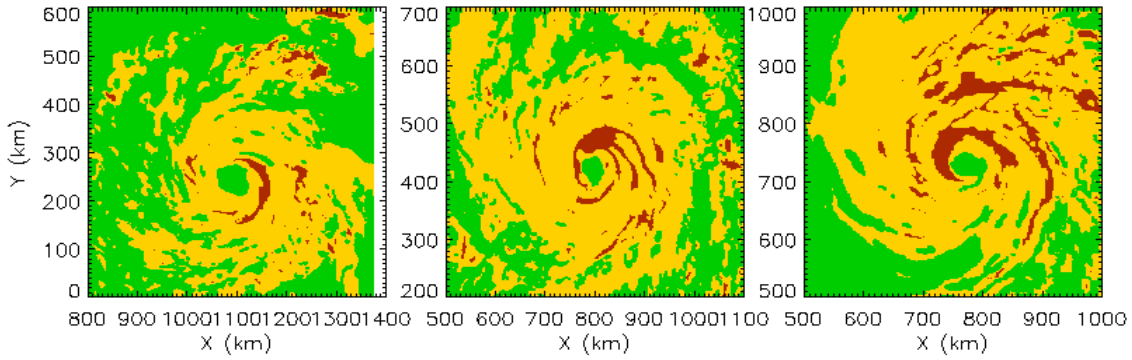

(c) AR

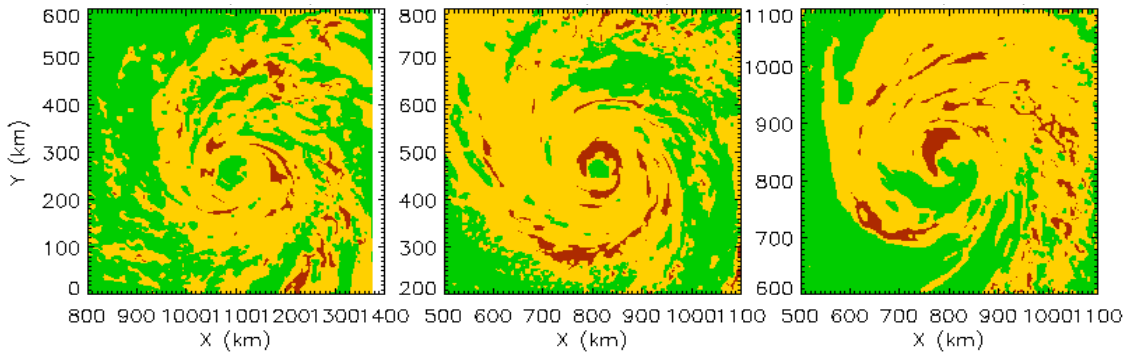

Figure 3.27. The results of convective stratiform separation algorithm applied to simulated radar reflectivity data shown in Figure 3.21. Dark red area indicates convective region (≥40 dBZ), yellow area means stratiform region, and green area means weak-echo region.

3.21. The thick and circular line of convective precipitation (dark red) around the eyewall is well defined in the clean case after 48 h simulation. Before landing (60 h), more convective bands appear along spiral rainbands and stratiform precipitation regions (yellow) are dominant rainfall pattern outside the eyewall. The clean case has the concentric eyewall with its strongest intensity of the hurricane system. The polluted and AR cases present more wide range of stratiform and noticeable convective rainfalls outside the eyewall after 48 h, while their thin and less strong intensity of convective rainbands are exhibited in the eyewall area (Figure 3.27b and Figure 3.27c). More convective and stratiform precipitation regions at the periphery of the hurricane in two polluted air cases represent the typical characteristics of weakening of tropical cyclone. In comparing with rainbands of the polluted and AR case, the AR case with the aerosol radiation effects shows the symmetric convective region in the eyewall and well-developed convective rainfall line along rainbands at the periphery of the hurricane after 48 h simulation even its weak hurricane intensity. It is explained by an air with high θ_e introduced into the eyewall and boundary layer outside the eyewall, thus leading more convection (Figure 3.22c). However, convective and stratiform rainfalls are getting weaker in both the eyewall and rainband regions and show the weakest intensity after landing in the clean and two polluted cases (Figure 3.27c). After landing, the symmetric convective eyewall is still noticeable in the polluted case, while the asymmetric structure in the AR case is shown in the eyewall.

The vertical velocity at 4 km altitudes in Figure 3.28 (shading) consists of updrafts and downdrafts in three simulated tropical cyclones and corresponds to the

(a) Clean

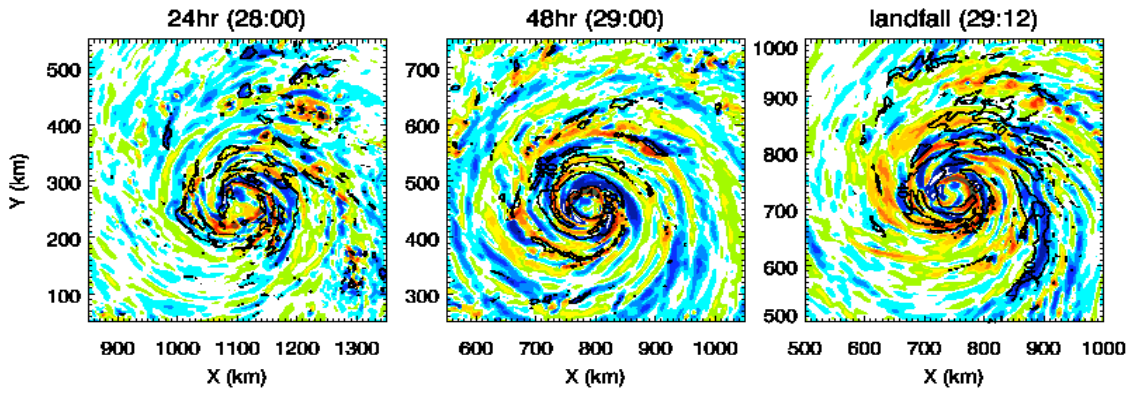

(b) Polluted

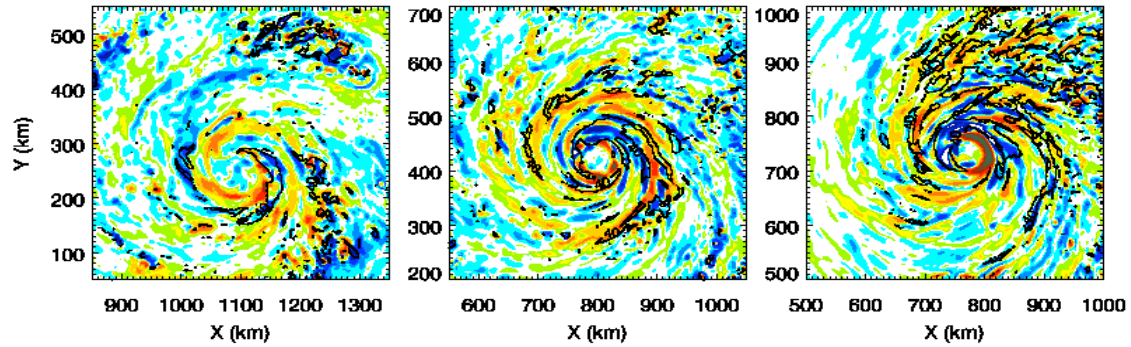

(c) AR

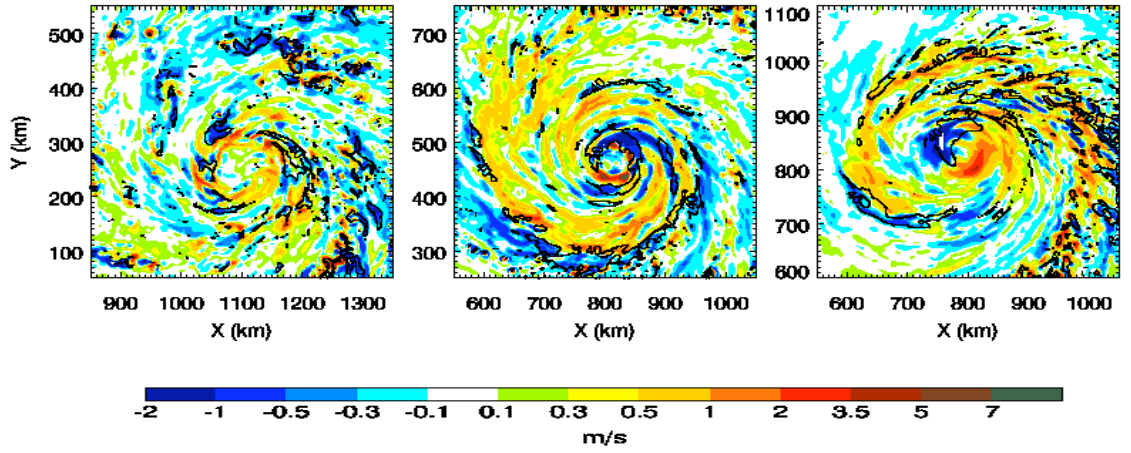

Figure 3.28. Horizontal distribution of radar reflectivity greater than 40 dBZ (contour) at 2km and vertical velocity (shading) at 4 km.

spatial distributions of higher θ_e and lower θ_e, respectively (Figure 3.22). The convective rainbands (contour) also occur in the area of intermittent pattern of updrafts and downdrafts cores and the convective activity in outside the eyewall is provided by the simulated hurricanes of the polluted and AR cases with their dominant rainband precipitation (Figure 3.28b and Figure 3.28c). The downdraft cores with negative values are mainly associated with inner-edge downdrafts (IEDs) rather than the low level downdrafts (LLDs) because the typical height of occurrence of LLD is lower than 4 km levels. Some convective regions overlapped in Figure 3.28 are matched with the locations of downdrafts core, in particular, IEDs. The polluted case presents more intense updrafts and downdrafts motions in outside the eyewall with active convective regions (Figure 3.28b), while the AR case shows broad updrafts regions around the eyewall and far-away downdrafts cores from the eyewall with a less convective rainfall inside of this downdrafts (Figure 3.28c). The intensity of downdrafts in the AR case is comparable with and their cores are distributed over broader area than those in the polluted case. The updrafts in the AR case show slightly weak intensity but more wide area coverage in the periphery of the hurricane than those in the polluted case. The relatively small scales with high intensity of updrafts and downdrafts, i.e. IEDs in the polluted case represent their convective-scale phenomena, which means updrafts and IEDs are associated spatially with the dynamics of convective cells [*Didlake and Houze*, 2009].

For the connection between the middle level and low level IED speeds, Figure 3.29a and Figure 3.29b present the probability distribution of 1 km level maximum IED

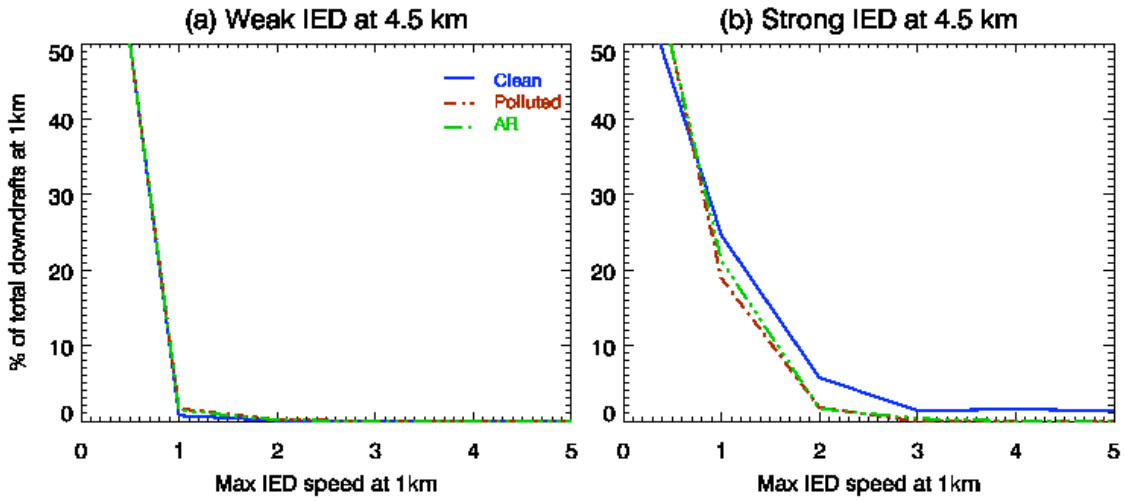

Figure 3.29. The relationship of the downdraft speeds at 1 km altitude between 10 km to 300 km from the center of the hurricane that occur when the maximum downdrafts speed at 4.5 km altitude in the same domain is 3 $\leq$ m/s in the same cross section. Only the maximum downdrafts speed at 1km in an individual cross section is counted in the frequency. The 1 km maximum downdraft counts are normalized by the total number of cross sections in which the 4.5 km downdrafts condition is matching and a 1 km downdraft exist. (b) as in (a), but that the 1 km maximum downdrafts are calculated for when the 4.5 km maximum downdraft is > 3 m/s [*Didlake and Houze*, 2009].

speeds when the 4.5 km levels IED obtains a certain maximum speed up to 5 ms^{-1} [*Didlake and Houze*, 2009]. When the maximum speed of IED at 4.5 km is less than 3 ms^{-1}, most of the maximum 1 km IEDs have less than 1 ms^{-1} speeds (Figure 3.29a). On the other hand, when the 4.5 km levels IED reaches over 3 ms^{-1} speeds, a large portion, 35 % of the 1 km IEDs shows speeds more than 1 ms^{-1} in the clean cases, which means a strong intensity of downdrafts in the eyewall and at the periphery of the hurricane even it has a weak activity of convection in outside the eyewall. The polluted and AR cases have the reduced portions of 21 % and 23 % of the 1 km IEDs greater than 1 ms^{-1} and represent the less intensity of downdraft than that in the clean case even their active convections in rainband regions. Generally, a weak middle level IED goes with a weak low level IED less than 1 ms^{-1} and a comparatively strong middle level IED is mainly accompanied by a higher probability of significant low level IEDs. Two polluted air cases exhibit the reduced occupation of strong low level IEDs with their strong middle level IEDs which represents a weakening of the hurricane intensity. The AR case shows a higher portion of strong 1 km IEDs and it is likely to be linked with an accompanied increase of low level wind in the AR case (Figure 3.26c).

Figure 3.30 illustrates vertical profiles of the horizontally averaged vertical velocities over inner domain within the convective cores. The convective cores are defined as the grid points where the averaged vertical velocity between 5700 m and 14700 m altitudes is greater than or equals to 1 ms^{-1} in this figure [*Van den heever et al*., 2006]. During the initial stage of three simulated hurricane systems (24 h and 48 h), the updrafts in clean case are greater than those in the polluted and AR cases throughout

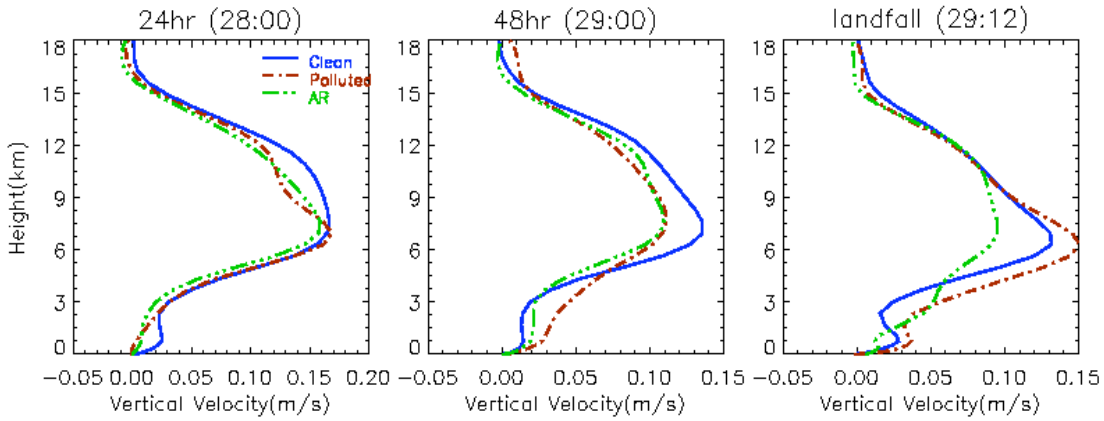

Figure 3.30. Vertical profile of the difference of the three experiments for the horizontally averaged vertical velocity within the convective cores (defined as the grid points where the vertical velocity averaged between 5700 and 14700 m is greater than or equal to 1 m/s [*Van den heever et al*., 2006] after 24 h (28:00), 48 h (29:00), and landing (29:12) (day in August 2005: hour UTC).

most of the troposphere. It represents the early development of the hurricane convection in the clean case. During the developing stage of the simulated hurricanes, the convective cores in the polluted case and AR case have the impact on the increase of updraft strength between 0 km and 5 km heights, while the impacts of high aerosol concentrations on updraft strength are reduced in the middle troposphere between 5 km to 13 km altitude. Beside the strong convection in the eyewall, the increase of the low level updraft velocity means the enhanced shallow convections concerned with precipitation in rainband regions. Before hurricane landing (60 h), the altitude with maximum velocity is getting lower and the reduced vertical velocity in the AR case is noticeable due to its fast dissipation. As the results of previous studies, the convection in the AR case is weakening and it is associated with the suppressing of convections triggered by the aerosol radiative effects. The differences in a vertical velocity and cloud hydrometeors due to modifications in aerosol concentrations and aerosol radiative properties can lead a microphysical and dynamical feedback. The production of ice, snow, and graupel above the freezing level can be triggered by strong updrafts and this production in turn enhances the updraft strengths by more latent heat release. On the contrary, the weak updrafts are mostly contributed to the production of liquid cloud water rather than the ice water paths. Examining a time series of the contributions of cloud water to the total liquid water mass (cloud and rain water) describes that the cloud water fraction in three simulated hurricanes are greatest during the initial stage of hurricane system and decrease after 24 h simulations (Figure 3.31a). The clean case demonstrates a large rain contribution, which means a more efficient warm rain process

(a)

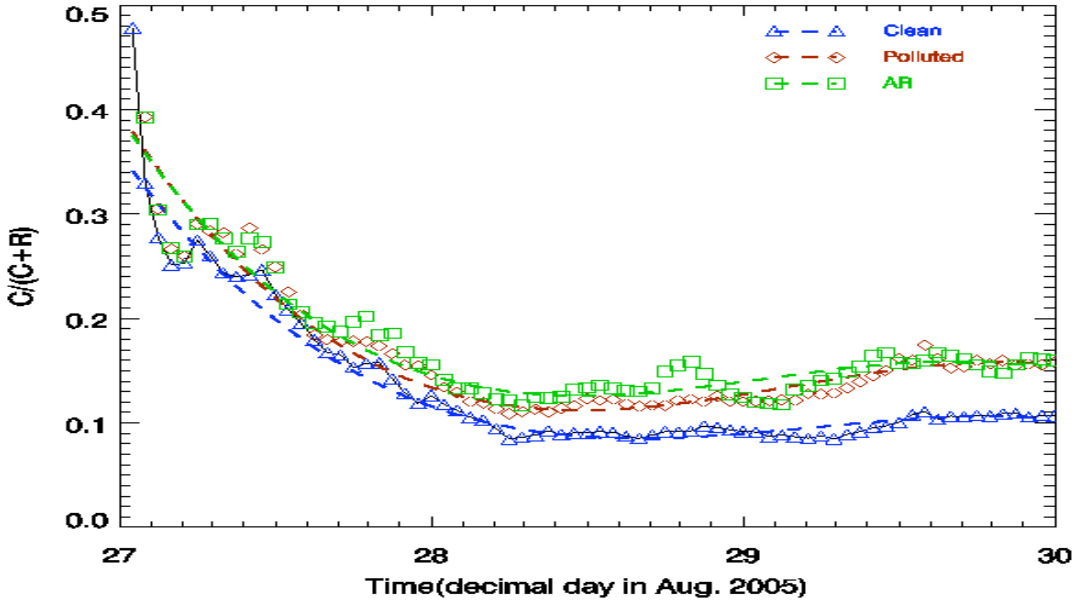

(b)

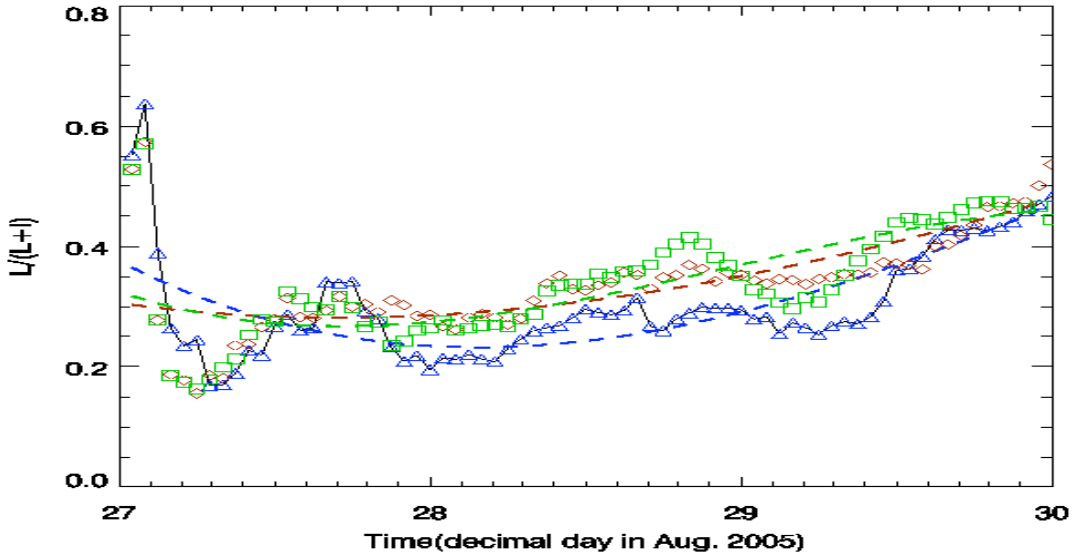

Figure 3.31. Scatterplot of the ratio of (a) vertically integrated cloud water/vertically integrated (cloud water + rain) mixing ratios and (b) vertically integrated liquid/vertically integrated (liquid + ice) mixing ratios, as a function of time for three experiments within the updrafts. Lines represent the best third-order polynomial fit [R2 values range (a) 0.93, 0.90, and 0.88, and (b) 0.52, 0.50, and 0.53] [*Van den heever et al.*, 2006].

in the clean case. The polluted and AR cases present a high portion of cloud water throughout the whole simulation periods and they describe that enhanced aerosol number concentrations impact on converting cloud water to rain by acting as CCN in relatively weak updraft regions. The increase of CCN can lead a considerable reduction in the cloud droplet size and inhibits the conversion of cloud water to rain. Also the aerosol radiative effect plays a role in transforming cloud water into the rain water during the stage of the hurricane development (28th ~ 29th). A time series of the contributions of liquid water to the total condensate, including ice water paths is shown in Figure 3.31b. The clean case mostly has the greatest ice water contributions and two polluted air cases have a larger portion of liquid water contributions. Two polluted air can produce more liquid water due to high concentration of aerosols in the troposphere, but the weak intensity of updrafts is not favorable to transfer more liquid water to the freezing level to make ice formation. Although their difference is not dominant, the AR case shows the highest liquid water contribution after about 36 h, supporting the fact that the aerosol radiative effect has the weakest updrafts intensity due to its suppressing convection. For the impacts on dynamic feedback, the track of simulated tropical cyclone can be changed. In Figure 3.32, the simulated tracks for the clean (blue), polluted (dark red), and AR (green) cases are illustrated with the observed one (black) during the whole simulation time. The polluted air hurricanes with a reduced intensity tend to move more eastward and it is related with a weak intensity of the hurricane and the beta effect. Being the weakest hurricane, the tropical cyclone in the AR case run shifted eastwards from that in the clean case and in addition, it is easily influenced by the most developed

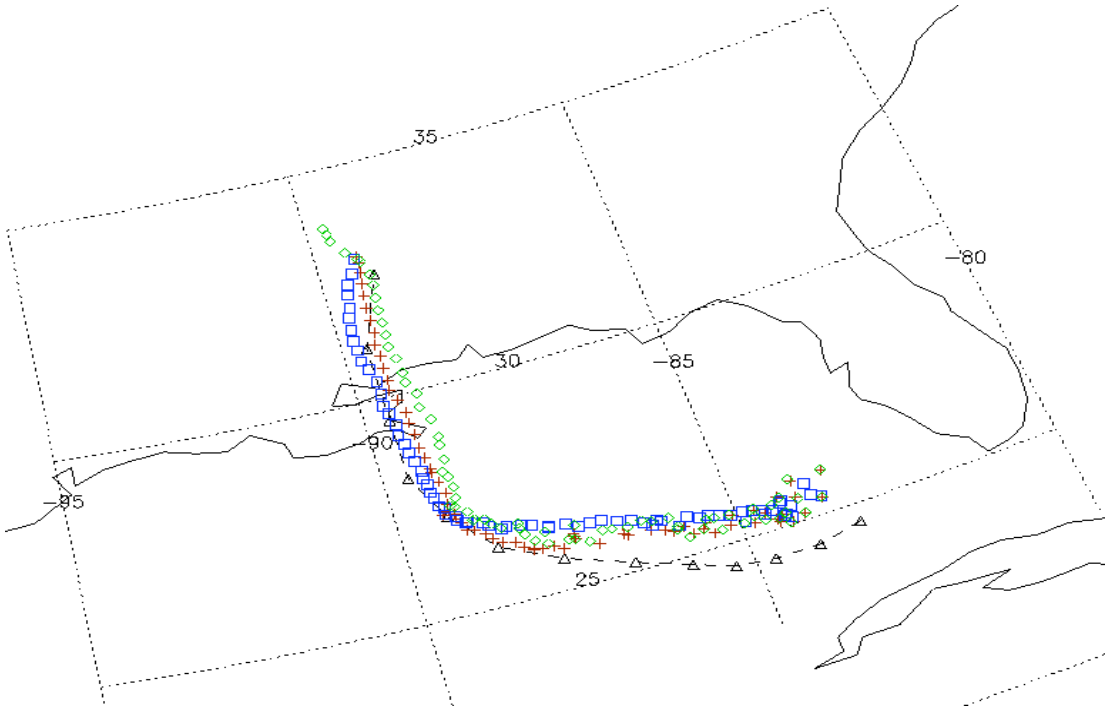

Figure 3.32. Time tracks of the observed (black) and simulated hurricanes for the clean (blue), polluted (dark red), and AR (green) cases.

convections at periphery and on land. Figure 3.33 represents the geopotential height fields of the clean, polluted, and AR cases at landfall. The clean and polluted cases show the distinct eyewall patterns before landing. However, the eyewall in the AR case is almost disappeared and the strong convective systems over the land are noticeable. The hurricane of the AR case shows the weakest intensity and early landing and this may be related with the effects of and interaction with the convective systems over land.

These simulation results demonstrate that the effects of high aerosol concentrations and radiative properties are dominant in their thermodynamic and dynamic fields during the hurricane evolution.

3.6 THE EVALUATION OF AEROSOL DIRECT AND INDIRECT EFFECTS ON TROPICAL CYCLONE

To assess the simulated hurricanes by aerosol direct and indirect effects, the results of minimum pressure and maximum wind speeds at surface in twenty- ensemble experiments are shown in Figure 3.34 and Figure 3.35, respectively. We run twenty members for the same Katrina case, altering the initial and boundary aerosol number concentration at surface from 100 to 2000 # cm^{-3} for aerosol indirect effect (Figure 3.34). More polluted cases show the increased surface pressures (Figure 3.34a) and less intensity of wind speeds (Figure 3.34b) at surface, which means the weakening of the hurricane intensity when the air becomes dirty and dusty. Also, we have the twenty-member simulations with the same aerosol number concentrations as those in Figure

(a) Clean (b) Polluted (c) AR

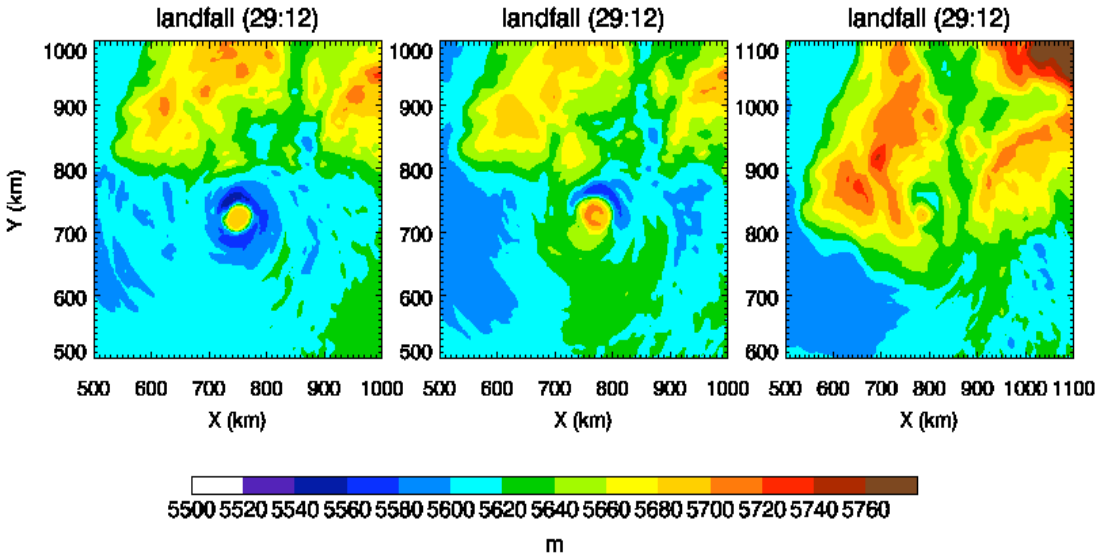

Figure 3.33. Horizontal distribution of geopotential height at 500 hPa at landfall. (a) the clean, (b) polluted, and (c) AR, respectively.

3.34 except for the including of the modified Goddard shortwave radiation scheme for the aerosol direct effects (Figure 3.35). The aerosol direct effects cases represent a similar pattern as those in the aerosol indirect effect cases, but more polluted cases illustrate a delayed weakening of the hurricane. It is likely to be the uncertainties of the hurricane system after landing. Based on the results of ensemble model experiments, it is found that the development and intensity of the simulated tropical cyclone are quite sensitive to the cloud microphysical variations by high aerosol concentrations and the aerosol radiation effects.

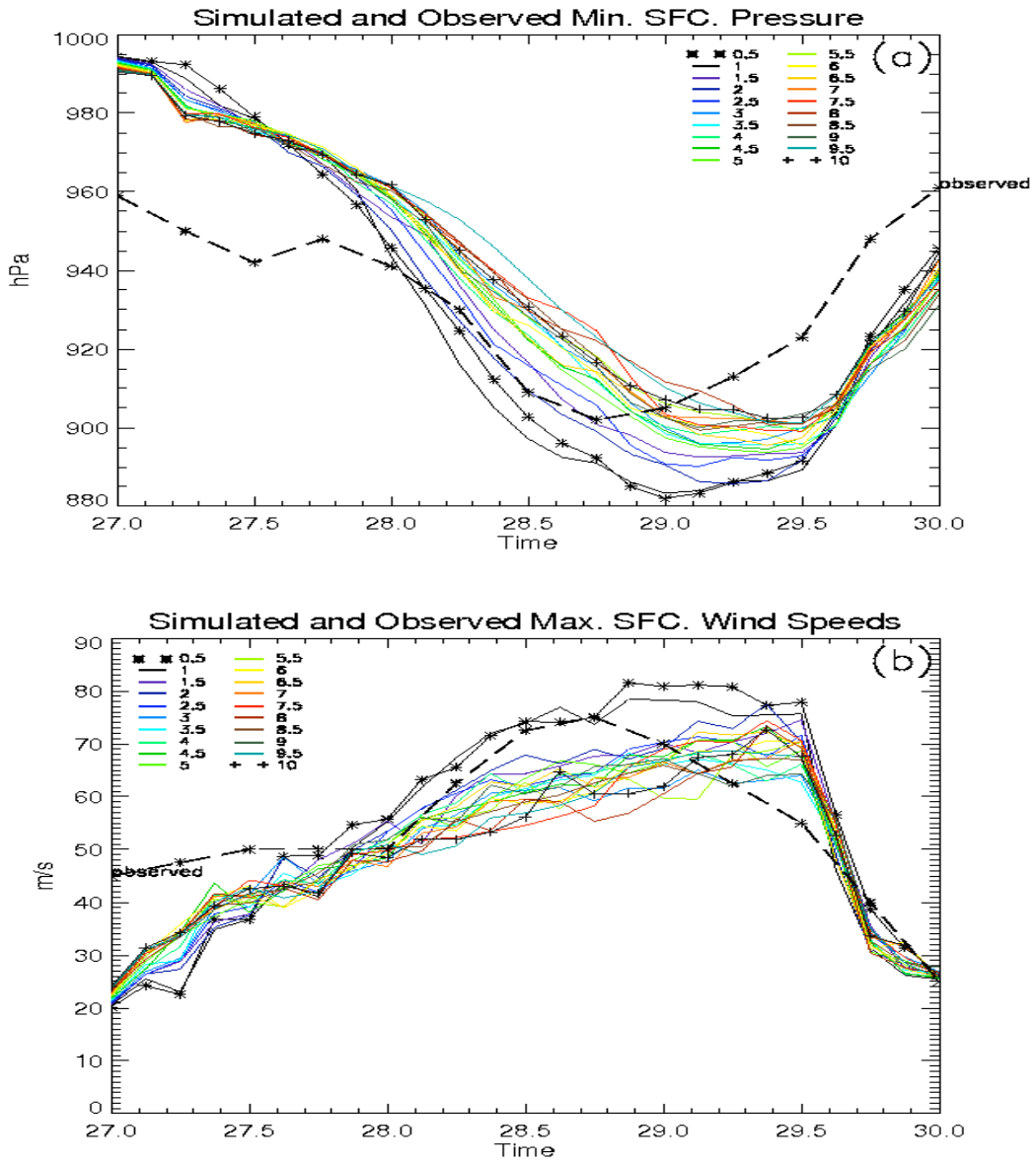

Figure 3.34. Time evolution of (a) minimum surface pressure and (b) maximum wind speed at the lowest model level for the hurricanes of 20 ensemble simulations. The black line is the observed values of the hurricane Katrina.

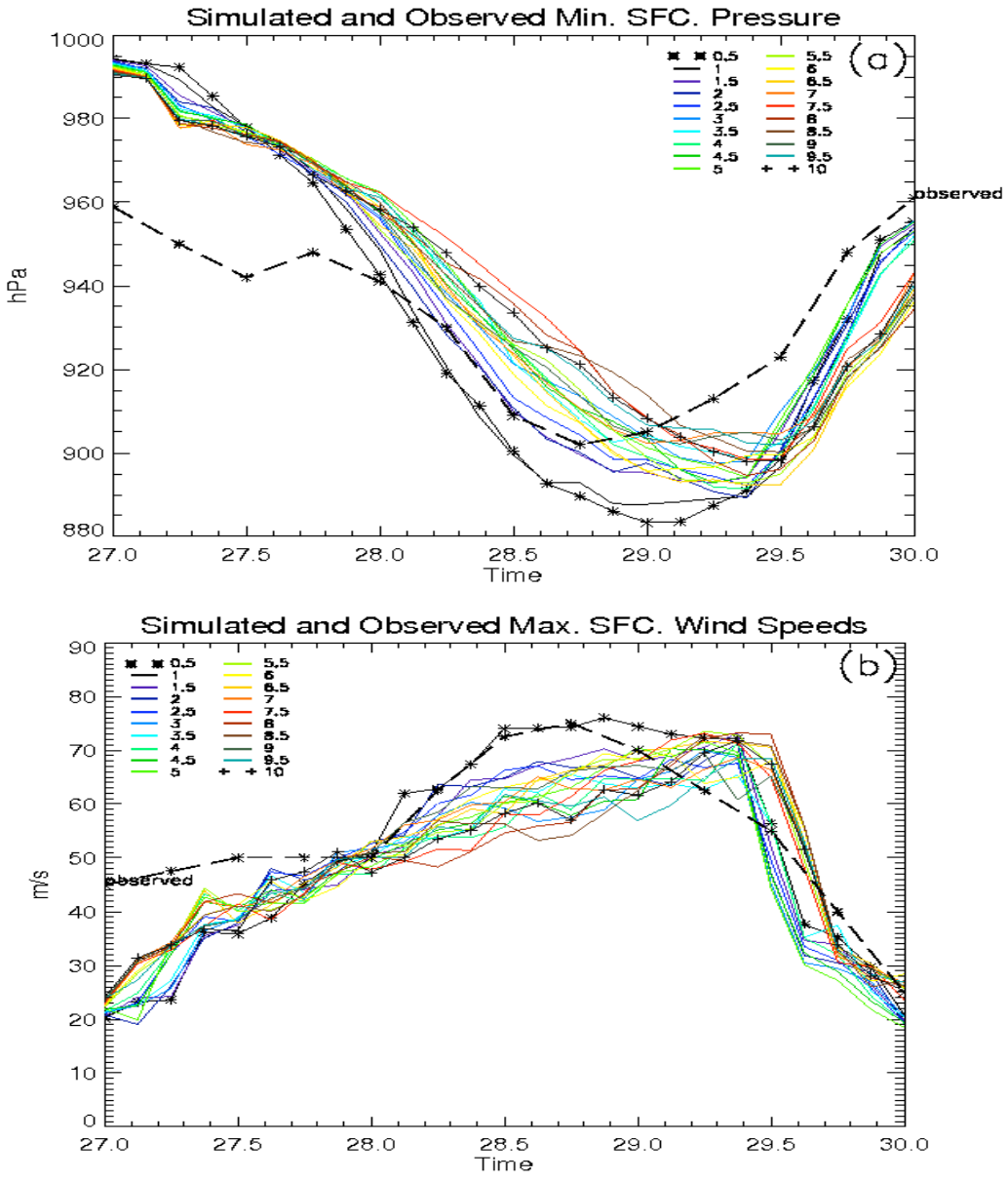

Figure 3.35. Same as in Figure 3.34 but for the aerosol direct effects simulations.

4. CONCLUSIONS

The direct and indirect effects of aerosols on the hurricane 'Katrina' have been investigated using the WRF model with a two-moment bulk microphysical scheme developed by *Li et al*. [2008] and modified Goddard shortwave radiation scheme by *Fan et al.* [2008]. The microphysical scheme in this study can predict time-dependent mass mixing ratios and number concentrations of cloud water, rain water, ice particle, snow flakes, and graupels, as well as the aerosol mass mixing ratio and number concentration. The modified shortwave radiation scheme calculates the wavelength-dependent aerosol radiative properties such as AOD, SSA, and AF based on the aerosol composition, size distribution, mixing state and ambient relative humidity. Simulations of the hurricane 'Katrina' are conducted under the three aerosol scenarios: 1) the clean case with an aerosol number concentration of 200 cm^{-1}, 2) the polluted case with a number concentration of 1000 cm^{-1}, and 3) the aerosol radiative effects (AR) case with same aerosol concentration as polluted case but with a modified shortwave radiation scheme. The effects of aerosol number concentrations and aerosol radiation properties on the evolution of the hurricane system have also been assessed through ensemble model experiments with twenty aerosol scenarios and applying the modified Goddard shortwave radiation scheme.

The results of model simulations show that the polluted air case with a high aerosol concentration is summarized in the schematic diagrams in Figure 4.1. A high

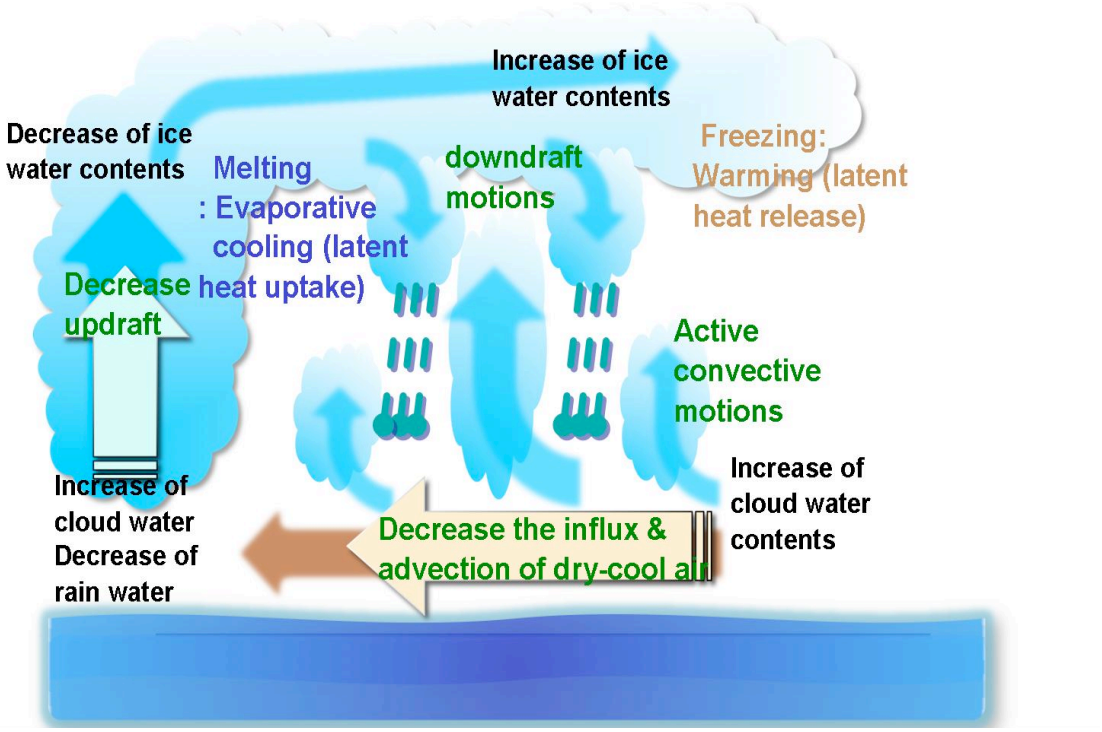

Figure 4.1. The schematic diagram of the hurricane system by the aerosol indirect effects.

aerosol concentration increases the amount of cloud hydrometeors and leads to more active rainbands at the hurricane periphery. As a result, polluted and AR cases indicate the delayed and weakened hurricane intensification because the updrafts in the rainband regions plays a role in hindering the advection of warm and moist air into hurricane center by lifting this air before reaching the hurricane eyewall region. Moreover, the downdrafts just inside and outside the updraft cores can influence the weakening of the hurricane by transferring cold and dry air with low θ_e into the boundary layer. This air can be supplied to the hurricane center by the low level inflow and give a negative effect on the hurricane intensification. Therefore, the aerosol indirect effect can contribute to the weakening of the hurricane intensity, representing a weak convective intensity in the eyewall and more enhanced convective activity outside the eyewall.

The schematic diagram of the hurricane structure in the AR case is shown in Figure 4.2. The AR case simulation shows that its hurricane has the weakest intensity of hurricane center with the fast dissipation of tropical cyclone due to early landing. However, when comparing to the results of the polluted case, the AR case has broader areas of rainbands and stratiform clouds outside the eyewall regions. Because of the warming in the troposphere and cooling at the surface by the aerosol absorption of solar radiation, the updraft intensity in the AR case is relatively lower than that in the polluted case at the periphery of hurricane. However, enhanced amounts of hydrometeors due to warm troposphere and more latent heat releases (more buoyant air) are produced in middle troposphere. The strong downdrafts associated with the rainband core and buoyant air can transport the air with relatively high θ_e into the boundary layer and this

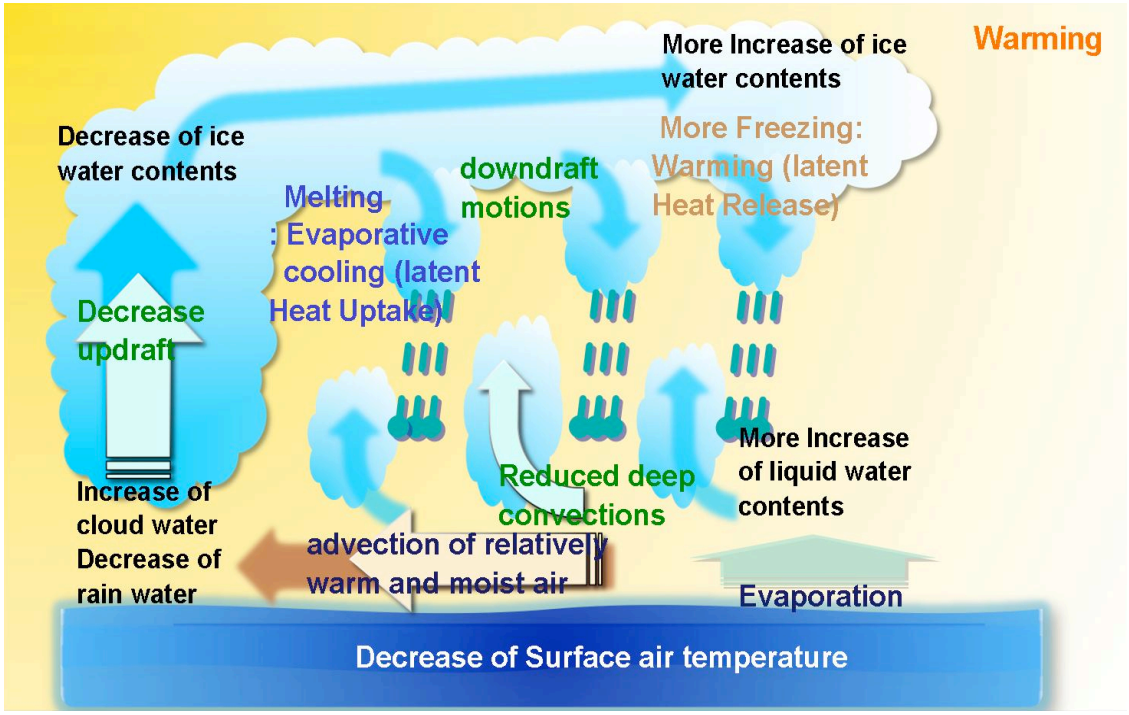

Figure 4.2. The schematic diagram of the hurricane system by the aerosol direct effects.

warm and moist air is advected into the center of hurricane along with the low level influx. The increase of low level winds in the AR case show a wide and outward distribution outside the eyewall and is closely linked with the enhanced intensity of a tangential wind maximum accompanied by the strong downdraft, which enhances the influx of angular momentum at lower levels. The wide extent of the rainband and the increase in cloud hydrometeors in the AR case represent more rainfall, suppressing convection and weakening hurricane intensity. The reduced hurricane intensity also can change the distribution of maritime aerosol concentration so that a large amount of sea salt aerosols is located outside the eyewall region. The modified maritime aerosol concentration at the periphery of the hurricane can reinforce the warm rain process because the large size of maritime aerosol makes it an efficient collector for the small size cloud droplets due to high concentration of continental aerosols. For this reason, the warm rain process in the polluted and AR cases can still play an important role outside the eyewall. Even though the reduced intensity of convection in the polluted and the AR cases is not favorable for the mixed-phase rain process, they exhibit more ice, snow, and graupel mass mixing contents above freezing level at the periphery of the hurricane. The two polluted air cases have much larger amounts of cloud water and water vapor in troposphere, and the increased cloud water can freeze to produce ice water paths. A tropical cyclone in dirty and dusty air has active rainbands outside the eyewall due to aerosol indirect effects. The aerosol direct effect can lead to the suppressing of convection and weakening of updraft intensity by warming the troposphere and cooling the surface temperature. However, these thermal changes in atmosphere are concerned

with the enhanced amounts of cloud hydrometeors and modification of downdraft and corresponding the low level winds in rainband regions. Thus, the AR case can produce the enhanced precipitation even in the weakest hurricane. When comparing the model performance between aerosol indirect and direct effect, the adjustment time of the circulation due to modification of the aerosol radiative forcing by aerosol layers may take a longer time than the hurricane lifetime, and the results from the simulated hurricane show that it is more sensitive to aerosol indirect effects which are related to the cloud microphysics process changes.

From this aerosol study, we can suggest that aerosols can influence the cloudiness, precipitation, and intensity of hurricanes significantly, and there may be different results in the meso-scale convective clouds cases. The hurricane system is a large and complex convective system with enormous heating energy and moistures. Moreover, relationships between various hydrometeors in hurricane systems are difficult to isolate and thus, it needs further study with more realistic cloud microphysical processes, aerosol distributions, and parameterizations.

REFERENCES

Ackerman, A. S., and O. B. Toon, D. E. Stevens, A. J. Heymsfield, V. Ramanathan, and E. J.Welton (2000), Reduction of tropical cloudiness by soot, *Science, 288*, 1042-1047.

Ackerman, T. P., and O. B. Toon (1981), Absorption of visible radiation in atmosphere containing mixtures of absorbing and non-absorbing particles, *Appl. Opt., 20*, 3661-3667.

Andreae, M. O., Rosenfeld, D., Artaxo, P., Costa, A., Frank, G. P., Longo, K. M., and Silva-Dias, M. A. F. (2004), Smoking rain clouds over the Amazon, *Science, 303*, 1337-1342.

Barnes, G. M., E. J. Zipser, D. P. Jorgensen, and F. D. Marks Jr. (1983), Mesoscale and convective structure of a hurricane rainband*, J. Atmos. Sci., 40*, 2125-2137.

Bäumer, D., U. Lohmann, G. Lesins, J. Li, and B. Croft (2007), Parameterizing the optical properties of carbonaceous aerosols in the Canadian Centre for Climate Modeling and Analysis Atmospheric General Circulation Model with impacts on global radiation and energy fluxes, *J. Geophys. Res., 112*, D10207, doi:10.1029/2006JD007319.

Bigg, E. K. (1953), The formation of atmospheric ice crystals by the freezing of droplets, *Q. J. R. Meteorol. Soc., 79*, 510-519.

Bohren, C. F., and D. R. Huffman (1983), Absorption and scattering of light by small particles, John Wiley & Sons, New York.

Camargo, S. J., K. A. Emanuel, and A. H. Sobel (2007), Use of genesis potential index to diagnose ENSO effects upon tropical cyclone genesis, *J. Clim, 20*, 4819-4834, doi:10.1175/JCLI4282.1.

Chazette, P., and C. Liousse (2001), A case study of optical and chemical ground apportionment for urban aerosols in Thessaloniki, *Atmos. Environ., 35*, 2497-2506.

Chou, M.-D., and M. J. Sharez (1999), A shortwave radiation parameterization for atmospheric studies, 15, NASA/TM-104606, P. 40.

Churchill, D. D., and R. A. Houze Jr. (1984), Development and structure of winter monsoon cloud clusters on 10 December 1978. *J. Atmos. Sci., 41*, 933-960.

Cohard, J. M., and J. P. Pinty (2000), A comprehensive two-moment warm microphysical bulk scheme, I: Description and tests, *Q. J. R. Meteor. Soc., 126*, 1815-1842.

DeMaria, M. (1996), The effect of vertical shear on tropical cyclone intensity changes, *J. Atmos. Sci., 53*, 2076-2087.

DeMott, P. J., M. P. Meyers, and W. R. Cotton (1994), Parameterization and impact of ice initiation processes relevant to numerical model simulations of cirrus clouds, *J. Atmos, Sci., 51*, 77-90.

Dunion, J. P., and C. S. Velden, (2004), The impact of the Saharan air layer on Atlantic tropical cyclone activity. *Bull. Am. Meteor. Soc., 85*, 353-365.

Didlake, A. C. Jr. and R. A. Houze Jr. (2009), Convective-scale downdrafts in the principal rainband of hurricane Katrina (2005), *Mon. Wea. Rev., 137*, 3269-3293.

Emanuel, K. A., and D. S. Nolan (2004), Tropical cyclones and the global climate system, paper presented at 26th Conference on Hurricanes and Tropical Meteorology, Am. Meteorol. Soc., Miami, FL.

Fan, J., R. Zhang, G. Li, J. Nielsen-Gammon, and Z. Li (2005), Simulations of fine particulate matter (PM2.5) in Houston, Texas, *J. Geophys. Res., 110*, D16203, doi:10.1029/2005JD005805.

Fan, J., R. Zhang, D. Collins, and G. Li (2006), Contribution of secondary condensable organics to new particle formation: A case study in Houston, Texas, *Geophys. Res. Lett., 33*, L15802, doi:10.1029/2006GL026295.

Fan, J., R. Zhang, W.- K. Tao, and K. I. Mohr (2008), Effects of aerosol optical properties on deep convective clouds and radiative forcing, *J. Geophys. Res., 113*, D08209, doi:10.1029/2007JD009157.

Frank, W. M., and E. A. Ritchie (2001), Effects of vertical wind shear on the intensity

and structure of numerically simulated hurricanes, *Mon. Wea. Rev., 129*, 2249-2269.

Hallet, J., and S. C. Mossop (1974), Production of secondary ice crystals during the riming process, *Nature, 249*, 26-28.

Hänel, G. (1976), The properties of atmospheric particles as functions of the relative humidity at thermodynamic equilibrium with surrounding moist air, *Adv. Geophys., 19*, 73-188.

Hansen, J., M. Sato, and R. Ruedy (1997), Radiative forcing and climate response, *J. Geophys. Res., 102*(D6), 6832-6864.

Hegg, A. D., J. Livingston, P. V. Hobbs, T. Novakov, and P. Russel (1997), Chemical apportionment of aerosol column optical depth off the mid-Atlantic coast of the United States, *J. Geophys. Res., 102*, 25, 293-25, 303.

Hence, D. A., and R. A. Houze Jr., (2008), Kinematic structure of convective-scale elements in the rainbands of hurricanes Katrina and Rita (2005). *J. Geophys. Res., 113*, D15108, doi:10.1029/2007JD009429.

Houze, R. A., Jr., (1973), A climatological study of vertical transports by cumulus-scale convection. *J. Atmos. Sci., 30*, 1112-1123.

Houze, R. A., Jr., (1993), Cloud dynamics, 573 pp., Academic Press, San Diego.

Huang, Y., W. L. Chameides, and R. E. Dickinson (2007), Direct and indirect effects of anthropogenic aerosols on regional precipitation over east Asia, *J. Geophys. Res., 112*, D03212, doi:10.1029/2006JD007114.

Intergovernmental Panel on Climate Change (IPCC) (2007), Climate change 2007: The scientific basis. contribution of working group 1 to the third assessment report, edited by J. T. Houghton et al., 881 pp, Cambridge Univ. Press, New York.

Jiang, J., and G. Feingold (2006), Effect of aerosol on warm convective clouds: Aerosol-cloud-surface flux feedbacks in a new coupled larged eddy model., *J. Geophys. Res., 111*, D01202, doi:10.1029/2005JD006138.

Johnson, B. T., K. P. Shine, and P. M. Forster (2004), A semi-direct aerosol effect:

Impact of absorbing aerosols on marine stratocumulus, *Q. J. R. Meteorol. Soc., 130*, 1407-1422.

Khain, A. P., M. Ovtchinnikov, M. Pinsky, A. Pokrovsky and H. Krugliak (2000), Notes on the state-of-the-art numerical modeling of cloud microphysics, *Atmos, Res., 55*, 159-224.

Khain, A. P., Rosenfeld, D., and Pokrovsky, A. (2005): Aerosol impact on the dynamics and microphysics of convective clouds, *Q. J. Roy. Meteor. Soc., 131*, 2639-2663.

Khain, A. P., N. Cohen, B. Lynn, and A. Pokrovsky (2008), Possible aerosol effects on lightning activity and structure of hurricanes, *J. Atmos. Sci., 65*, 3652-3677.

Knaff, J. A., S. A. Seseske, M. DeMaria, and J. L. Demuth (2004), On the influences of vertical wind shear on symmetric tropical cyclone structure derived from AMSU, *Mon. Wea. Rev., 132*, 2503-2510.

Lau, K. M. and K.-M. Kim (2007), How nature foiled the 2006 hurricane forecasts, *Eos Trans, 88,* 9, pp.105-107.

Li, G., Y. Wang, and R. Zhang (2008), Implementation of a two-moment bulk microphysics scheme to the WRF model to investigate aerosol-cloud interaction, *J. Geophys. Res, 113*, D15211, doi:10.1029/2007JD009361

Liu, Y., and P. H. Daum (2004), Parameterization of the autoconversion process. Part I: Analytical formulation of the Kessler-type parameterizations. *J. Atmos. Sci., 61*, 1539-1548.

Long, A. B. (1974), Solutions to the droplet collection equation for polynomial kernels, *J. Atmos, Sci., 31*, 1040-1052.

Lou, X.-F., Z.-J. Hu and Y.-Q. Shi (2003), Numerical simulation of a heavy rainfall case in south china, *Adv. Atmos, Sci., 20*, 128-138.

Lu, M., and J. H. Seinfeld (2005), Study of the aerosol indirect effect by large eddy simulation of marine stratocumulus, *J. Atmos. Sci., 62*, 3909-3932.

Lynn, B., Khain, A., Dudhia, J., Rosenfeld, D., Pokrovsky, A., and Seifert, A. (2005): Spectral (bin) microphysics coupled with a mesoscale model (MM5), Part 2: Simulation of a CaPe rain event with squall line, *Mon. Wea. Rev., 133*, 59-71.

Mallet, M., J. C. Roger, S. Despiau, J. P. Putaud, and O. Dubovik (2004), A study of the mixing state of black carbon in urban zone, *J. Geophys. Res., 109*, D04202, doi:10.1029/2003JD003940.

Mann, M. E. and K. A. Emanuel (2006), Atlantic hurricane trends linked to climate change, *Eos Trans, 87*, 24, pp. 233-244

Menon, S., J. Hansen, L. Nazarenko, and Y. Luo (2002), Climate effects of black carbon aerosols in China and India, *Science, 297*, 2250-2253.

Meyers, M. P., R. L. Walko, J. Y. Harrington, and W. R. Cotton (1997), New RAMS cloud microphysics. Part II: The two-moment scheme, *Atmos, Res., 45*, 3-39.

Mlawer, E. J., S. J. Taubman, P. D. Brown, M. J. Iacono, and S. A. Clough (1997), Radiative transfer for inhomogeneous atmospheres: RRTM, a validated correlated-k model for the longwave. *J. Geophys. Res., 102*, 16663-16682.

Noh, Y., W. G. Cheon, and S. Rasch (2001), The improvement of the K-profile model for the PBL using LES. Preprints of the International Workshop of Next Generation NWP Model, Seoul, South Korea, P 65-66.

O'Dowd, C. D., J. Lowe, M. H. Smith, and A. D. Kaye (1999), The relative importance of sea-salt and nss-sulphate aerosol to the marine CCN population: An improved multi-component aerosol-droplet parameterization, *Q. J. R. Meteorol. Soc., 125*, 1295-1313.

Powell, M. D. (1990a), Boundary layer structure and dynamics in outer hurricane rainbands. Part I: Mesoscale rainfall and kinematic structure. *Mon. Wea. Rev*., *118*, 891-917.

Powell, M. D. (1990b), Boundary layer structure and dynamics in outer hurricane rainbands. Part II: Downdraft modification and mixed layer recovery. *Mon. Wea. Rev., 118*, 918-938.

Pruppacher, H. R., and J. D. Klett (1997), Microphysics of clouds and precipitation, 2nd ed., 914 pp., Oxford Univ. Press, New York.

Putaud, J. P., R. V. Dingene, M. Mangoni, A. Virkkula, F. Raes, H. Maring, J. M.

Prospero, and E. Swietlicki (2000), Chemical mass closure and assessment of the origin of the submicron aerosol in the marine boundary layer and the free troposphere at Tenerife during ACE-2, *Tellus, Ser. B, 52*, 141-168.

Ramanathan, V., P. J. Crutzen, J. T. Kiehl, and D. Rosenfeld (2001), Aerosol, climate and the hydrological cycle, *Science, 294*, 2119-2124.

Rosenfeld, D. and Woodley, W. L. (2003), Closing the 50-year circle: From cloud seeding to space and back to climate change through precipitation physics. Chapter 6 of "Cloud System, Hurricanes, and the Tropical Rainfall Measuring Mission (TRMM)" edited by: Tao, W.-K. and Adler, R., 234PP., P. 59-80, Meteorological Monographs 51, AMS.

Rosenfeld, D., A. Khain, B. Lynn, and W. L. Woodley (2007), Simulation of hurricane response to suppression of warm rain by sub-micron aerosols, *Atmos, Chem. Phys., 7*, 3411-3424.

Russell, M., D. T. Allen, D. R. Collins, and M. P. Fraser (2004), Daily, seasonal and spatial trends in PM2.5 mass and composition in southeast Texas, *Aerosol Sci. Technol., 38*, 14-26.

Segal, Y., Khain, A., Pinsky, M., and Rosenfeld, D. (2004), Effects of hygroscopic seeding on raindrop formation as seen from simulations using a 2000-bin spectral cloud parcel model*, Atmos, Res., 71*, 3-34.

Seinfeld, J. H. and S. N. Pandis, (2005), Atmospheric chemistry and physics: from air pollution to climate change, 2nd ed., 695 pp., A Wiley-Interscience Publication, New Jersey.

Steiner, M., R. A., Houze Jr., and S. E. Yuter (1995), Climatological characterization of three-dimensional storm structure from operational radar and rain gauge data. *J. Appl. Meteor., 34*, 1978-2007.

Takemura, T., T. Nozawa, S. Emori, T. Y. Nakajima, and T. Nakajima (2005), Simulation of climate response to aerosol direct and indirect effects with aerosol transport-radiation model, *J. Geophys. Res., 110*, D02202, doi:10.1029/2004JD005029.

Van den Heever, S. C., Carrió, G. G., Cotton, W. R., Demott, P. J., and Prenni, A. J. (2006), Impacts of nucleating aerosol on Florida storms. Part I: Mesoscale simulations, *J. Atmos. Sci., 63*, 1752-1775.

Verma, S., O. Boucher, C. Venkataraman, M. S. Reddy, D. Muller, P. Chazette, and B. Crouzille (2006), Aerosol lofting from sea breeze during the Indian Ocean experiment, *J. Geophys, Res., 111*, D07208, doi:10.1029/2005JD005953.

Wang, C., and J. S. Chang (1993), A three-dimensional numerical model of cloud dynamics, microphysics, and chemistry: 2. A case study of the dynamics and microphysics of a severe local storm*, J. Geophys. Res., 98*, 14,845-14,862.

Wang, Y (2002), An explicit simulation of tropical cyclones with a triply nested movable mesh primitive equation model: TCM3. Part II: Model refinements and sensitivity to cloud microphysics parameterization. *Mon. Wea. Rev., 130*, 3022-3036.

Willoughby, H. E., Jorgensen, D. P., Black R. A., and Rosenthal, S. L. (1985), Project STORMFURY, A scientific chronicle, 1962-1983, *Bull. Amer. Meteor. Soc., 66*, 505-514.

Wolf, S. (2002), Mie scattering in particle ensembles under consideration of large size parameter, California Institute of Technology, CA91125.

Woodcock, A. H. (1953), Salt nuclei in marine air as a function of altitude and wind force, *J. Meteor., 10*, 362-371.

Wu, L (2007), Impact of Saharan air layer on hurricane peak intensity, *Geophys. Res. Lett., 34*, L09802, doi:10.1029/2007GL029564.

Yuan Tianle, Z. Li, R. Zhang and J. Fan (2008), Increase of cloud droplet size with aerosol optical depth: An observation and modeling study, *J. Geophys. Res., 113*, D04201, doi:10.1029/2007JD008632, 2008.

Zhang, H., G. M. McFarquhar, S. M. Saleeby, and W. R. Cotton (2007), Impacts of Saharan dust as CCN on the evolution of an idealized tropical cyclone, *Geophys, Res. Lett., 34*, l14812, doi:10.1029/2007GL029876.

Zhang, R., I. Suh, J. Zhao, D, Zhang, E. C. Fortner, X. Tie, L. T. Molina, and M. J.

Molina (2004), Atmospheric new particle formation enhanced by organic acids, *Science, 304*, 1487-1490.

Zhang, R., G. Li, J. Fan, D. L. Wu, E. R. Williams, and M. J. Molina (2007), Intensification of Pacific storm track linked to Asian Pollution, *Proc. Natl. Acad. Sci. USA, 104*, 5295-5299, doi:10.1073/pnas.0700618104.

APPENDIX

CONVECTIVE-STRATIFORM SEPARATION ALGORITHM

The convective-stratiform separation algorithm is using radar reflectivity data and was first suggested by *Churchill and Houze* [1984] using the ideas presented in *Houze* [1973]. The process of separation technique is first to identify convective regions based on the local peakedness of reflectivity values at a certain low level altitude. Then, the remaining pixels are designated as stratiform regions. The convective centers are provided if the reflectivity value of individual pixels exceeds the local background reflectivity (Z_{bg}) by at least the convective center criterion, ΔZ_{CC} [*Steiner et al*., 1995]. In this study, we defined convective centers as grids that have reflectivity values greater than or equal to a certain threshold intensity, Z_{ti}. The local background reflectivity, Z_{bg} is defined as the average of nonzero and nonnegative radar reflectivity values within a radius of 11 km around the grid point. The algorithm must be tuned for the particular radar data because *Steiner et al*. [1995] warned that differences in radar instrumentation affect the algorithm's ability to identify radar signatures. Once convective centers are identified, the grids within a certain radius of the convective center, which is called the convective radius (R), are classified as convective regions. Here R is a function depending Z_{bg} on given by

$$R = \begin{cases} 0.5, & Z_{bg} < 20 \\ 0.5 + 3.5\left(\dfrac{Z_{bg} - 20}{15}\right) & 20 \le Z_{bg} < 35 \\ 4, & Z_{bg} \ge 35 \end{cases},$$

Where *R* is in units of kilometers. The remaining grids with reflectivity less than a certain threshod, Z_{we} are defined as " weak echo". Weak echoes mean ambiguous as to whether they are convective or stratiform. All of the remaining undefined grids are classified as " stratiform". This algorithm is applied at the low level altitude of 2km heights, and the parameters are Z_{ti} = 40 dBZ and Z_{we} = 20 dBZ.

VITA

Name: Keun Hee Lee

Address: Department of Atmospheric Sciences
MS 3150, Texas A&M University,
College Station, Texas 77843-3150

Email Address: anticyclone@naver.com

Education: B.A., Education of Earth Science, Ewha Womans University, 1997
M.S., Atmospheric Sciences, Seoul National University, 2000
Ph.D., Atmospheric Sciences, Texas A&M University, 2011